Particle Tracking and Deposition from CFD Simulations using a Viscoelastic Particle Model

Particle Tracking and Deposition from CFD Simulations using a Viscoelastic Particle Model

Proefschrift

ter verkrijging van de graad van doctor
aan de Technische Universiteit Delft,
op gezag van de Rector Magnificus prof.dr.ir. J.T. Fokkema,
voorzitter van het College voor Promoties,
in het openbaar te verdedigen op vrijdag 6 maart 2009 om 10:00 uur

door

Marco LOSURDO

Laurea in Ingegneria Aerospaziale
University of Rome "La Sapienza"
geboren te Rome, Italie

Dit proefschrift is goedgekeurd door de promotoren
Prof. Dr.-Ing. H. Spliethoff
Prof. Dr. D.J.E.M. Roekaerts

Samenstelling promotiecommissie:

Rector Magnificus, Voorzitter
Prof. Dr.-Ing. H. Spliethoff, Technische Universität München, promotor
Prof. Dr. D.J.E.M. Roekaerts, Technische Universiteit Delft, promotor
Prof. Dr. ir. A.H.M. Verkooijen, Technische Universiteit Delft
Prof. Dr. ir. J.A.M. Kuipers, Technische Universiteit Twente
Prof. Dr.-Ing. C. Bruno, University of Rome "La Sapienza", Italy
Dr. ir. C.C.M. Rindt, Technische Universiteit Eindhoven
Dr. C. Bertrand, ECN, Petten

This research has been founded by ECN (Energieonderzoek Centrum Nederland) and The Netherlands Agency for Energy and the Enviroment (SenterNovem), "Boiler fouling bij biomassa meestoken". Contract No 2020-04-11-14-003.

...to Alberto,

thanks!

Contents

"Vincent: ...you know what they put on french fries in Holland instead of ketchup?

Jules: What?

Vincent: Mayonnaise... "

-Pulp Fiction, 1994.

Abstract

In the present dissertation the mathematical modelling of particle deposition is studied and the solution algorithms for particle tracking, deposition and deposit growth are developed. Particle deposition is modelled according to mechanical impact and contact mechanics taking into account the dependency on time, temperature and particle-deposit composition explicitly. Indeed, such a model lies in the field of the rheology of visco-elastic solids which the author of this dissertation refers to in the following chapters.

Particle adhesion is calculated by imposing an energy balance between kinetic energy, energy loss and the work of adhesion at the impact while the hard sphere approach is applied to model particle to particle collision. These calculations eventually return as result the particle tangential and normal to impact surface (energy) restitution coefficients. Particular attention was given to the implementation of the solution algorithms and the development of a computational strategy to investigate in detail both particle trajectories, properties and deposit locations.

The development of the solution algorithms is twofold, to investigate both particle deposition and the deposit growth applying different computational strategies and algorithms which are usually employed separately *(competitor algorithm solution)*. In the *"integrated"* approach proposed here, these strategies are coupled *(staged partner algorithm solution)* according to a sequential use *(staged procedure)*, to provide detailed and time dependent result data. A novel computer program for Lagrangian particle tracking on unstructured meshes, was developed to investigate particle deposition in Computational Fluid Dynamics (CFD) data post-processing. Developing a particle tracker

program as a separate and CFD independent computer code has overcome several limitations in particle modelling which are present in commercial CFD code (i.e. *non-open source*) even though, on the other hand, it required to develop a robust in-cell particle location algorithm as well as an accurate and efficient particle interpolation and integration time scheme.

All these characteristics and requirements have driven the author in the development of the **P**article **P**ost-**P**rocessor software, nicknamed P^3, which is capable of calculating particle trajectories and deposition, deposit growth and particle-particle interaction (hard spheres model). A specific particle in-cell detection algorithm, to locate the cell hosting the particle, was developed to upload and elaborate results from commercial CFD codes for hybrid-unstructured meshes. Three commercial CFD codes have been tested. Particle tracking on both Reynolds Averaged Navier-Stokes (RANS) and Large Eddy Simulation (LES) results was successfully performed and compared. Numerical results are substantially in good agreement with the experimentals.

Introduction, Motivation and Outline of the thesis

Flows of gases and liquids occurring in diverse industrial and domestic applications are characterized by the presence of particles of different size which are advected in the flow due to the action of aerodynamic forces. In some cases, particle deposition may occur and it may severely decrease the performance of the facility. Most common examples are dust in air conditioning and ventilation pipelines [**1**] or fly ashes in coal and biomass burners [**2**]. Particle deposition phenomena happen under specific circumstances in which particles form and float. For instance, in the oil and food industries temperature and shear-stress gradients in pipelines and food mixing containers are the major cause of particle precipitation, which is also commonly known as fouling (generic formation of deposit) and slagging (vitreous sludge as a result of consistent sedimentation occurring at temperatures close to the glass transition temperature of the deposit). In the so-called "hot" applications, such as coal and biomass burners, high temperatures may cause fly ashes to deposit on the burners walls and on heat exchangers. Indeed, at high temperature, fly ash starts to melt, and interaction with the wall is of the visco-elastic type. The ashes deposited may then undergo specific thermo-chemical transformations in which the deposited ashes first convert themselves into a thermo-solid formation and afterward, due to the reduced heat transfer caused by the deposit itself, into a typically visco-solid molten slag agglomeration. Furthermore, thick agglomerations may eventually modify the flow field inside the burners, altering the performance. More importantly, large agglomerates of slag may eventually detach from the walls and impact and damage delicate components of the burners or simply obstruct ducts and ash collectors. Deposition is extremely dependent

on temperature and composition of the impacting particles: high alkali and solfur concentration in the deposit may induce corrosion, and high silicate content (like biomass) shows a typical glass behavior in a lower operating temperature range. As a consequence, the effort required by the construction and operation of an experimental apparatus aimed at studying particle deposition in real-scale facilities is often deemed prohibitive. For these reasons, numerical investigations are considered a valid support to evaluate the impact of deposition on the performance of the facility to prevent unscheduled outages and severe damage. Generally speaking, particle deposition may occur as a consequence of a negative energy balance between the particle kinetic energy, friction and plastic deformation dissipation and the work of adhesion during either particle-wall or particle-particle inelastic impact [**3, 4**]. Two colliding bodies may adhere to each other, hence agglomerate, and either deposit or grow and proliferate (as bacteria in food industry production) on surfaces. All this depends on thermodynamic conditions: temperature and composition are the driven parameters to estimate deposition behaviors after particle-to-wall impacts or particle-to-particle collisions have occurred. Authors mainly refer to hot and cold impact, respectively for those cases close to the glass transition temperature or substantially below such temperature. Even though the mechanism of deposition-adhesion applies to a wide range of cases, in this work the attention of the author mainly focuses on hot impact cases which are more relevant in power generation facilities burning either coal or biomass. The hot impaction phenomenon has been studied for almost two decades [**2, 5, 6, 7**] using simple mathematical models as well as with the use of Computational Fluid Dynamics (CFD). The latter may represent a more appropriate tool than chemical calculations at equilibrium, generally based on overall empirical indices of ash composition to describe the deposition process [**8, 9**]. Predictions of ash deposition by CFD has been essentially based only on the evaluation of one or more parameter considered significant to describe particle deposition. In literature, particle viscosity, stopping distance, Stokes number and

terminal velocity (the velocity required by a particle to cross the turbulent boundary layer and eventually reach the wall) are usually referred to and considered as the most significant variables to estimate particle turbulent dispersion[**10**] and deposition [**11, 12**]. In the author's opinion, ash deposition can be interpreted as a specific case of the more general particle adhesion problem, which depends upon the evaluation of both impact and adhesion process. Furthermore, it is possible to sort and classify impact and adhesion as hot and cold, depending on whether the impact occurs at temperature at which particle elastic properties dramatically change (closely to the glass transition temperature) or not. The glass transition temperature is a function of the composition, therefore it vaires strongly from case to case. The author's assumption is that both cold and hot impact approaches can be successfully described by visco-elastic theories for solids [**13**]: therefore, not only the instantaneous condition at the impact, but also the history of the colliding bodies is to be taken into account. For temperatures at which elastic properties remain unchanged in time (cold adhesion), isothermal adhesion theories have been formulated by Johnson, Derjaguin, Greenwood and Maugis [**14, 15, 16, 20**].

Such a strong time and temperature dependency has implicitly turned the path and the focus of this Ph.D. study towards the more complex field of *Rheology* where viscous and elastic properties of the solids involved in a collision event are described as dependent on the history before such collision occurred. Therefore, as required in the Rheology modelling, to keep track of the history of each particle, a Lagrangian reference frame was selected to investigate particle deposition behavior.

The final goal if the present thesis is twofold: i) to present a robust and efficient particle localization (particle host cell determination) algorithm, ii) to mathematically describe and implement into a computer code adhesion occurring in hot and cold impacts, as a function of the rheological properties of the colliding bodies [**23, 24**]. In this context, CFD calculations apply to the fluid dynamics of the flow phase, while a stochastic particle modeling approach is used to predict both

particle and deposit history. Furthermore, a novel computational strategy has been developed to apply the rheological approach to previous CFD studies already performed. Eventually, the final result of such investigation is to provide a numerical estimate of particle deposition, deposit composition, deposit thermal resistance and temperature behavior for biomass with high silicate content burners, by applying mechanical and rheological models of visco-elastic solids. Therefore, the computer program dedicated to particle tracking in unsteady flow fields was developed in cooperation with the Energy Research Center of The Netherlands (ECN) to numerical investigate particle deposition and aggregation in industrial facilities characterized by fouling and slagging phenomena [**77**].

This Ph.D. work was initially started to study deposition, ash behaviour, slagging and fouling in pulverized solid fuel and biomass combustion cases. The understanding of such a specific topic have turned out to require a wider knowledge on particle contact mechanics. The author estimated that a suitable model for ash deposition (hot temperature deposition) may eventually require information and modelling for particle both as a physical single entity with unique properties and characteristics, and as groups or clusters which eventually may agglomerate with completely distinct properties and different behaviour from the master particles such agglomerates are made of.

To model ash particles behaviour, from their original state as discrete and single entity till the final solid deposit they might form, a top-down (vertical investigation) approach was first applied. Afterwards, it clearly appeared that applying such a direct strategy was neither sufficient nor consistent with physics to computationally describe ash deposition process: modelling ash deposition requires primarily a deeper knowledge of general particle mechanical impact as well as particle to particle collision. Similarities in particle behaviour have induced the author of this work to proceed both top-down and level-level (horizontal investigation) to meet more detailed modelling requirements and computational flaws detected in the computer programming.

In this Ph.D. study, different commercial CFD codes are used and time dependent particle dynamics is captured thanks to a robust and efficient particle tracking algorithm. In Part I, the numerical strategy and the deposition algorithm are explained, while in Chapter 1 the computational strategy, the hierarchic algorithm of the Particle Post-Processor (P^3) and the particle dispersion are presented. In Chapter 2 the deposit growth and erosion algorithms are explained. In Part II, the visco-elastic theory and approach is explained in Chapter 3 while in Chapter 4 and 5 deposition modelling is presented. In Chapter 6 the adhesion criteria are introduced and in Chapter 7 the model is validated. Results reported in Chapter 7: experimental data on glass particles obtained from the ECN Lab-scale Combustor Simulator (LCS) are compared to the author's numerical results. In Part III, industrial applications are investigated. In Chapter 8 unsteady simulations are performed on a bundle of tubes mimicking particle deposition heat exchangers. In Chapter 9 two cases of sand and soil separation are presented while in Chapter 10 the simulation of particle-particle collision in a scraper crystallizer is investigated. In Part IV, two biomedical applications are presented: in Chapter 11 the numerical strategy and the computer code presented are applied to study aerosol deposition in an idealized extrathoracic mouth-throat model and to a simple simulation on hemodynamics in Chapter 12. An overview of the simulations performed and presented in this dissertation is shown in Fig.0.0.1.

Acknoledgements

The author of this dissertation wishes to acknowledge Prof. Splithoff, Prof. Roekaerts, Prof. Verkoijen and Prof. Kuipers for their valuable and productive scientific support. Rob Korbee, Bart Venneker, Christine Bertrand, Alberto Guardone, Giampietro Carpentieri and Marcos Pascual-Rodriguez for scientific discussions, solutions and ideas suggested to develop this work and The Energy Research Center of The Netherlands for the financial support provided during these years.

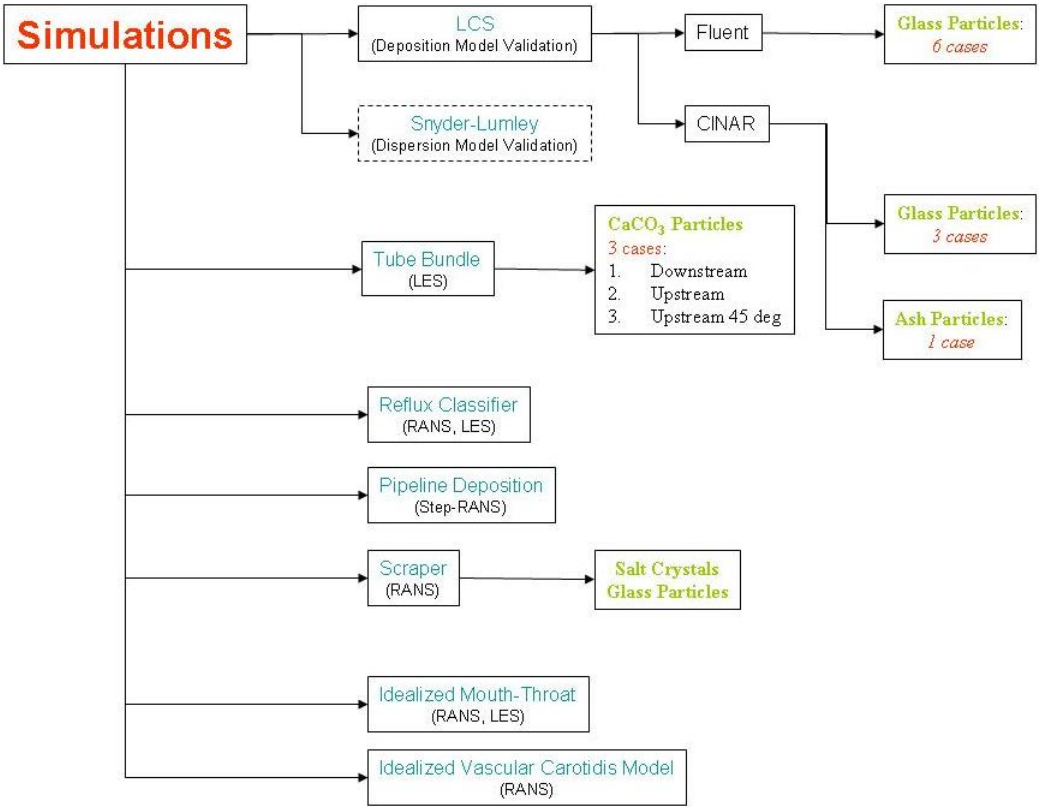

FIGURE 0.0.1. Overview of the simulations

Part 1

Particle Tracking and Solution Algorithm

CHAPTER 1

Computational Strategy

"...He had been one thing before, and now he was another. It was neither better nor worse.
It was different, and that was all."
- 'The New York Trilogy: City of Glass', Paul Auster.

1.1. CFD and Particle Post Processing

The main P^3 algorithm elaborates and integrates CFD data with particle dynamics in order to predict their deposit behavior (see Fig.1.1.1), deposit growth and heat transfer starting from a known flow field that is obtained by a standard CFD code. Particle tracking can be in principle investigated either using the Eulerian or the Lagrangian approach. Due to the Rheological approach attempted, the author focused only on the Lagrangian particle tracking approach in use in commercial CFD codes, that offers, in order of complexity, the following techniques to couple particle and fluid phase motion:

(1) one-way coupling: the fluid phase influences particle motion
(2) two-way coupling: particle motion and fluid phase dynamics influence each other
(3) *"three-way"* coupling: particle-particle interaction is investigated when particle collisions occur. The fluid phase is kept "frozen" as in the one-way coupling.
(4) four-way coupling: particle-particle interaction and flow field are fully coupled.

The time required by a particle to reach equilibrium, either mechanical, thermal or chemical, with the system the particle is contained in is

called *"relaxation time"* that measures the time-dependent response to a change (external force acting on it). In fluid dynamics it is defined as in eq. 1.1.1.

$$\tau_p = \frac{\rho_p d_p^2}{18\mu_f} \tag{1.1.1}$$

where ρ_p and d_p are the particle density and its diameter, respectively, whereas μ_f is the viscosity of the fluid phase. The ratio between the relaxation time and the residence time $\tau_r = \frac{d_c}{U_0}$ gives the dimensionless Stokes number $S_{tk} = \frac{\tau_p \cdot U_0}{d_c}$, where U_0 is the main flow velocity and d_c the main reference dimension. If particle impaction on surfaces is studied, the main obstacle dimension is taken as d_c.

Depending on the Stokes number, one of the above mentioned approaches is selected. A low relaxation time ($S_{tk} \ll 1$) implies that the particle reaches easily and quickly the equilibrium with the surrounding environment, for which a one way particle tracking is preferred. Usually, to save CPU time, the one-way coupling is preferred even in those cases equilibrium may not be reached. Such approach is largely used in ash CFD deposition analysis where particle deposition is investigated using the post-processing approach. The three-way coupling applies only when the Stokes number is much greater than unity ($S_{tk} \gg 1$) and particle collisions are locally likely to occur, see Fig.1.1.2 and Fig.1.1.3. The one-way coupling can be further divided into time averaged (steady) and time dependent (unsteady) calculation. In a time averaged approach, particles are tracked independently from each other. In particular each particle is integrated in time independently, according to its own specific time step. On the contrary, in a time dependent approach, particles can be considered as a group, tracked by a single time step. The computational strategy proposed here deals mainly with the sequential use of time averaged (steady) and time dependent (unsteady) particle tracking, respectively, in the complete and in a selected domain, extracted from the whole computational domain (see Fig.1.1.4).

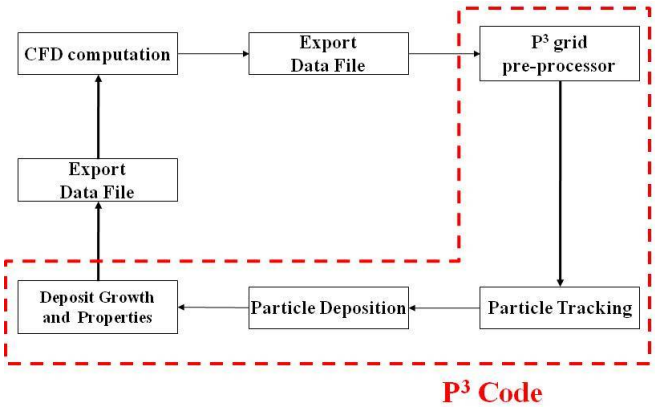

FIGURE 1.1.1. Overview on the P^3 algorithm

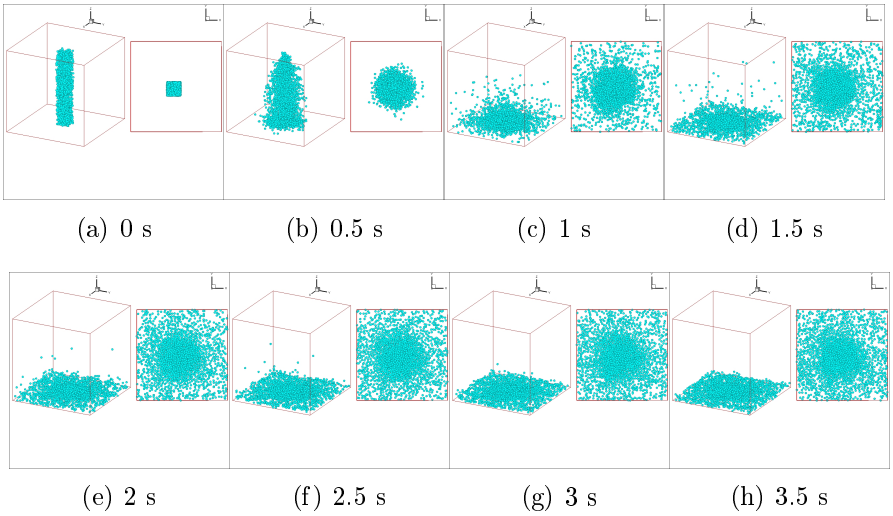

(a) 0 s (b) 0.5 s (c) 1 s (d) 1.5 s

(e) 2 s (f) 2.5 s (g) 3 s (h) 3.5 s

FIGURE 1.1.2. 2000 particle falling in 0.1 × 0.1 × 0.1 m box of still air. Particle density: $2500\,kg/m^3$. Particle diameter: $2.5\,mm$. Particle to particle interaction.

Fig. 1.1.6 and Fig. 1.1.7 show more in detail the algorithms of the steady and unsteady particle tracking separately. In the steady particle tracking, deposit, particle statistics and trajectories are the main output to be perfomed in post-processing (after the computation is finished). On the contrary, the unsteady particle tracking may perform deposit growth or erosion while computing particle tracking.Therefore,

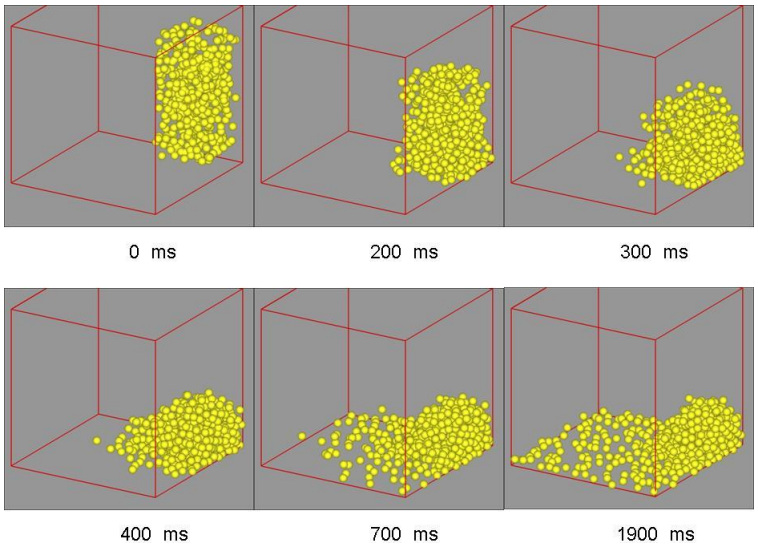

FIGURE 1.1.3. 500 Hard rubber particle 2.0 mm diameter, free fall in 0.1x0.1x 0.1 m box. Friction coefficient set to 0.8

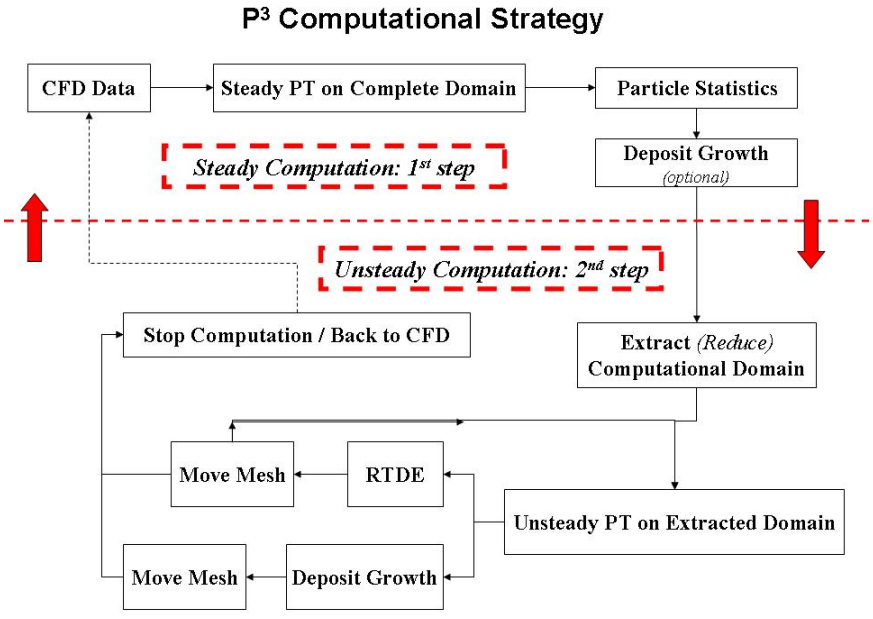

FIGURE 1.1.4. Computational Strategy

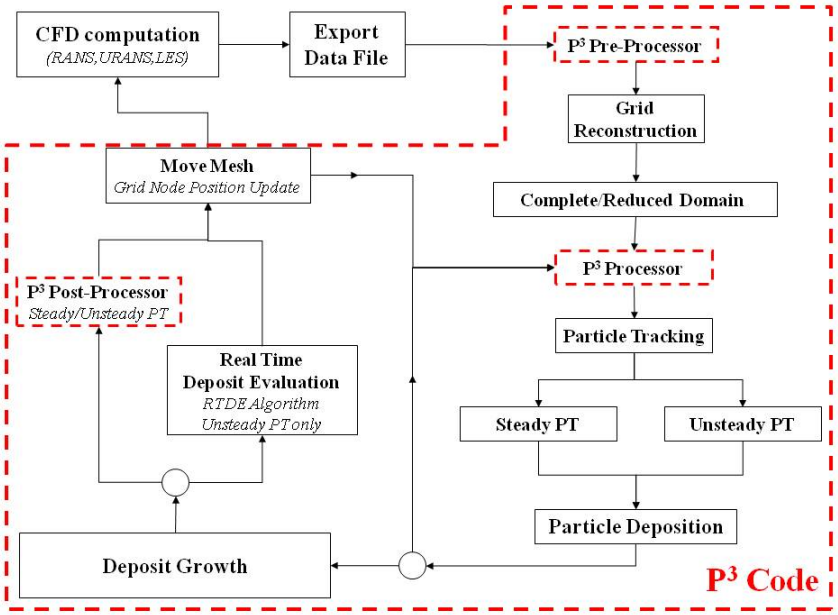

FIGURE 1.1.5. P^3 computational algorithm: detailed

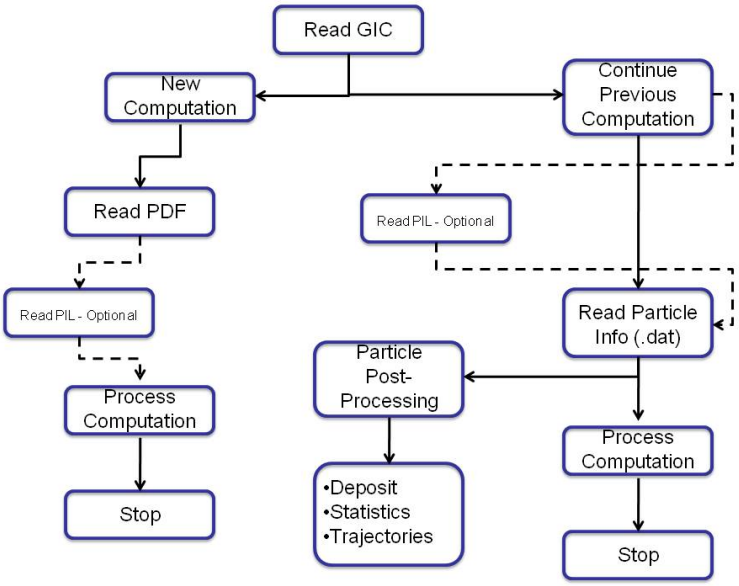

FIGURE 1.1.6. Steady Particle Tracking Algorithm Diagram

deposit and particle statistics are calculated during the computation itself.

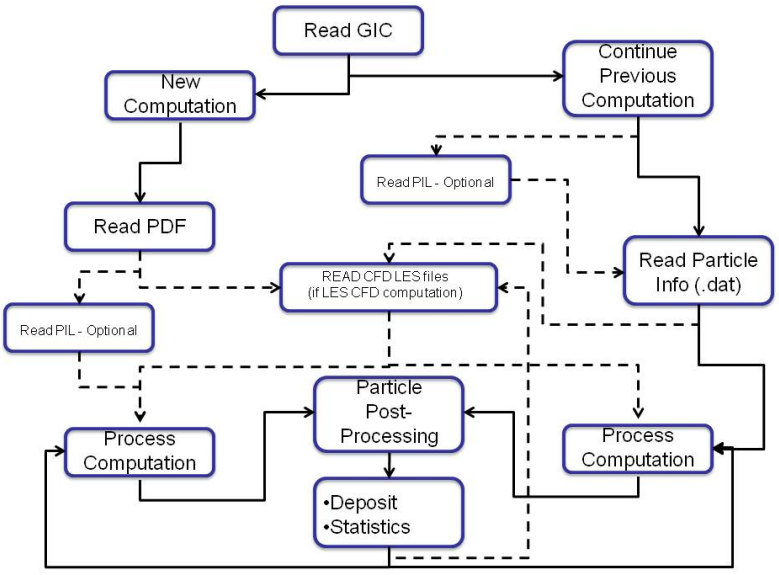

FIGURE 1.1.7. Unsteady Particle Tracking Algorithm Diagram

Time dependent calculations provide useful information concerning particle deposition rate or deposit growth. To study these quantities, a specific algorithm was implemented which allows to estimate the rates of changes of temperature, deposit thickness and thermal resistivity. This algorithm, named RTDE (Real Time Deposit Evaluation, see Fig.1.1.4 and Fig.1.1.5), models particle-particle interaction occurring at the wall during the deposition process, building up the deposit during the computation. Instead of modelling particle-particle interaction on surfaces, which may require a prohibitive number of particles to be tracked (thus leading to high CPU time), particles interact with a deposit surface which takes into account the particles already deposited and mimics their interaction with the new ones impacting ones: where deposition occurs, both boundary and internal grid nodes are correspondingly moved into their new location accounting for the thickness of the deposit. Such strategy reduces indeed the CPU time, since it requires a lower number of particle compared to the full particle-particle interaction model at the deposit location. Furthermore, boundary nodes include new computational variables describing

deposit properties, such as thermal resistance, composition, viscosity and deposit thickness. Moreover, the RTDE algorithm may account for both deposit growth *and* erosion, see Section 2.2. Eventually, the modified mesh could also be uploaded back into the CFD code to solve the Navier-Stokes equations on the modified grid. Enabling the RTDE calculation allows to mimic the particle-particle interaction, as in the three-way coupling, without actually calculating any particle interaction: the effect of the particles already deposited is taken into account by the impact surface nodes properties: thickness, thermal resistance, viscosity and composition of the deposit are calculated when a significant number of particles, given in the input data file, "stop" moving along a surface. In this way, it is possible to study deposition on clean and dirty surfaces while computing particle motion, and also to restart the previous CFD computation on the deposit updated mesh. Depending on the facility that is simulated, the time frame investigated and the particle properties, the deposit thickness may influence the fluid dynamics of the system. It is indeed possible to collect time dependent numerical results and simulate high deposition cases even when the facility may run into the chocking condition, i.e., when the facility is almost completely obstructed.

Experiments have identified several processes including chemical and physical phenomena causing particles deposition. These processes are for example particle inertia, (turbulent) diffusion, thermophoretic forces, vapor condensation and heterogeneous reactions between ash particles and deposition surfaces. Thermophoresis, condensation and inertia impact are the most relevant processes in the deposit growth in combustion cases [**8, 9, 25**]. In the algorithm presented here, condensation is not considered. In most cases of interest, particle inertia represents the main driving physical mechanism leading to deposition. The particle diffusion (dispersion) model has been validated by comparing numerical results with the Snyder and Lumley experimental results [**26**] while the particle deposition model is validated using ECN particle experiments. Thus the present work investigates only the advection,

the diffusion and the deposition of solid non-reactive particles. *'Exporting'* deposition results (by means of updated mesh nodes location) and restarting the CFD computation over the modified geometry is demonstrated using the $Fluent^{TM}$ code. A similar particle post-processing approach was also used by Matida et al. [**27**] to track aerosol particles.

1.2. Outline of the P^3 Algorithms

The P^3 software is a particle tracking post-processor which reconstructs hybrid unstructured CFD meshes, assembling a linear (p1) segmentation of the flow variables over each element, based on the topological node information of the CFD mesh. One of the main issues in developing and performing a Lagrangian particle tracking - location is represented by the computational time required for the particle cell detection., that is, for determining in which cell a given particle currently is. Time integration to compute the particle displacement during the time step and deposit evaluation brings additional computational load. In short, these operations may be gathered into four groups:

(1) Particle location and in-cell detection algorithm (number of operations required to find the cell where the particle is located).
(2) Fluid phase properties at the specific location (particle position): trilinear interpolation for exahedral P1 elements.
(3) Time integration scheme used to predict the new position of the particles, i.e. Euler, Runge-Kutta.
(4) Particle Deposition Evaluation (operations required to assess whether the particle is indeed deposited)

1.3. P^3 Inlet Condition Files

In the P^3 code the *"operative"* inlet information is grouped a text file named General Inlet Condition (GIC), see Fig. 1.3.1, while particle data are in the above metioned Particle Data File (PDF), see Fig. 1.6.2. Two more files are optionally used: the Particle Inlet Location (PIL), see Fig. 1.3.2, and the Extract Computational Domain

file (ECD), see Fig. 1.3.3. Using text files to group operative and inlet conditions enabled users to perform computations without a General User Interface (GUI). The GIC file contains all the operative information and computational options. The PIL and the ECD file apply the bounding box approach: particle locations are defined as point-, line- or volume-locations as well as the domain to be extracted. Furthermore, in the EDC file, inlet and outlet regions are selected according to the same approach, see Section 1.6 for furhter details.

1.4. Particle location and in-cell detection algorithm

The problem referred in literature as Particle Localization or Particle Host Cell Determination, essentially concerns the detection of the (only) cell whose volume contains the investigated particle. Most particle location algorithms available are based on the "Known-Vicinity" approach developed by Lohner [**28, 29**]. Haselbacher et al. [**30**] presented a robust and efficient algorithm which improved the efficiency and solved some errors included in previous work [**31, 32, 33**]. The "Known-Vicinity" approach is based on limiting the cell search to those cells[1] which have a common edge (or face, in 3D) intersected by the particle trajectory. This algorithm exits the loop the edges/face of the candidate cell when the first edge (or face) fulfilling this property is detected. Chen and Pereira (CP approach, [**31**]) first, and lately Haselbacher et al.[**30**] substantially improved the approach proposed by Zhou and Leschziner (ZL approach, [**32**]) even though their detection cell loop searches for intersected edges/faces as well as in the ZL approach, (see Chen and Pereira[**31**] and Haselbacher et al.[**30**] for further details on these approaches). Haselbacher et al.[**30**] solved some of the failures of these algorithms by improving their robustness. The algorithm Haselbacher et al.[**30**] proposed is based on the search for the intersected edge/face. This algorithm not only always

[1] namely, adjacent cells

General Inlet Condition file

Code: FLUENT (Options: FLUENT / CINAR / CFX)
CFD: RANS (Options: RANS,URANS,LES)
CFD_Turb_model: k-e (Options_ k-e, k-omega)
****
UNSCFD_ts: 0.001 s (Unsteady CFD time step)
UNSCFD_IFN: 0 (Unsteady CFD Initial File Number)
UNSCFD_FFN: 60000 (Unsteady CFD Final File Number)
****
REG: Y (Read Existing Grid - Y/N) ECD: N (Extract Computational Domain - Y/N ==> STOP)
RECD: N (Read Extracted Computational Domain - Y/N==>STOP only if ECD:Y)
2CFD: N (Back to CFD: Grid reconstruction - STOP if Y)
PDC: N (Previous Deposit Calculation)
SYM: N (Symmetric Domain ==> SYM files will be read - Y/N)
MYN: N (Meet Your Neighbour ==> To be done before RTDE or DTE!!! ==> STOP)
PIL: Y (Particle injection Location - Y/N)
CPC: N (CPC:Continue Previous Calculation: Y/N) SCI: 10 (Saving Computation Interval: 10,100,1000 etc...only for Steady PT and for RTDE.EQ.'Y')
SCN: 0 (SCN:Specific Computation Number==>URANS,LES+PT=U only if .NE. 0)
****
Operative_P: 101325 (Pressure is in [Pa])
GDX: 0.d0 (Gravity Direction X)
GDY: 0.d0 (Gravity Direction Y)
GDZ: 1.d0 (Gravity Direction Z)
****
PT: S (Particle Tracking: S/U = Steady/Unsteady)
RTDE: N (Real Time Deposit Evaluation - Unsteady PT only)
DEC: 1.d0 (Deposit Evaluation Coefficient)
EPT: N (Extract Particle Trajectories: Y/N ==> STOP) ONLY FOR STEADY CALCULATION
DTE: N (Deposit Thickness Evaluation: Y/N ==> STOP only if RTDE.EQ.'N')
PSP: 0.d0 (Particle Scatter Percentage| Range: 0.d0 - 1.d0)
PPI: N (Particle-Particle Interaction: Y/N; Y only if PT=U)
VEM: E3 (Visco-Elastic Model: E1,E2,E3,E4,E5,E6)
Thermophoresis: N (Y/N)
****
EPN: 0 (Estimated Particle Number:if EPN=0/-1 => (PT=S, U)
DPI: 1.d-3 s
RIR: 1.0061822d-6 Kg/s
total_time: 3600.d0 s
dt_writing: 1.d3 s
time_step: 1.d-3 s
min_time_step: 1.d-4 s
ISN: 1 (Intermediate Step Number: must be at least 1, integer variable)
TIS: RK (RK/EU => Runge-Kutta or Euler Time Integration Scheme)
RKPC: N (Runge-Kutta Predictor-Corrector - Y/N)
RKI: 2 (Runge-Kutta Intervals ==> Hmax = time step/RKI)

FIGURE 1.3.1. P^3 inlet condition file

Particle Injection Location - PIL

ILN: 1 (Injection Location Number - integer number)
****
x_{min}: -0.006 (m)
x_{max}: 0.006 (m)
y_{min}: -0.00 (m)
y_{max}: 0.006 (m)
z_{min}: 0.001 (m)
z_{max}: 0.005 (m)

FIGURE 1.3.2. P^3 Particle Inlet Location file (PIL)

Extracted Computational Domain Coordinates

```
ECD_xmin= -100.d0
ECD_xmax= 100.d0
ECD_ymin= -100.d0
ECD_ymax= 100.d0
ECD_zmin= 4.d0
ECD_zmax= 9.d0
********************
Inlet Box Coordinates

IBC_xmin= -100.d0
IBC_xmax= 100.d0
IBC_ymin= -100.d0
IBC_ymax= 100.d0
IBC_zmin= 4.1d0
IBC_zmax= 4.2d0
********************
Outlet Box Coordinates

OBC_xmin= -100.d0
OBC_xmax= 100.d0
OBC_ymin= -100.d0
OBC_ymax= 100.d0
OBC_zmin= 8.9d0
OBC_zmax= 9.d0
```

FIGURE 1.3.3. P^3 Extract Computational Domain file (ECD)

requires the information on the particle starting position, but also detects every cell the trajectory intersects till the given particle current position is reached. In fact, such information is necessary only for the two-way and four-way coupling, while it is neither necessary nor required and is CPU time consuming in case of particle post-processing (one-way or three-way coupling). Haselbacher's algorithm presents four advantages compared to the previous particle location algorithms: a) it applies to arbitrary polyhedral cells, b) it is not limited to small particles displacements, c) it naturally deals with boundaries and d) it is robust and efficient. Recently, Martin et al. [**34**] presented an improved host cell detection algorithm based on the work of Lohner and Haselbacher for 2-D and 3-D polyhedral unstructured mesh. Martin's algorithm uses the adjoining-face-searching, which essentially consists in performing the host cell search looking for the crossed face of each candidate neighbor cell. The solution proposed by Martin et al. [**34**] to optimize the loop requires both the particle previous position $\bar{P}^{n-1}$ and location (previous host cell j^{n-1}). To progress from one cell to another until the current host cell j^n is detected, the algorithm calculates the scalar (dot) product of the displacement vector of the particle

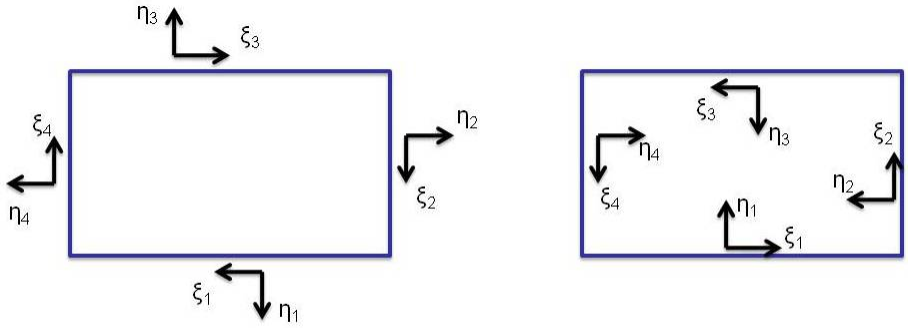

FIGURE 1.4.1. Local Reference Systems: (a) Outward and (b) Inward orientation

$\bar{P}^n - \bar{P}^{n-1}$ and $\bar{P}^n - \bar{C}_{i,j}$, the vector from the centroid $\bar{C}_{i,j}$ of the face i of the candidate cell j to the current particle position $\bar{P}^n$. If $\left(\bar{P}^n - \bar{P}^{n-1}\right) \cdot \left(\bar{P}^n - \bar{C}_{i,j}\right) > 0 \; \forall i$, then the cell has been crossed by the particle and the search moves towards the next cell j' whose boundary face meets both $\left(\bar{P}^n - \bar{P}^{n-1}\right) \cdot \left(\bar{P}^n - \bar{C}_{i,j'}\right) > 0$ and $\left(\vec{d}_{i,j'} \cdot \vec{n}_{i,j'} \geq 0\right)$, where $\vec{d}_{i,j}$is the vector from the face i of the new cell j' to the particle position. The local reference system adopted by Martin [**34**] is the outward pointine while the reference system used in the P^3code is the inward pointine, as sketched in Fig. 1.4.1 and 1.4.2.

The P^3 code does not store the information concerning face directions. This fact largely affect time and CPU performance since at every cell face the local reference system must be calculated. The local-to-face inward reference system is calculate centering the reference system at the first node of each face. According to the anticlockwise orientation, for the edge/face i, $\overrightarrow{V_iV_{i+1}} = \overrightarrow{\xi_i}$, $\overrightarrow{V_iV_{i-1}} = \overrightarrow{\eta_i}$.

For the 2-D square element sketched in Fig. 1.4.2a, the (anticlockwise) sequence is the following:

(1) edge 1. $\overrightarrow{V_1V_2} = \overrightarrow{\xi_1}$, $\overrightarrow{V_1V_4} = \overrightarrow{\eta_1}$
(2) edge 2. $\overrightarrow{V_2V_3} = \overrightarrow{\xi_2}$, $\overrightarrow{V_2V_1} = \overrightarrow{\eta_2}$
(3) edge 3. $\overrightarrow{V_3V_4} = \overrightarrow{\xi_3}$, $\overrightarrow{V_3V_2} = \overrightarrow{\eta_3}$
(4) edge 4. $\overrightarrow{V_4V_1} = \overrightarrow{\xi_4}$, $\overrightarrow{V_4V_3} = \overrightarrow{\eta_4}$

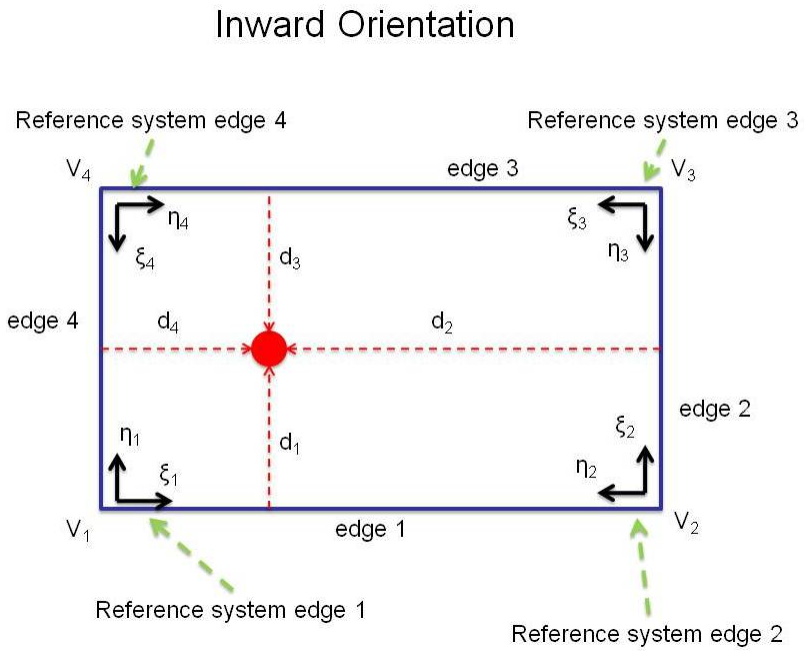

(a) 2D square element

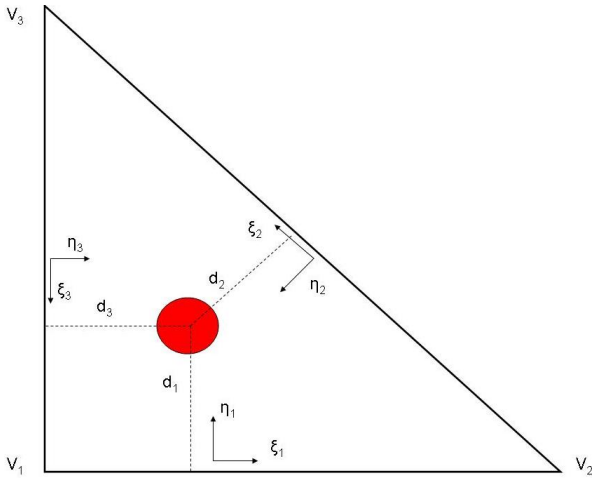

(b) 2D triangle element

FIGURE 1.4.2. Local Reference System within the candidate host cell

To detect the next cell crossed by a particle, two main techniques are largely in use:

(1) The cell selection is based simply on looping through the faces and choosing the first face that generates a positive dot (scalar) product. This technique is referred to as the First Positive Dot Product (FPDP) method [**34**]. This method has the advantage of not having to search every face of an element (which can be many in 3-D cells) before moving on to the next host cell. It may be suboptimal in that the chosen cell is dependent upon face inspection order.

(2) The cell selection is based on looping through the faces and choosing the one that generates the largest positive dot product. This technique is referred to as the Maximum Positive Dot Product (MPDP) method [**34**].

As reported in [**30**], the first technique 1 may fail to detect the host cell. In this case, the algorithm searches for the current host cell using a coarser mesh, or in the worse case, on the entire domain ("brute force" solution as in [**28, 29**]). Furthermore, if hybrid polyhedral meshes are used with large scale factor for the cell step-size, the FDPD technique 1 may result computationally expensive.

Fig. 1.4.3 describes the MPDP technique adopted by Martin [**34**].

The particle location algorithm proposed here has been developed independently by Haselbacher [**30**] and Martin [**34**]. It includes all the features which characterize Haselbacher's and Martin's algorithm and, in addition, it requires neither the initial particle position nor it detects every intersected cell, unless the particle falls out of the domain skipping the boundary cell layer. Furthermore, it deals naturally and correctly with boundaries and large scale factor cell step-size and time integration step. Furthermore, the trilinear isoparametric interpolation is applied. A shape function is associated to each node of the cell and particle properties can be calculated at the particle position. For an hexahedron, the nodes have coordinated in the range $[-1, +1]$, see Fig. 1.4.4. If particle coordinates have values out of this range, such a particle is certainly out of the cell. Such a technique was introduced by

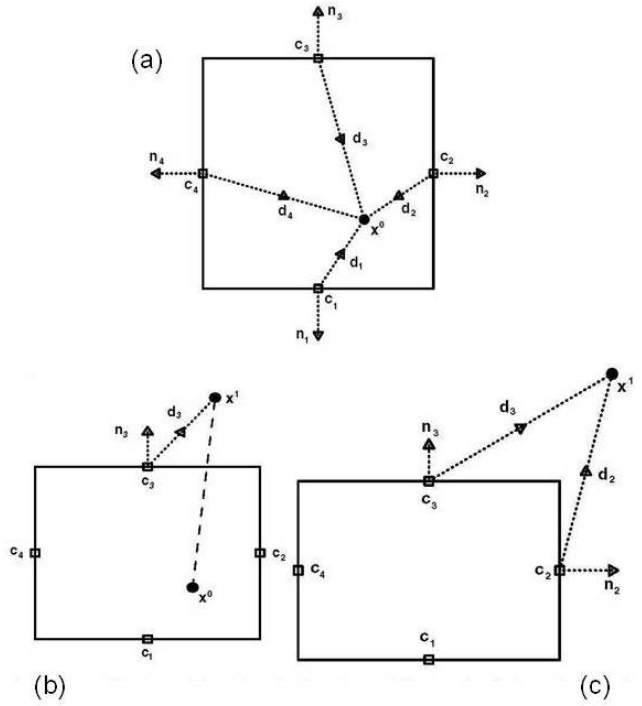

FIGURE 1.4.3. MPDP strategy. Picture taken from Martin et al. [**34**]

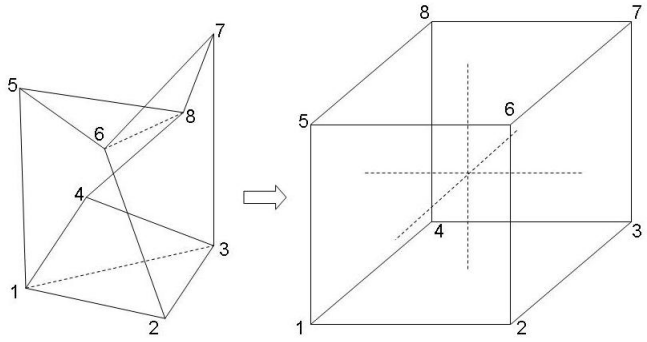

FIGURE 1.4.4. Trilinear Isoparametric Interpolation. Hexahedron example

Lohener and Ambrosiano [**28**] to easily and quickly calculate distances from distorted faces in non-structured meshes.

The MPDP techinque 2 is used in the P^3 code to detect the crossed face if the search results in multiple candidate cells or at the boundaries

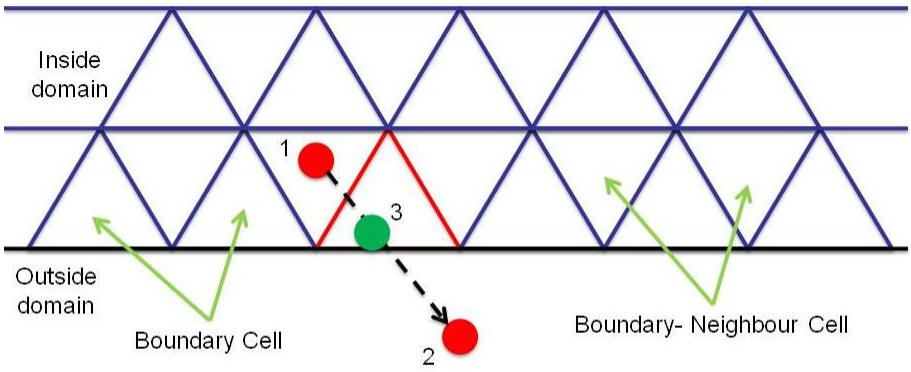

FIGURE 1.4.5. Boundary and Boundary-Neighbour cells. Crossed cell face and correct boundary cell detection

for both corner cells (more than one wall face) and boundary-neighbour cells[2], as sketched in Fig. 1.4.5.

The detection of the cell where the particle is located consists of a two-step particle bounding box algorithm. CPU requirements are quasi-independent on the mesh size (computational nodes) and completely independent on the starting particle position at each time step. The two step (particle) cell detection algorithm has been developed to comply with computational efficiency and accuracy in the particle trajectory calculation. During the grid reconstruction process (P^3 preprocessor, see Fig.1.1.5) the maximum and minimum coordinates of each cell are written into a file to determine the virtual bounding box of the cell (see Fig. 1.4.6). Hence, the first step of the algorithm is the search for those cells whose virtual bounding box contains the particle.

If the output of this screening is only one cell, the search is completed and the cell is detected. If the result is more than one cell, as it is often the case, the particle lies in a region where multiple bounding boxes overlap. In this case, the second step of the algorithm must be

[2]Boundary-Neighbour cells: cells having only one vertex or one edge on the boundary and not a face. A boundary cell is a cell which has least one wall face whereas a corner cell is a cell which has more than one wall face.

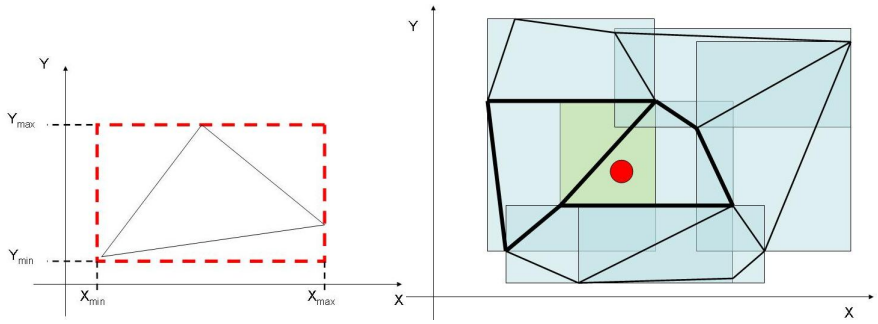

FIGURE 1.4.6. Cell Bounding Box Approach in 2D. a) triangle, b) quadrilateron

performed. In the second step, the cell contains the particle only if $\left(\vec{d}_{i,j} \cdot \vec{n}_{i,j} \geq 0\right)\ \forall i$, namely, if the distances between the particle and each face of the cell is positive (see Fig.1.4.2). The scalar (dot) product $\left(\vec{d}_{i,j} \cdot \vec{n}_{i,j} \geq 0\right)$ is used to calculate both the tangent $\left(\vec{d}_{i,j} \cdot \vec{n}_{i,j} \approx 0\right)$ and the crossed faces, largest positive $\left(\vec{d}_{i,j} \cdot \vec{n}_{i,j} > 0\right)_{max}$ of the cell.

Instead of performing such a calculation over each cell of the computational domain, which is referred in literature as "brute force approach" [**29**], the loop is performed only for those cells listed as candidate cells whose bounding boxes overlap. The trilinear isoparametrical algorithm [**35**] is used to calculate both the distances from the cell faces and to interpolate nodes variables at the particle location [**33**]. The reason for using an interpolation with linear shape function is that it allows to take into account cell distortion, caused by both by the mesh generator (unstructured commercial CFD codes) and by the deposit evaluation, since grid nodes are moved. The implemented trilinear interpolation requires less than four iterations to converge since the first iteration is performed using a rough estimation of the particle position normalized by the cell dimension. The main feature of this algorithm (see Algorithm 1), is its capability of unambiguously detecting the cell where the particle is located regardless of any cell distortion. The CPU requirements for this second step in the particle detection algorithm can be considered to be almost independent from the total amount of cells

Algorithm 1 Main steps of the P^3 global algorithm

(1) Starting position is assigned to every particle
(2) Loop on each particle: result=0
  (a) Find cell: Loop on those cells whose bounding box contains the particle position
    (i) IF result=1, cell detected. THEN exit the loop
    (ii) ELSE, loop on the faces of the selected cells to check on the (positive) distances from the cell's faces (trilinear isoparametric interpolation)
      (A) Loop on the candidate cells
      (B) IF every distance ≥ 0, THEN result = result+1 (two or more cells having positive volumes cannot simultaneously have all distances positive)
      (C) END Loop
    (iii) ENDIF
  (b) END Loop
  (c) IF result=1, (cell detected) THEN exit
  (d) IF result > 1 AND at least one distance $= 0$, THEN
    (i) IF the previous cell is included in the group of selected, THEN it is picked up
    (ii) ELSE, the first cell in the selected cell array is chosen
  (e) END Loop (on the cells)
  (f) IF result is 0, THEN particle is out of the domain
    (i) Check on particle's previous position:
      (A) IF the particle has crossed the outlet, THEN particle is out.
      (B) IF the particle has crossed a wall boundary, THEN calculate restitution coefficients
      (C) IF the particle collision fulfills the adhesion requirements, THEN particle deposited
      (D) ELSE the particle rebound
    (ii) Particle time integration (Runge-Kutta 4^{th} order)
    (iii) Save particle Position and Properties in the output file
  (g) ENDIF
(3) END Loop (over particles)

and their typology (shape of the cell) as the distance calculation loop is set only on the narrowest volume surrounding the particle and including at least one cell. Usually, the computation is typically limited to a maximum of seven cells if a tetrahedral mesh is used while, for regular hexahedral meshes, the correct cell is usually detected during the first step.

1.4.1. The Three Zeno's Motion Paradoxes.

When it comes to mathematically describe the motion of any solid body by a computer program, an interesting computational problem may arise that is well described by recalling three paradoxes on the body motion which were issued by the Greek philosopher Zeno.

Let us start from Zeno's second paradox *(the dichotomy paradox)*.

> *"That which is in motion must arrive at the half-way stage before it arrives at the goal"*
>
> Aristotle, Physics VI:9, 239b10

Integrating Newton's second law in time, a time step consistent with the physics must be selected. In case of a particle moving from one side to another of a hosting cell (discrete volume delimited by edges and faces) if the integrating time step is simply chosen as $dt = \frac{distance}{velocity}$ or smaller due to machine precision, round-off and truncation errors, the center of gravity of the moving body may never cross the boundary it was heading to, unless a minimum dt is selected as a the lower threshold level. Such assumption implies that any moving body will never exactly reach any edge of its containing domain (it is moving within) but it can only be either inside or outside. A straightforward consequence is depicted in Fig. 1.4.7: in order to get into a tangent position (position P_3), a particle has to either cross the boundary (P_2 outside location) or be at a distance lower than its radius. In both cases, when out of the domain or at a distance lower than the radius (impact occurred), it is considered what happens to the particle in the tangent to wall position and adhesion hence evaluated. One of the key features of the proposed particle tracking algorithm is the fact that if the result of the search of the host cell for a particle returns zero, it simply means that the particle is out of the domain; therefore, the typology of the surface crossed (either outlet or wall) may be assessed.

In the case of two colliding bodies (particle-particle collision), the third Zeno's paradox *(Achilles and the tortoise)* has to be addressed:

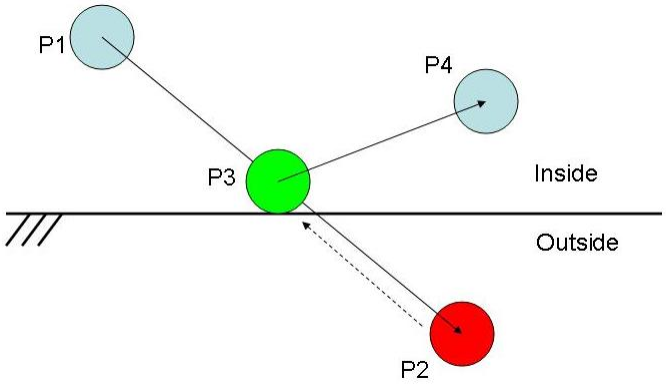

FIGURE 1.4.7. Particle Step Back

> *"In a race, the quickest runner can never overtake the slowest, since the pursuer must first reach the point whence the pursued started, so that the slower must always hold a lead."*
>
> Aristotle, Physics VI:9, 239b15

This paradox points out the non-trivial computational problem of simultaneous motion of (pointwise) solids. In this work the hard sphere approach (presented in the mathematical modelling part) does not allow for multiple simultaneous, albeit instantaneous, collisions to occur. The error provided by such assumption can only be reduced by decreasing the integrating time step, but can not be prevented.

Concerning the rendering of the particle's motion into a *visible* format, either a sequence of discrete snapshots or an animation (collection of several sequential snapshots), the Zeno's first paradox states:

> *"If everything when it occupies an equal space is at rest, and if that which is in motion is always occupying such a space at any moment, a flying arrow is therefore motionless"*
>
> Aristotle, Physics VI:9, 239b5

Such a statement essentially denies the possibility of representing any moving body: a collection of steady snapshots (frames saved by the computer code at each time step, recording particles' position along

the domain) would *simply* result in keeping track of a steady motion which is after all a "no motion" condition since an instant is only a snapshot. Therefore, if it cannot move in a single instant it cannot move in any instant, making any motion impossible to be represented. In other words, an external observer cannot see solids moving since they are "framed" in snapshots within which they cannot move. Solids may move only *in between* these snapshots, when an external observer cannot see them actually moving.

Therefore, according to this statement, none of the animations performed and presented in this work may exist...

The ultimate conclusion following these paradoxes is that numerical simulations are affected by inevitable errors. In particular, describing particle motion under force action in a computer program may have intrinsic, although basic, conceptual problems since the final goal is to discretize, at least in time using time steps to integrate formulas, a process which occurs in continuum without assumptions or numerical tollerance. Since this work mainly concerns (spherical) solid motion, recalling the fact that computer coding is affected by the same motion paradoxes, issued thousand years ago, indeed provided a *"wise"* support to implement the solution algorithm.

1.4.2. Fluid Phase Interpolation.

To calculate the external forces acting on a particle, the fluid variables at the particle location have to be calculated. The trilinear interpolation approach developed for the cell detection is used also in this case. Depending on the total number of particles, mesh topology and total number of cells, the computing cost, in terms of time, might become too expensive. In order to reduce the CPU time, at the cost of the discretization error, instead of interpolating the fluid phase variable at the particle location, the center cell values can be used for internal cells (non-boundary cells). For boundary cells both the trilinear isoparametric interpolation and the physical model for the wall turbulence anisotropy developed by Dreeben and Pope [**36**] are adopted and

implemented according to the method proposed by Dehbi[**37**]. Similarly, Greenfield and Quarini [**38**] used fluctuation velocity correction taken from Kallio and Reeks [**39**], while Matida et al.[**27**] implemented in their particle tracking code the turbulence anisotropy corrections developed by Wang and James[**40**] for a channel flow. Although these formulations were derived from Direct Numerical Simulation (DNS) data fitting of specific channel flows, they are expected to substantially improve the accuracy of thecalculation at the boundary for most of the cases of interest in this work.

1.4.3. Time integration schemes.

Two time integration schemes are currently available in the P^3 post-processor: the Runge-Kutta 4^{th} order Felberg method and the explicit Euler method. The strategies mentioned above to reduce the CPU time allowed to track and evaluate deposition of 10^4 particles in a 35×10^4 unstructured polyhedral mesh in about 72 hours, using a single Pentium IV 3.0 GHz processor. However, the presented implemented algorithm in FORTRAN 95 is not CPU time optimized, since this aim is beyond the author's intent. In this work, the Runge-Kutta scheme is applied, unless specified otherwise.

1.5. Particle Dispersion Modeling

The forces implemented to describe particles motions are drag, gravity and thermophoresis [**43**], this last disabled both in isothermal and high particle Stokes number conditions[3]. The velocity and the position of each particle are calculated using the Runge-Kutta 4^{th} order

[3]Since thermophoresis contribution is neglegible in those cases

scheme to time integrate Newton's second law.

$$\begin{cases} \frac{dU_x}{dt} = \frac{\rho_f}{\rho_p}\frac{3}{4}\frac{C_D}{d_p}\cdot|u_x - U_x|\,(u_x - U_x) + \left(\frac{\rho_f}{\rho_p} - 1\right) g_x + F_{th_x} \\ \\ \frac{dx}{dt} = U_x \\ \\ \tau_p = C_n \frac{\rho_p}{\rho_f}\frac{4d_p}{3C_D\left|u_f - u_p\right|} \end{cases} \tag{1.5.1}$$

where U_x, ρ_p and u_x, ρ_f represent the velocity and the density of the particle and the flow velocity and density (at particle i location) respectively. d_p is the particle diameter while g_x and F_{th_x} are the gravity and the Thermophoretic force in the x Cartesian direction. Similar equations apply for the y and z directions. Solving eq.1.5.1, the instantaneous particle velocity and position are given at each time step and τ_p is the particle relaxation time. The drag coefficient C_D is calculated according to Morsi and Alexander [**44**]. C_n is the Cunningam slip correction factor for submicron particles. In RANS simulations, the particle dispersion has been modeled using the so called particle random walk - Lagrangian stochastic Eddy Interaction Model (EIM), developed by Gosman and Ioannides [**45**]. In the present work, the EIM is $\kappa - \varepsilon$ based as in Schuen et al. [**46**] and currently present in $FLUENT^{TM}$ [**47**]. The EIM model calculates the particle-turbulence interaction by means of the "eddy lifetime" model: a particle moves from one eddy to another according to the particle eddy crossing time and the eddy lifetime τ_e (or the Lagrangian eddy integral time T_L). This model bases the calculation of the Lagrangian eddy life time on κ and ε, respectively the turbulent kinetic energy and its dissipation rate: when the particle has resided in the eddy for a time longer than its life time or the eddy crossing time, the fluid velocity fluctuation u' is updated and the instantaneous velocity u is calculated. Further details on this model are reported in [**41**]. Integral time scale and eddy life-time are calculated as

$$T_L = C_L \cdot \frac{\kappa}{\varepsilon} \tag{1.5.2}$$

$$\tau_e = -T_L \cdot \ln n_r$$

where C_L is a turbulent coefficient usually in the range of $0.15-0.3$, and n_r is a random number in the range $0-1$.

In the case of isotropic turbulence, the fluid velocity in any direction is modeled in RANS and URANS simulations as

$$u = \bar{u} + u' \tag{1.5.3}$$

$$u' = \zeta_x \sqrt{\bar{u'^2}} = \zeta_x \sqrt{\frac{2}{3}\kappa} \tag{1.5.4}$$

where ζ_x is a Gaussian random number, u, $\bar{u}$ and u' are the actual velocity, the mean velocity and the fluctuation (e.g., in the streamwise x direction).

To model the anisotropy occurring at boundaries for $y^+ < 80$, several correction formulas have been introduced [**10, 36, 37, 39**]. In this work, the formulation used by Dehbi derived from Dreeben and Pope is used. That is, the non-dimensional fluctuations are defined as

$$f_u = \frac{\sqrt{\bar{u'^2}}}{u^*} = \frac{0.4 \cdot y^+}{\left(1+0.0239 \cdot (y^+)^{1.496}\right)}$$

$$f_v = \frac{\sqrt{\bar{v'^2}}}{u^*} = \frac{0.0116 \cdot \left(y^+\right)^2}{\left(1+0.2039 \cdot y^+ + 0.0014 (y^+)^{2.421}\right)} \tag{1.5.5}$$

$$f_w = \frac{\sqrt{\bar{w'^2}}}{u^*} = \frac{0.19 \cdot y^+}{\left(1+0.0361 \cdot (y^+)^{1.322}\right)}$$

where f_u, f_v and f_w are the fluctuations in the stremwise, spanwise and normal to boundary direction and u^* is the friction velocity, defined as $u^* = \sqrt{\frac{\tau_w}{\rho_{gas}}}$ and $\tau_w = \mu_{gas} \cdot \frac{\partial u}{\partial y}$ and y^+ the dimensionless distance to the wall, calculated as $y^+ = \frac{u^* y}{\nu}$ where y is the local distance from the nearest wall and ν is the kinematic viscosity of the fluid.

Since the dimension of the particles tracked is smaller than the main cell dimension[4], $y^+ > 80$ condition is usually met outside the boundary cells for . Therefore, the f_u, f_v and f_w are calculated in the P^3 code only if the particles reside in a wall boundary cell. This approximation may affect the particle trajectories in RANS calculations for very small particles. However, the instantaneous flow velocity $\overline{u}$ is the filtered velocity in LES simulations. To include the instantaneous velocity fluctuations either a stochastic Langevin-type model to account for the discarded turbulence at the Sub-Grid Scale (SGS) level [**48**], or a very fine mesh in conjunction with a small integration time step may be used. Adopting the latter approach implies that the LES might turn into a Direct Numerical Simulation (DNS), becoming as accurate as computationally expensive.

The particle dispersion model has been validated against Snyder and Lumley experimental data [**26**] at $Re = 10^5$. This experiment concerns particle dispersion along a 0.6 m shaft. An air-blower with a grid provides a homogenous turbulence to the flow. The experimental data provided for the validation concern the dispersion from the centerline of the shaft, see Fig.1.5.1, while for the particle velocity fluctuation a turbulence ratio was plotted, see Fig.1.5.2.

Milojevic[**61**] used Snyder and Lumley data to validate a particle dispersion model based on Gosman and Ioannides [**45**]. Results presented in this dissertation are in good agreement with those presented by Milojevic and with the experimental ones only for the particle dispersion. In particular, Milojevic reported that, due to some uncertainty in fluctuation measurements and the stochastic based model used, it is not possible to match the experimental data unless a specific tuning parameter is applied to each case. The author of this dissertation shares this opinion, considering the results obtained on the dispersion sufficiently accurate to accept as valided the fluctuation model implemented into the computer program.

[4]Reference cell dimension: $\sqrt[3]{Volume_{cell}}$

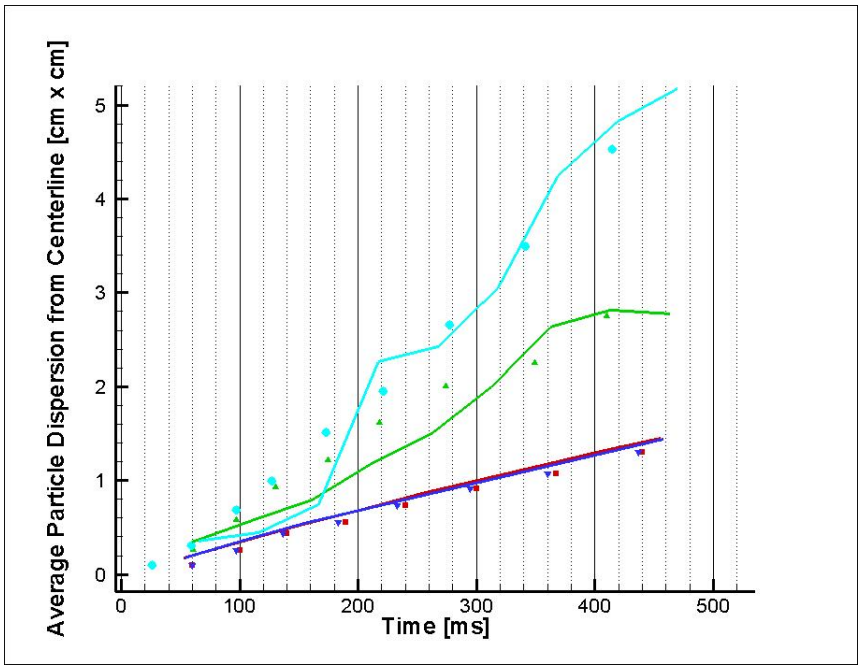

FIGURE 1.5.1. Snyder and Lumley particle dispersion from the centerline. •corn pollen, ▲hollow glass, ▼solid glass, ■ copper

1.6. Combined use of Steady and Unsteady particle tracking

Combining steady (time averaged) and unsteady (time dependent) particle tracking over a smaller computational domain allows to reduce the computational cost of the total simulation and to improve the accuracy only in the volume selected (the so-called reduced computational domain), as shown in Fig.1.6.1.

The idea behind this approach is to decrease the total number of particles (hence CPU time) that would be required for a reliable statistic analysis if either steady or unsteady particle tracking were independently used. The first step is to perform a steady particle tracking calculation with a minimum number of particles (still statistically consistent with the physics and the CFD grid) over the entire domain. Deposit and trajectories statistics of this first step as well as the list of the cells, which have been crossed during the steady particle motion, are calculated. This information is used as input of the unsteady

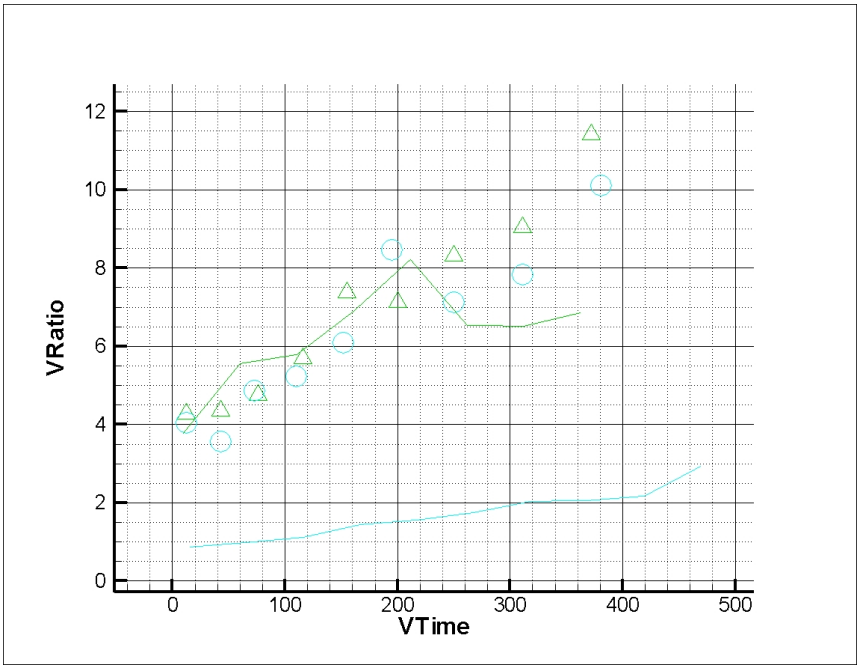

(a) Corn Pollen - Hollow Glass

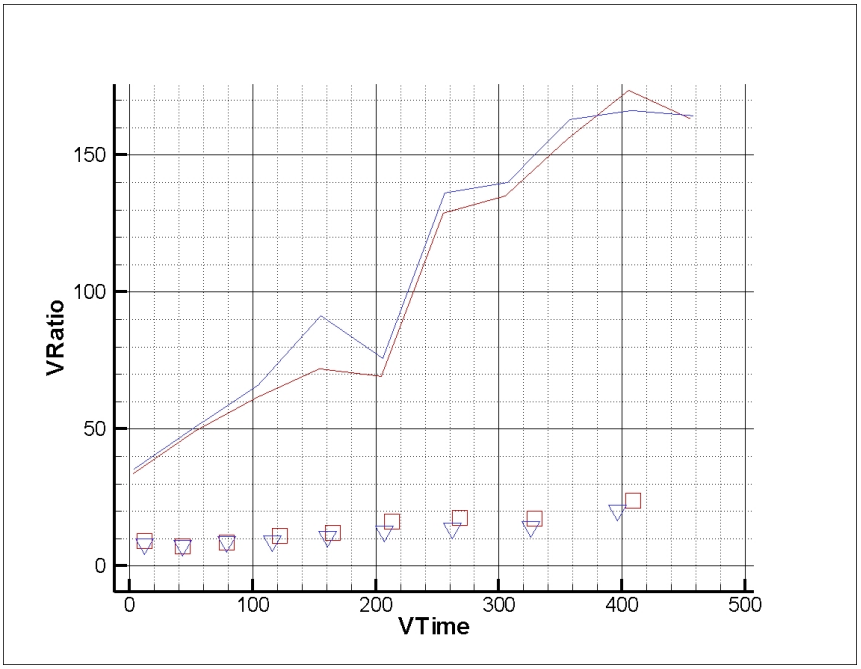

(b) Copper - Solid Glass

FIGURE 1.5.2. Snyder and Lumley Turbulence

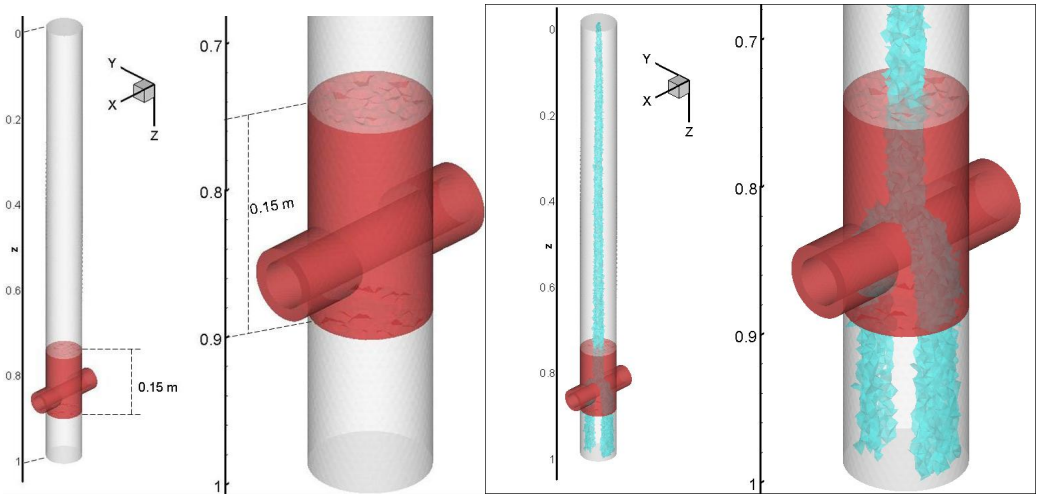

(a) Complete and Reduced domain

(b) Complete and Extracted domain: particle host cells detail

FIGURE 1.6.1. Complete and Reduced Computational Domain

particle tracking in the reduced computational domain, which contains locations one is most interested in, and where a more detailed calculation is required. A Gaussian distribution is assumed for each of the particle properties for each group of particles in a separate file, named Particle Data File (PDF), see Fig. 1.6.2. This file contains the total amount of particles as well as the particle Gaussian distributions for variables such as size, density or composition. The number of particles for particle size-class is determined according to the probability that such event may occur. Every particle represents a portion of real particles (parcel of particles)[**41**], a percentage of the total injected according to the given Gaussian distributions.

1.7. Staged Steady Particle Tracking

In this section, an interesting application of the steady particle tracking is presented. In combustion and other processes, particles may change their thermal and chemical properties, density, dimension and composition. Such processes can be investigated using a post-processing approach in two ways:

```
Particle Data File ==> PDF

TGN: 1 PNPG: 5 (Particle Number Per Group)
************************************************************
Particle Size (Diameter): (S)
Mean: 105.d-6 [m]
SD: 0.0d0 (Standard Deviation)

Particle Density: (D)
Mean: 2500.d0 [kg/m3]
SD: 0.0d0 (Standard Deviation)

Particle Composition (Acid/Base Ratio): (C)
Mean: 1.d0
SD: 0.0d0 (Standard Deviation)

Particle Specific Heat ==> PSH [J/(Kg*K)]
Mean: 840.d0 [J/(Kg*K)]
SD: 0.0d0 (Standard Deviation)

Particle Thermal Conductivity ==> PTC [W/(m*K)]
Mean: 1.d0 [W/(m*K)]
SD: 0.0d0 (Standard Deviation)

Particle Young Modulus ==> PYM [Pa]
Mean: 70.d9 [Pa] (at 300 K)
SD: 0.0d0 (Standard Deviation)

Particle Temperature ==> PTemp [K]
Mean: 300.d0 [K] ==> Mean: 0.d0 ==> means particles get inlet cell's temperature
SD: 0.0d0 (Standard Deviation)

PCN: 1 (Particle Cluster Number)
PCC: S (Particle Cluster Criteria ===> Please select S,D or C)
```

FIGURE 1.6.2. P^3 Particle Data File (PDF)

(1) implementing "hybrid" reactions[5] and tracking all the particles
(2) staging particle changes in specific zones of the simulated reactor

Ash formation and fragmentation, see Section 7.5.2.1, can be studied applying these strategies. Ash formation is usually studied with the well known one-one particle (one coal particle becomes one ash particle [**12**]) model. Using 1 requires specific reactions to be modelled whereas applying the 2 the computational domain is divided in several subvolumes and particles are tracked untill they deposit or exit the subdomain. Particles may change their properties only when a simulation is continued in the following computational subdomain: at each boundary between the two subvolumes, particle location is uploaded into the P^3code and new properties may be set in the Particle Data File (PDF,

[5]Hybrid reactions: particles may react with the flow according to the one-way fluid-particle coupling. The flow is not influenced by particle heat, gas species either released or absorbed.

Algorithm 2 Staged Particle Tracking

(1) Loop on the extracted computational subdomains
  (a) upload (next) extracted subdomain
  (b) read particle properties from previous computation or from the PDF file
  (c) particle tracking
  (d) stop particle tracking when all the particles have either deposited or exited the subdomain
(2) End Loop

see Fig. 1.6.2). The algorithm of this application is briefly reported in Alg. 2 and sketched in Fig. 1.1.6. The staging particle tracking approach 2 is a useful computational tool in simulations where:

(1) high number of cells (milions)
(2) particle thermochemical changes occur in different zones of the simulated facility and they may be grouped in several independent processes

Typically, these two requirements are fulfilled in simulations of industrial facilities as in coal and biomass boilers (see, Fig. 1.7.2), when milions of cells may mesh the computational domain and chemical processes are staged along the facilities. The staging particle tracking reduces both CPU and RAM memory use. For a stand alone PC desktop with a 2 Gb RAM, critical values[6] can be approximatly estimated in 1 milion cell mesh, tracking 2000 particles.

To verify the applicability of the staged approach, the Alg. 2 was computationally tested on a simple geometry. The staged approach was applied on a simple tube reactor (168000 cells) with a diffusive flame injecting a single class particle distribution which mimicked high silicate biomass (glass particle,s) as shown in Fig. 1.7.3. Table 1 reports the data for each of the four stages in which the tube was divided. Since the CFD simulation did not represent any specific experimental work, an unsteady particle tracking simulation was performed with a five-class particle distribution, see Fig. 1.7.4, to compare particle distribution

[6]Critical values of cells and particles represent the limit RAM memory and CPU capability to process a computation.

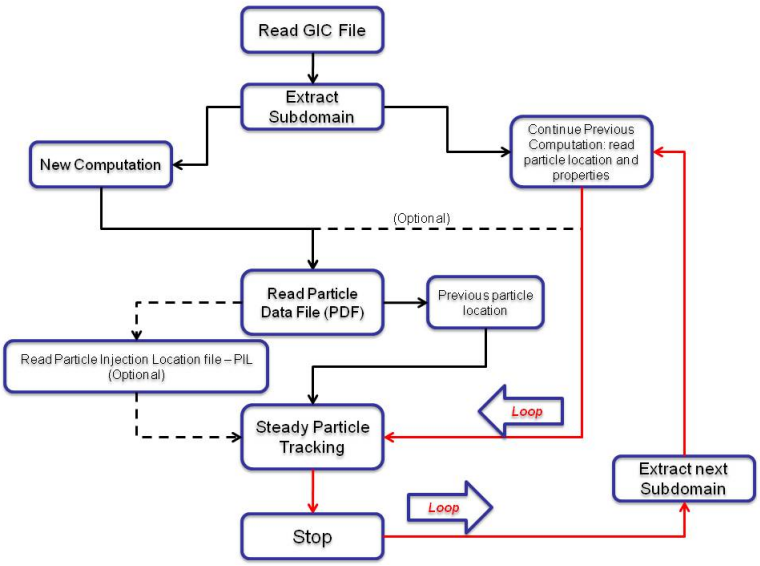

FIGURE 1.7.1. Staged Particle Tracking Algorithm Diagram

Stage	Diameter	Density	Young Modulus
1	100 μm	2500 kg/m^3	$50 \cdot 10^9$ Pa
2	75 μm	2000 kg/m^3	$20 \cdot 10^9$ Pa
3	50 μm	1500 kg/m^3	$1 \cdot 10^8$ Pa
4	5 μm	1000 kg/m^3	$1 \cdot 10^7$ Pa

TABLE 1. Tube Reactor Staged Particle Tracking, Four stage particle input data

in the staged and not staged simulations. In the unsteady particle tracking, particles keep their initial diameter and density while in the (steady) staged particle tracking, particles undergo to size and density changes as well as all the other properties. Although qualitatively, the numerical results on the staged computational tool are positively encouraging the use and the development of this application.

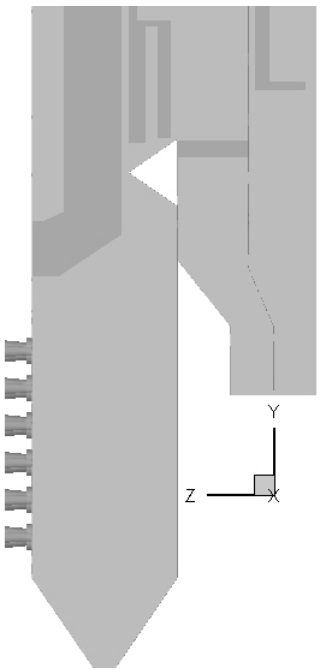

(a) Complete Boiler

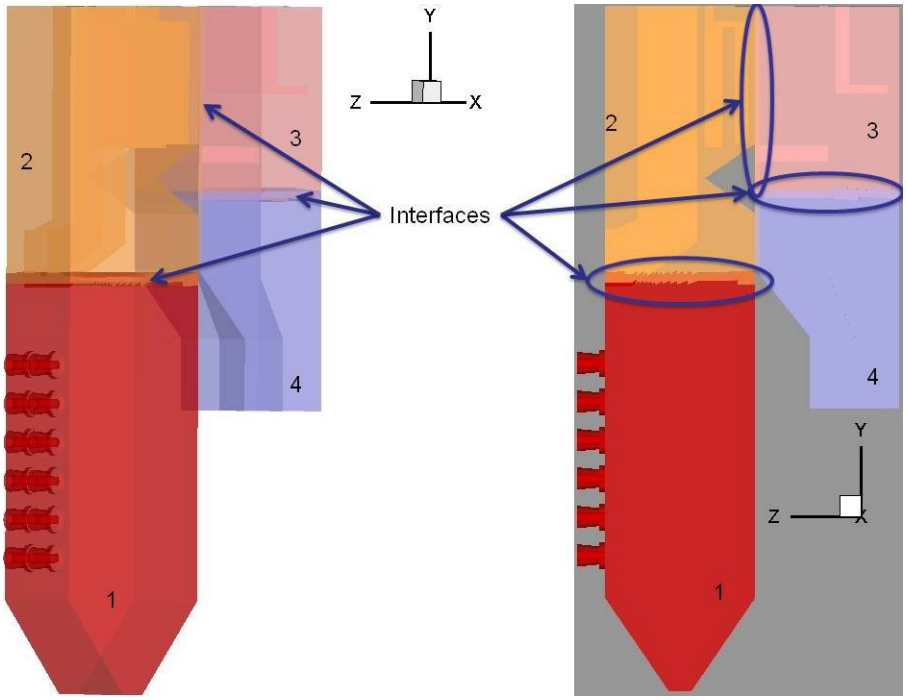

(b) Subdomain division

FIGURE 1.7.2. Staged Particle Tracking: subdomain division of a typical coal-biomass boiler facility. 1 milion cells, four independent zones for particle reaction and deposition.

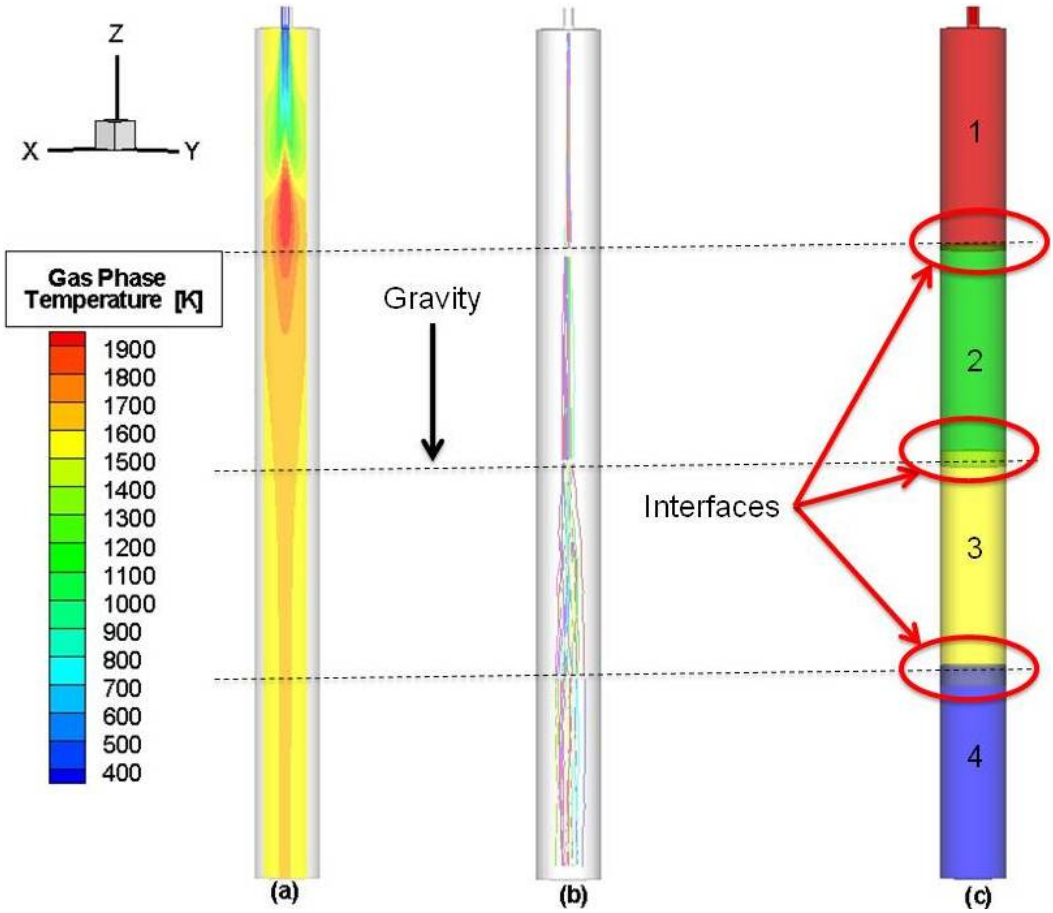

FIGURE 1.7.3. Tube Reactor (168000 cells), Staged Particle Tracking example. a) complete reactor, temperature contour, b) four staged particle trajectories, c) four staged reactor

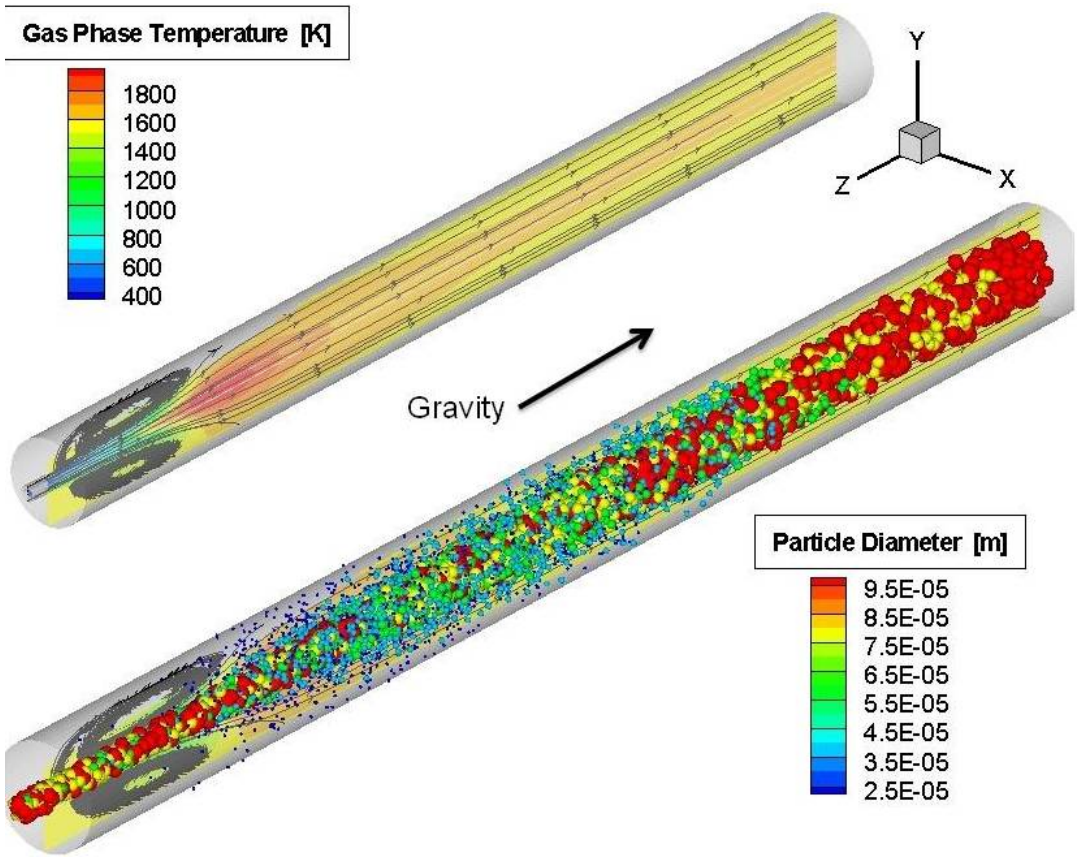

FIGURE 1.7.4. Tube Reactor, Unsteady Particle Tracking, 20 μm, 40 μm, 60 μm, 80 μm and 100 μm particles, constant density 2500 kg/m^3. Animation available on Internet at [Weblink Tube Reactor1.] and [Weblink Tube Reactor2.].

CHAPTER 2

Deposit Modeling

"...But in herself she matters more than all of you together, since it is she that I watered; since it is she that I placed under the glass dome; since it is she that I sheltered with the screen; since it is she whose caterpillars I killed... Since it is she that I listened to, when she complained, or boasted, or when she was simply being silent.

Since it is she who is my rose."

- 'The little Prince', Antoine de Saint-Exupéry.

2.1. Introduction

In this chapter the algorithms for the deposit growth, the node position displacement and the calculation for the deposit thickness, composition and thermal resistance are presented. In Section 2.2 the evaluation of the amount of mass deposited in each cell, the local node thickness and grid nodes displacement are introduced and their algorithms explained, see Alg. 3 and 4. In Section 2.3, the strategy to update deposit properties while computing the (unsteady) particle tracking (Real Time Deposit Evaluation - RTDE) and the deposit smooting technique are described.

The mathematical and computational strategy to model and take into account deposit and its mechanical, thermal and chemical properties represents one of the most important issues of this dissertation. The overall structure of the P^3 code, i.e. steady-unsteady particle tracking and the complete-reduced domain, was tailored to provide both statistics and time dependent information. Such a computational

Algorithm 3 Deposith Growth and Mesh Update, part I

(1) tag new deposit cells
(2) update list of deposit cells
(3) calculate the volume $[m^3]$ and the mass $[kg]$ of the deposit in each cell (tagged as new, step 1)
(4) upload into the P^3 the list of boundary node and cell neighbours (how many and which node/cell is next to the other)
(5) calculate the x,y and z directions for each node i
  (a) calculate the directions $\cos\theta_x|_j$, $\cos\theta_y|_j$ and $\cos\theta_z|_j$ for each boundary face j that the node i tips an edge
  (b) calculate $\cos\theta_x|_i$, $\cos\theta_y|_i$ and $\cos\theta_z|_i$ as

$$\cos\theta_x|_i = \frac{A_{tot}}{V_{tot}} \cdot \sum_j \frac{V_j}{A_j} \cdot \cos\theta_x|_j \tag{2.2.1}$$

  being V_j and A_j the mass deposited on the face j and its area whhereas $V_{tot} = \sum_j V_j$ and $A_{tot} = \sum_j A_j$ are the total deposit volume and the total area the deposit may be spread on
  (c) calculate node i deposit thickness as $thick = \frac{V_{tot}}{A_{tot}}$
  (d) calculate new node i position, x_i, y_i and z_i as $x_i = thick \cdot \cos\theta_x|_i$
  (e) calculate deposit composition and thermal resistance

characteristic represent a novelty in the particle tracking and deposition calculation. The algorithms presented in this chapter are used to numerical investigate several different application, see Chapter 7, 8, 9, 10, 11 and 12.

2.2. Deposit Growth and Node Displacement Algorithm

2.2.1. Deposit Growth.

The main algorithm to grow the deposit is divided in three parts. The first part of the algorithm tags those boundary cells containing stopped particles and calculates deposit properties at each node, see Alg. 3.

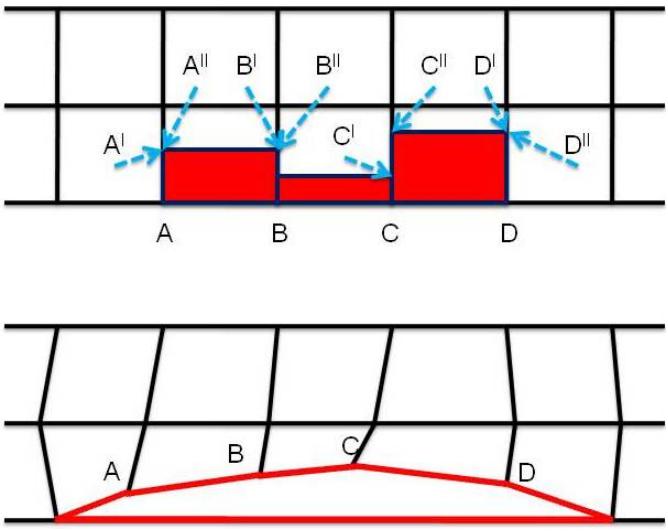

(a) Node displacement: deposit mass conservation

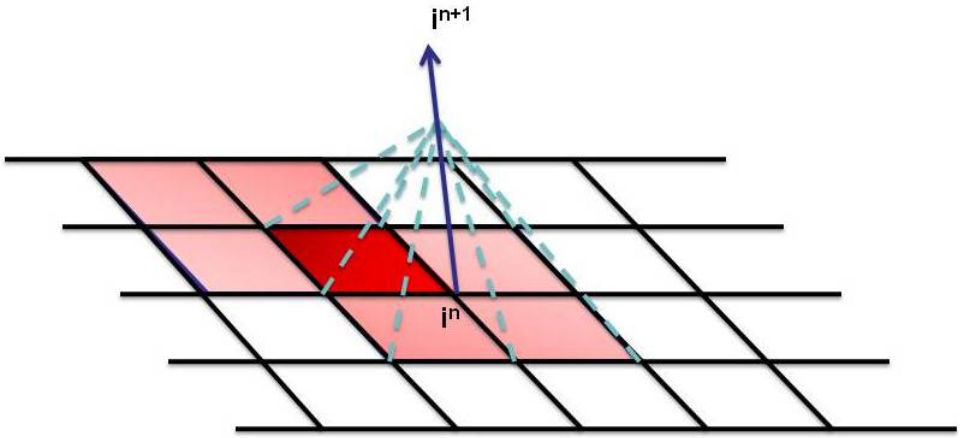

(b) Single Node "i" Displacement from time step (n) to time step (n+1)

FIGURE 2.2.1. Deposit Growth: Node Displacement

The second part concerns the internal node displacement according to the deposit. Each cell edge is modelled as a spring with a stiffness. Edge stiffness is assumed $\frac{1}{node\ distance}$, see Alg. 4.

In the third part, the files for the visual rendering in Tecplot are generated. These files allow to visualize the computational domain as well as the deposit area only or the reduced computational domain. The

Algorithm 4 Deposith Growth and Mesh Update, part II

(1) Start iteration Loop ($n = 1$ to itermax)
(2) Loop on internal nodes i
(3) Loop on i neighbour nodes j
(4) Calculate stiffness $stiff\ ij_x$, $stiff\ ij_y$ and $stiff\ ij_z$ at edge ij, $stiff\ ij_x = \frac{1}{\triangle x_{ij}}$
(5) Calculate total stiffness at node i, $stiff\ i = stiff\ i + stiff\ ij$
(6) Calculate node displacement $\triangle x_i$, $\triangle y_i$, $\triangle z_i$ at step n.

$$\triangle x_i|^n = \sum_j \frac{stiff\ ij}{stiff\ i} \cdot \triangle x_{ij}|^{n-1} \tag{2.2.2}$$

(7) End Loop on node neighbour j
(8) End Loop on nodes i
(9) Check on rms, IF $rms < 10^{-10}$, THEN $EXIT$
(10) End iteration Loop
(11) Calculate new node position $\forall\ i$, $x_i = x_i + \triangle x_i$

main problem solved in this part is to efficiently store all the deposit information and to keep track of them when a computation is restarted as well as generating the *"deposit only"* grid file as a self standing grid (see Fig. 2.2.1a), that allows animations to be recorded. In generating the *"deposit only"* file the non-trivial problem is to generate the new node connectivity for the mesh which represents the deposit shape. Since every node index number changes from the complete domain mesh to the *"deposit only"* mesh and the indeces are not sequential, it was necessary to develop a specific procedure to store efficiently such information and generate the deposit mesh without modifying the original triangular or quadrilateral shape of the 2-D elements of the boundary surface mesh.

2.2.2. Deposit Erosion.

The erosion process may be modelled using the same subroutines (algorithms) implemented for the growth. As sketched in Fig. 2.2.2, if a particle bounces off the deposit (yellow particle) and erosion conditions are fulfilled[1], two particles may be created in the same boundary cell of impaction: the first has a positive mass equal to the mass eroded (red

[1]Erosion condition may vary depending on particle kinetic and deposit-particle surface energy.

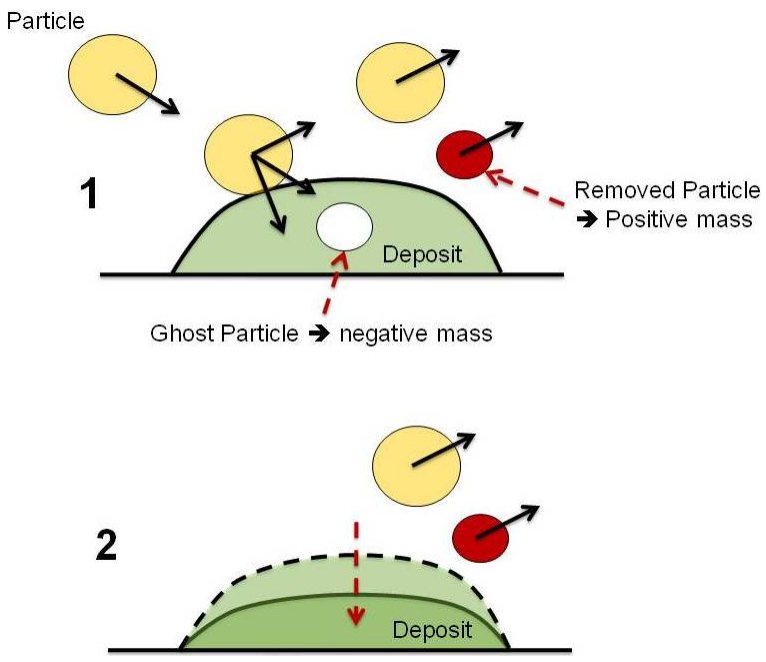

FIGURE 2.2.2. Erosion, Sketch of the algorithm

particle) and the other is a ghost particle with a negative mass (white particle). Using a negative mass particle allows to use the same set of subroutines applied for the deposit growth since the deposit volume in each cell comes out of the algebric sum as calculated in Alg. 3.

2.3. The RTDE Algorithm

Steady and Unsteady CFD calculations, such as RANS with the $\kappa-\varepsilon$ or $\kappa-\omega$ turbulence models and LES, have been used as input for the P^3 in the present work. Depending on the case simulated, the use of LES may be advisable to better evaluate the influence of turbulence (unsteady flow field) on the particle transport and deposition process. If unsteady particle tracking is required (either for RANS and LES), the deposit properties like thickness, temperature, viscosity, composition and thermal resistance (fouling factor) are evaluated during the particle tracking calculation and updated in real time to predict the changes that may occur over the deposit surface, as shown in Fig. 2.3.1. Deposit roughness is also calculated from these properties at each node. This

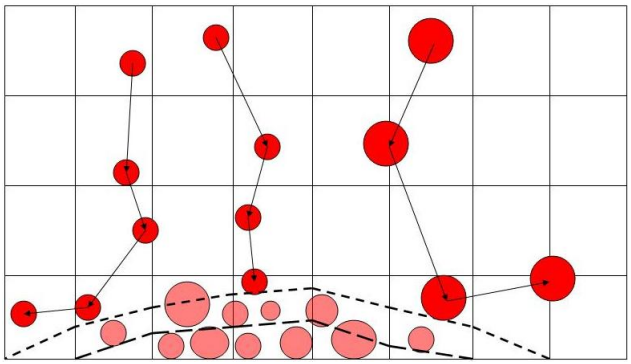

FIGURE 2.3.1. RTDE: deposit growth while particle are tracked. According to particle and deposit properties and the impact angle, a particle may either bounce off or stop (deposit).

allows modeling of the deposit growth in time. Several issues must be addressed, when implementing this approach

- the effect of the already deposited particle (deposit mechanical properties)
- the change of the impact angle, caused by the presence of the deposit
- the modified surface properties, which, according to the deposition model applied in this work, may affect the stickiness behavior of the impinging particle, see Fig. 2.3.1.

Investigating particle deposition in unsteady flow fields (LES) by simulating the real time interval of the experiment in most cases is computationally too expensive. To overcome the problem of how long the simulated time should be, a Deposit Evaluation Coefficient (DEC) is used. The deposit thickness growth rate is multiplied by this coefficient to express that to a numerical time step corresponds a longer time internal in the experiment. This coefficient increases the deposit thickness prediction at each time step using a linear approximation for the deposit history. If a numerical simulation of N time steps Δt_{num} is to represent an experiment of duration Δt_{exp}, the DEC coefficient is give by eq. 2.3.1, as follows:

$$DEC \simeq \frac{\Delta t_{exp}}{N \cdot \Delta t_{num}} \tag{2.3.1}$$

$$DT_i^{n+1} = \sum_{j=1}^{s} DEC \cdot \frac{\left(D_j^{n+1} - D_j^n\right)}{A_j} \tag{2.3.2}$$

$$cos\theta_x|_i = \frac{1}{DT_i^{n+1}} \sum_{j}^{s} cos\theta_x|_i|_j \cdot \frac{\left(D_j^{n+1} - D_j^n\right)}{A_j} \tag{2.3.3}$$

where Δt_{exp} is the experimental time, Δt_{num} is the CFD time step and N is the number of unsteady flow field frames available. n identifies the time step, D, DT and A_j represent respectively the deposit volume in m^3, the deposit thickness in m and the deposit area of the cell j on the total number s of neighbour cells which have the node i in common. $cos\vartheta_x$ represents the direction the node i will be displaced along, see Fig. 2.3.2. Deposit properties are evaluated and the mass represented by each particle is assumed homogeneously distributed on the cell's wall surface. As shown in Fig. 2.3.2, the numerical output given by the code is calculated as the distance between the new and the old node position, while it should be calculated as the distance normal of the node i from the surface area the projected node is contained within. For small time deposit update interval, the difference between the two results is substantially negligible. Certainly, reducing the time deposit update interval reduces the error introduced.

Afterwards, and according to a particle scatter coefficient, see Section 2.3.1, the deposit thickness at each node is calculated according to wall surface area of the cell and its neighbors (see Fig. 2.3.1). An example of deposit growth on a pipe is given in a few snapshots in Fig. 2.3.3: the deposit growth (thickness) is locally predicted and the deposit properties, such as viscosity and composition, are (constantly) updated during the run of the simulation.

2.3.1. Smooting Algorithm.

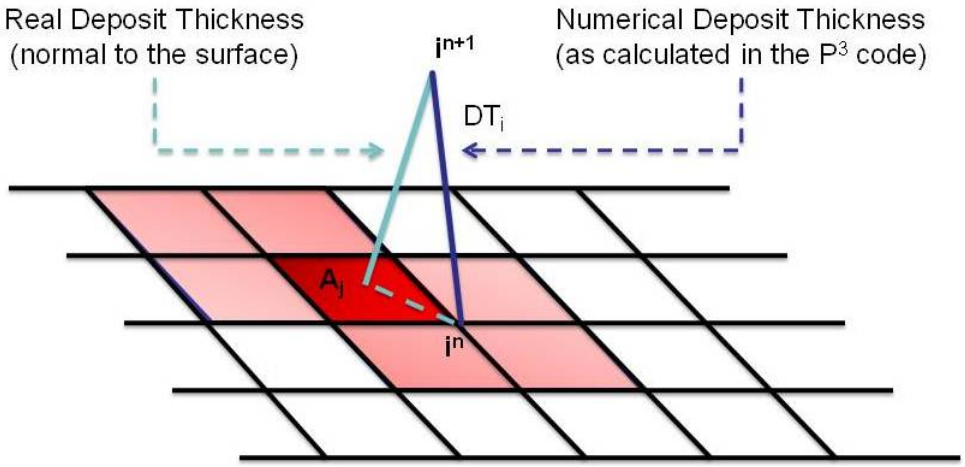

FIGURE 2.3.2. Deposit Thickness: Real and Numerical P^3 results

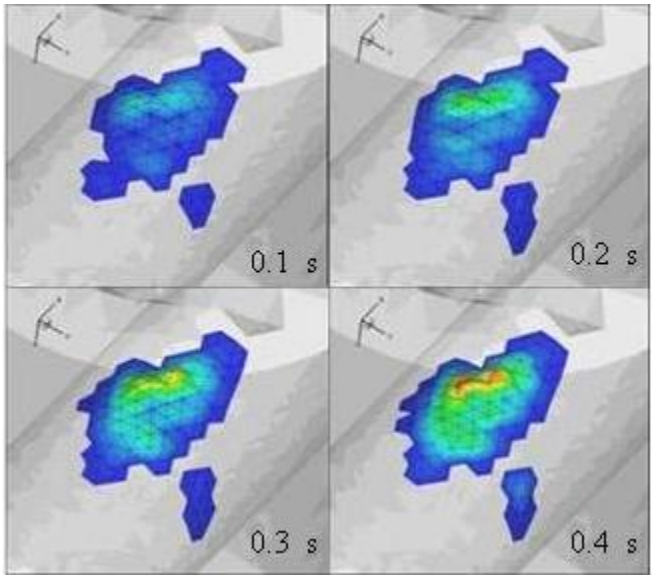

FIGURE 2.3.3. Deposit growth at 0.1 s, 0.2 s, 0.3 s and 0.4 s. Real time deposit evaluation enabled.

Usually the number of particles to be tracked depends on the fluid turbulence level and the given particle distribution, and it is chosen so as to minimize the computational time. Reducing the number of particles to save CPU time in a domain with fine mesh at the boundaries may alter the numerical prediction of the thickness, thermal properties

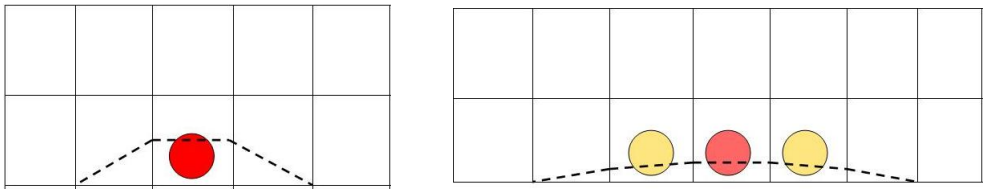

(a) (b)

FIGURE 2.3.4. Scatter coefficient: a) scatter coefficient = 0.0, b) scatter coefficient $\leq$ 1.0 with neighbour ghost particles. It results in a smoother surface deposit.

and location of the deposit, since the mass represented by each parcel particle may deposit on an area narrower then in reality (e.g., walls, where CFD boundary conditions require a detailed computational resolution). In fact, this problem may arise every time the total number of particles or the number of the particle size-classes of the Gaussian distribution are not (statistically) representative, and leads to unrealistic peaks of thickness. To lower such error, a smoothing empirical non-dimensional coefficient can be introduced to numerically scatter part of the deposit to neighbour cells. This scatter coefficient Sc is in the range $0-1$. If $Sc = 0$, the deposition is calculated as mentioned above; if $0 < Sc \leq 1$ then the mass represented by the particle is distributed according to the scatter coefficient into *"ghost"* particles dwelling in the neighbour cells (see Fig. 2.3.4).

In the case of maximal smoothing ($Sc = 1$) the volume deposited is equally distributed between the original cell and its neighbour cells. Assuming that the cell j has 8 neighbour cells, the volume of the mass deposited in each cell will simply be $Vol_j|_{Sc=1} = \frac{Vol_j|_{Sc=0}}{8+1}$. scatter coefficient can be computed as in eq. 2.3.4:

$$Sc \propto k_c \cdot \frac{m_{parcel}}{M_{tot}|_{exp}} \cdot \frac{A_{tot}}{\bar{A}_{cell}} \propto \frac{No.dep.cells}{No.parcels} \tag{2.3.4}$$

where Sc is the scatter coefficient, $m_{parcel}$is the mass represented by the parcel particle, $M_{tot}|_{exp}$ is the total mass injected, A_{tot} is the total impinging area (frontal area of bundles of tubes, for instance)

and $\bar{A}_{cell}$ is the main cell area dimension. k_c is a correction coefficient that should be empirically estimated to correct the uncertainty that may be introduced in the calculation of A_{tot}, which can usually only roughly estimated. It is to be noticed that the ratio $\frac{A_{tot}}{\bar{A}_{cell}}$ represents the total amount of cells candidate for deposition. Paradoxically, due to an error compensation, without scattering, a coarse CFD mesh in conjunction with statistically insufficient amount of tracked particles might provide a result closer to the experimental results than a calculation performed tracking the same amount of particles and using a finer mesh. The deposit thickness depends on both the total amount of deposited mass and the discretization (mesh) of the deposit location: reducing the number of computational particles increases the mass that such parcel of particle represents. Therefore, there is a little statistical error in the total amount of the deposited mass. However, with fewer particles (parcels) there will be higher statistical error in the location of the deposit (spatial distribution). To overcome this modelling problem, and assuming that the mesh is suitable to correctly describe the fluid dynamics calculated in the commercial CFD code, two options may be applied: a) to increase the number of particle (raising CPU time) or b) to set the scatter coefficient $Sc > 0$ and to slightly increase the amount of particles (lowering CPU time). Eventually, if the deposit thickness is one of the results expected from the simulation, the number of particles selected must be suitable to correctly describe deposit behavior comparted to the boundary discretization (boundary cell number) and configuration as well as statistically representative of the dispersion in flow due to the turbulence and the given distribution (i.e. mean and variance in case of Gaussian distribution). Certainly a fundamental remark may be addressed concerning the definition of this empirical coefficient: although this is a global coefficient, the need for smoothing the deposit shape is indeed a local property depending on the location. However, the deposit smoothing technique here presented concerns only the neighbor cells (see. Fig. 2.3.4). The widening or extent of the deposit area could be better calculated if the physics

of the problem were taken into account. For istance, assuming a viscoelastic model, see Chapter 3, that may mimic the shape deformation according to temperature, composition, surface energies of the impinging particle and the deposit surface (surface tension for almost-liquid particles) and their viscosities.

Part 2

Particle Mathematical Modeling and Validation

CHAPTER 3

Viscoelastic Solids

"The mountains flowed before the Lord."[1]

Song of Deborah, Bible, Judges 5:5

Modeling adhesion of solid bodies which may change, shape, composition ad mechanical properties in time may require a little information about their history. Solid materials under thermal stress and gradients may change their shape and mechanical properties or changing phase becoming liquid. Since every material has a melting temperature, depending on both the present condition and its history any solid may soften showing a viscous liquid-like behavior. During this transition, a solid acts in between being in a liquid and a solid state, named viscoelastic. In general, every solid show a viscous flow motion in a long time. That is the sentence reported above: only The Lord can see mountains flowing.

In combustion cases, particles undergo through several processes that may induce viscoelastic behaviour to occur. Viscoelastic models seem appropriate to reproduce more in detail anelastic particle impactions and adhesion, since these phenomena may be explicited in terms of mechanical and thermal properties, i.e. Young modulus and surface energy/tension.

[1]There are a few different translations from original language version. Mostly it is translated as "flowed ", "melted" , rarely as "quaked" or even "gushed". The meaning used by Prof. Markus Reiner, who coined the name of the dimensionless Deborah's number, was that even mountains have a flow motion, so slow that it may appear only before God.

3.1. Introduction to Viscoelasticity

Considering the mechanical response of a solid material to stress or strain, materials can then be gathered into three main categories:

(1) Elastic
(2) Viscoelastic
(3) Viscous

Solid materials' behaviors are mostly described by the Young (elastic material) or stress relaxation modulus $Y(t) = \frac{\sigma(t)}{\varepsilon}$ and the compliance modulus $J(t) = \frac{1}{Y(t)} = \frac{\varepsilon(t)}{\sigma}$. In linear materials, Y and J are independent of the strain level, so $Y = Y(t)$ and $J = J(t)$. Elastic materials show an "immediate" recovery from any stress or strain state applied, which can be accurately represented by the Young modulus E. On the contrary, creep viscous behaviour is better represented by the compliance modulus J. Viscoelastic materials exhibit creep[2], stress relaxation[3] and recovery as a function of time[4]. Depending on the (experimental) response of the material, E or J can be used to describe dynamic behaviour[5]. Stronge[**3**] and Lakes[**13**] report some examples of creep, relaxation and material elastic response or compliance. For elastic materials, stress and strain are described by $\sigma = Y \cdot \varepsilon$ and $\varepsilon = J \cdot \sigma$ where ε and σ are respectively strain and stress. A viscous fluid can be represented by $\sigma = \eta \frac{d\varepsilon}{dt}$ where η is the viscosity. Anelastic solids[6] can be considered as viscoelastic materials since they have a unique equilibrium configuration and may eventually fully recover after load removal. Solid particles which go through temperature gradients or changes in composition or size (as in combustion) show indeed some anelastic behaviour and undergo thermal stresses.

[2]Creep: slow process, progressive deformation of a material under constant stress applied
[3]Stress relaxation describes how materials relieve stress under constant strain
[4]Viscoelastic materials are those materials having a relation between stress and strain as time dependent[**3, 13**]
[5]Full knowledge of the viscoelastic response of material is based on experimental measurements[**3**].
[6]Anelastic materials: viscoelastic materials which exhibit complete recovery after a sufficient time following creep or relaxation

Indeed, all materials show viscoelastic behaviour[**3**]. The time scale to notice the flowing/shear motion determines to which extent a solid can be considered viscoelastic[7]. The dimensionless *Deborah* number documents this concept:

$$Da = \frac{creep/relaxation\ time}{observation\ time} \tag{3.1.1}$$

Generally, springs and dashpots variously connected are used to model viscoelastic and anelastic behaviour. Only by knowing either the stress or the strain distribution (in time) of a material it is possible to select a correct set of spring-dashpots to provide an accurate model.

The constitutive equation analysis provided by Stronge [**3**] refers to linear and non-linear one dimensional isothermal viscoelastic materials. Such approach can still be considered valid for homogeneous spherical particles as long as the temperature effect is properly taken into account. Since temperature acts on viscosity, an accurate viscosity prediction is required. How the temperature T and composition c influence the viscosity, as $\eta = \eta(c, T)$, may be provided by means of interpolation functions. In this work, the solution proposed by Senior and Srinivasachar [**11**] is applied.

3.2. Viscosity Closure Algorithm

The calculation of the mechanical properties of a particle in the computer software requires a closure algorithm based on some assumptions. The closure in the present model may be synthetized as reported in Alg. 5.

The following assumptions are made in this work:

(1) Particle temperature is assumed to be constant along the path between location A and B
(2) The viscosity formulation $\eta = \eta(c, T_{P_B})$:
    (a) predicts the particle viscosity at equilibrium[8] $\eta = \eta_{eq}$

[7]As long as any solid can be considered having a viscoelastic response, a very low viscoelastic response returns an elastic behavior whereas a very high viscoelastic response makes the solid to be considered as viscous.
[8]Thermo-chemical equilibrium

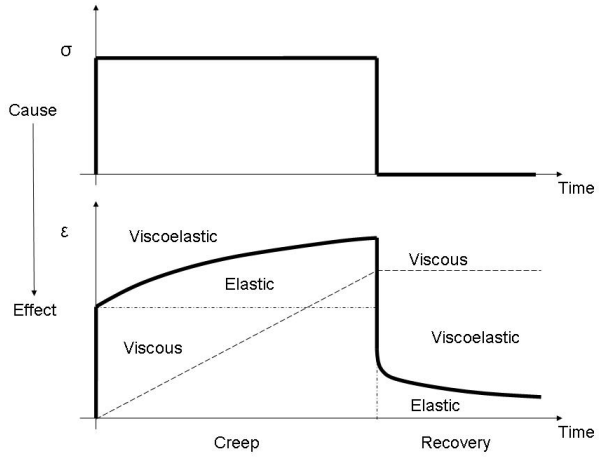

(a)

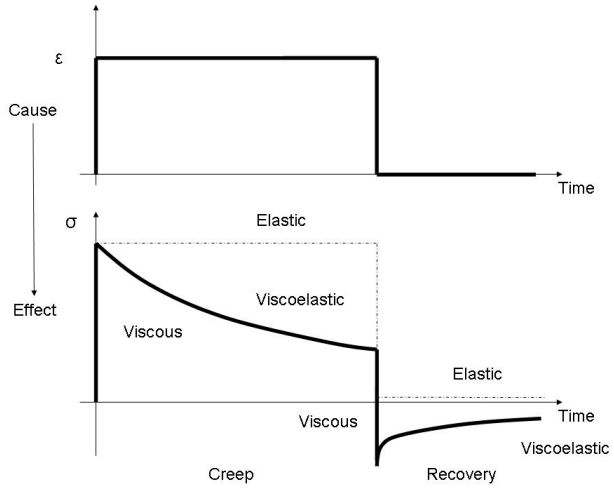

(b)

FIGURE 3.1.1. Creep and Stress Relaxation: a) Creep and recovery, b) Stress Relaxation and recovery. Source Stronge[**3**].

(b) the viscosity η_{eq} is assumed as *bulk* viscosity

(3) The time dependent formulation $Y = Y(\eta, t)$ implies that the mechanical response of the relaxation modulus to a thermal stress is slower than the viscous response given by the time

Algorithm 5 Viscosity Closure Algorithm

(1) Particle time integration: selection of the time step dt

(2) Particle new position (x_B, y_B, z_B), from location A to B

(3) Particle new temperature T_{P_B} (conduction only, Fourier law): calculated assuming residing for a time dt at a constant gas phase temperature T_A before reaching location B

(4) Particle viscosity $\eta = \eta\left(c, T_{P_B}\right)$

(5) Y (or, similarly J) modulus update as $Y = Y\left(\eta, dt\right)$, according to the integration time step (which represents the time frame the particle has been residing at the temperature T_A) and the viscoelastic model selected

$t_\eta = \frac{\eta}{\rho \cdot C \cdot \Delta T}$, where ρ, C and T are respectively, density, specific heat and temperature of the solid material.

(4) Particle heat exchange with the surroundings is limited to conduction only.

The equilibrium viscosity approach $\eta = \eta\left(c, T\right)$ may either overpredict (if $\Delta T > 0$) or underpredict (if $\Delta T < 0$) the softening of the solid[9]. As complementary solution, particle temperature is usually underpredicted since no radiation is taken into account. Indeed, a more correct approach would require a time dependent viscosity formulation $\eta = \eta\left(c, T, t\right)$, tailored for a range of composition. In this work, particle viscosity was calculated by the use of the interpolation function proposed by Senior and Srinivasachar[**11**] which extended the well known Urbain[**58**] model $\eta = \eta\left(c, T\right)$ for a wider range of compositions as well as increasing the accuracy of the model type[10].

[9]This statement for the softening works for the hardening for opposite temperature gradients: overpredicting the hardening, if $\Delta T < 0$, and underpredicting for $\Delta T > 0$.

[10]The Senior and Srinivasachar interpolation extended the model proposed by Urbain, by a)widening the range of composition, b)increasing the number of experimental sample for the mathematical regression fitting, 3)using multiple interpolation functions to calculate the logarithmic regression line coefficients A and B.

3.3. Relaxation and Compliance Modulus

Mechanical collision and adhesion of elastic-plastic solid spheres under thermal stress represent one of the main topics of this dissertation, even though neither particle size reduction nor dilatation due to temperature gradients was taken into account. Combining various springs and viscous dashpots may model almost any material creep and relaxation behavior. While springs mimic the elastic restitution to stress, a viscous dash-pot accounts for the energy dissipation which may occur due to material properties. In general, any kind of stress or strain can be modelled with a combination of spring and dashpots as long as their combination and the values of the coefficients and parameters required by the model are representative of the response of the material. In this work, six models have been implemented but only four of them have turned relevant for the simulation performed. Therefore, only these four models are presented, tested and used in this dissertation. In literature, the ratio $\frac{\eta}{Y}$ is addressed as the (viscous) relaxation time τ_r. In Fig. 3.3.1 and Fig. 3.3.2, the models implemented in the software and their behaviors are presented.

(1) Maxwell, Fig. 3.3.1(a):

$$\begin{cases} Y(t) = Y_1 \cdot \exp\left(-\frac{t}{\eta_1/Y_1|_{t=0}} \cdot \frac{\Delta T_1}{|\Delta T_1|}\right) \\ Y(t=0) = Y_1 \\ \lim_{t\to\infty} Y|_{T=T_1} = 0 \end{cases} \tag{3.3.1}$$

(2) Voigt, Fig. 3.3.1(b):

$$\begin{cases} Y(t) = \frac{Y_1}{\left[2-\exp\left(-\frac{t}{\eta_1/Y_1|_{t=0}} \cdot \frac{\Delta T_1}{|\Delta T_1|}\right)\right]} \\ Y(t=0) = Y_1 \\ \lim_{t\to\infty} Y|_{T=T_1} = \frac{Y_1}{2} \end{cases} \tag{3.3.2}$$

(3) Standard Linear Solid (SLS), Fig. 3.3.1(c):

$$\begin{cases} Y(t) = Y_1 + Y_2 \cdot \exp\left(-\frac{t}{\eta_2/Y_2|_{t=0}} \cdot \frac{\Delta T_2}{|\Delta T_2|}\right) \\ Y(t=0) = Y_1 + Y_2 \\ \lim_{t\to\infty} Y|_{T=T_2} = Y_1 \end{cases} \tag{3.3.3}$$

(4) Four elements: Maxwell-Voigt in serie, Fig. 3.3.1(d):

$$\begin{cases} Y(t) = \frac{Y_1 Y_2}{\left[Y_2 + Y_1 Y_2 \frac{t}{\eta_1} \frac{\Delta T_1}{|\Delta T_1|} + Y_1\left(1 - \exp \frac{t}{\eta_2/Y_2|_{t=0}} \cdot \frac{\Delta T_2}{|\Delta T_2|}\right)\right]} \\ Y(t=0) = Y_1 + Y_2 \\ \lim_{t\to\infty} Y|_{T=T_2} = 0 \end{cases} \tag{3.3.4}$$

The constitutive equations 3.3.1, 3.3.2, 3.3.3 and 3.3.4 are obtained either by compliance, assuming as valid Boltzmann superimposing condition (total deformation $\varepsilon_{tot} = \sum_i \varepsilon_i$) or relaxation (total stress $\sigma_{tot} = \sum_i \sigma_i$). For the Maxwell model[11], for instance:

$$\begin{cases} \varepsilon_{tot} = \varepsilon_{spring} + \varepsilon_{dashpot} \\ \sigma_{tot} = \sigma_{spring} = \sigma_{dashpot} \end{cases} \tag{3.3.5}$$

$$\begin{cases} \frac{d\varepsilon}{dt} = \frac{d\varepsilon_s}{dt} + \frac{d\varepsilon_d}{dt} \\ \varepsilon_s = \frac{\sigma}{Y} \\ \varepsilon_d = \frac{\sigma}{\eta} \cdot t \end{cases} \tag{3.3.6}$$

which gives $Y\frac{d\varepsilon}{dt} = \frac{d\sigma}{dt} + \frac{\sigma}{\tau_r}$ with $\tau_r = \eta/Y$. Integrating in time, $Y(t) = Y|_{t=0} \exp^{-\frac{t}{\tau_r}}$ which simply returns the eq. 3.3.1.

The Maxwell model 3.3.1 and the Voigt model 3.3.2 can be considered fundamental, or academic, models to mimic relaxation (Maxwell Model) and creep (Kelvin-Voigt Model). Experimental data are indeed necessary to correctly set the parameters Y_i and η_i for all the elements used in each model. The scarce availability of this kind of information is essentially due to the strong dependency on the material thermal and mechanical history and composition, a fact that makes the collection

[11] In the Maxwell model, deformation is assumed quasistatic, inertia is not considered and the stress applied is the same on both the two elements[**3, 23**].

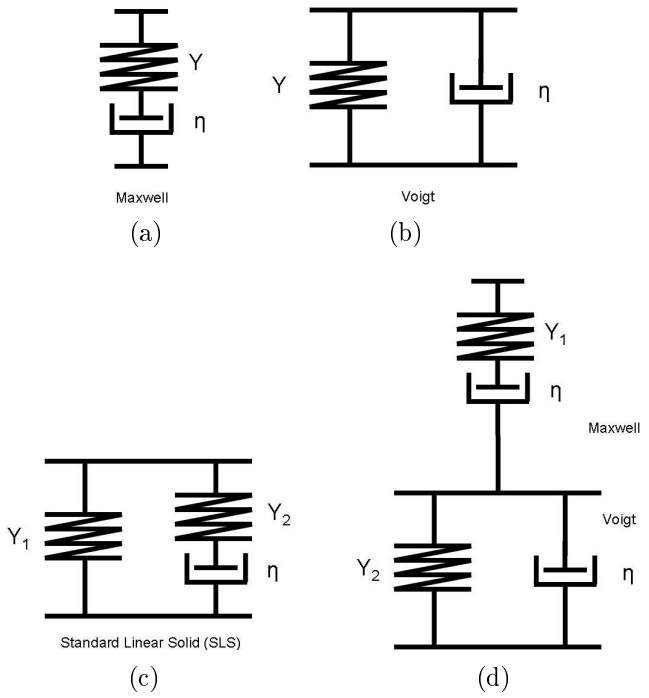

FIGURE 3.3.1. a) Maxwell Model, b)Voigt Model, c)Standard Linear Solid Model (SLS), d)Four Elements

of such parameters certainly difficult [**53**]. In Fig. 3.3.3 the relaxation behaviour of the four models is shown at high temperature[12]. It is to be noticed that the SLS model is the stiffest whereas the four-elements is the softest one. The conditions listed in eq. 3.3.7 and eq. 3.3.8 have been used respectively for the SLS and the four-element models.

$$\begin{cases} Y_1 = (0.25 - 0.5) \cdot Y|_{t=0} \\ Y_2 = (0.75 - 0.5) \cdot Y|_{t=0} \\ \eta = \eta_{bulk} \end{cases} \tag{3.3.7}$$

[12]High temperature condition: when mechanical properties start decreasing rapidly. It usually happens in when $T > T_g - [100 - 200\,K]$, where $T_g$stands for glass transition temperature

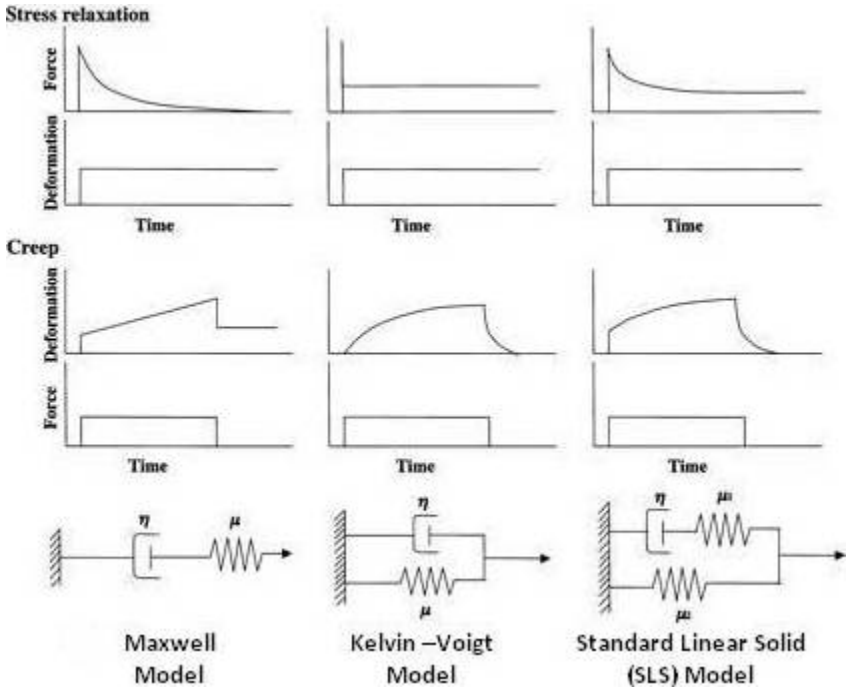

(a) Maxwell, Voigt and Standard Linear Solid relaxation time behaviour

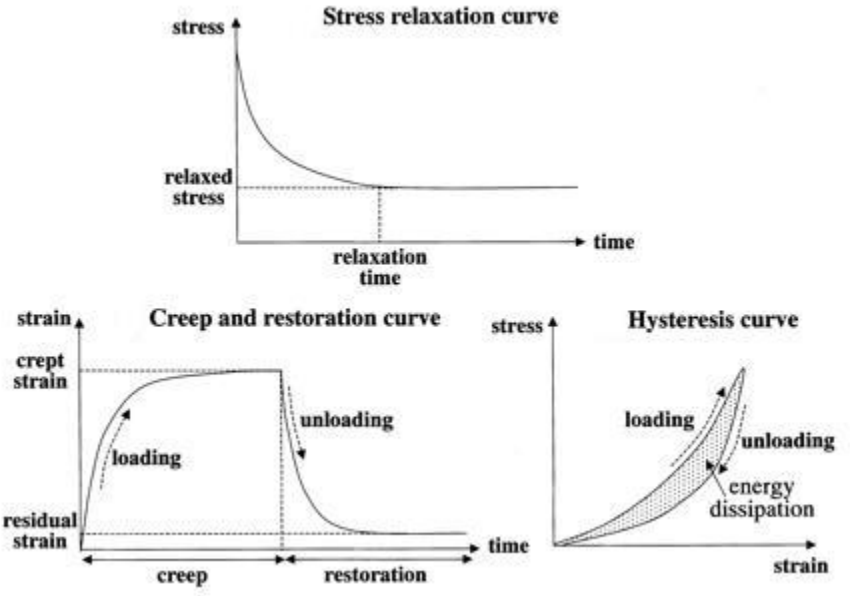

(b) Maxwell model time, load and hysteresis behaviour

FIGURE 3.3.2. (a) Viscoelastic Models. (b) Creep and stress behaviour. Source [**53**]

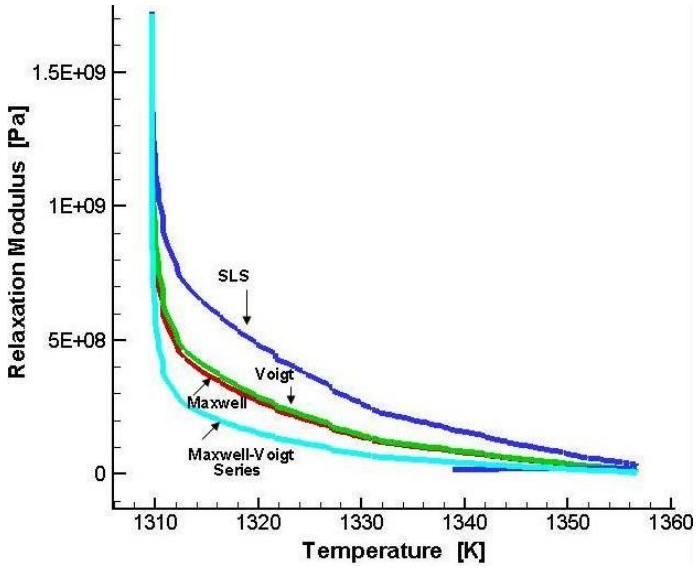

FIGURE 3.3.3. High Temperature conditions. Relaxation modulus for solid glass particles. Maxwell, Voigt, SLS and Four element models

For the four-element model, it has been used

$$\begin{cases} Y_1 = Y_2 = Y|_{t=0} \\ \eta_1 = \eta_2 = \eta_{bulk} \end{cases} \tag{3.3.8}$$

For the i element, if the temperature difference is $\Delta T_i > 0$, then the relaxation modulus decreases (softening process), if $\Delta T_i < 0$ then the material hardens up (hardening process). Thermal stresses may induce hysteresis on the relaxation modulus (anelastic loss) consistently lowering the bulk hardening. To account for the hysteresis due to thermal stress, if $\Delta T_i < 0$ the four-element approach (the more complex and CPU-intensive amongst all the models implemented) is then selected. Fig. 3.3.4 shows the high temperature thermal hysteresis cycle of the SLS and the four element model. The area between the two curves indicates the mechanical loss (anelastic) due to thermal hysteresis. For instance, the coiling process of metals and glasses is severely controlled

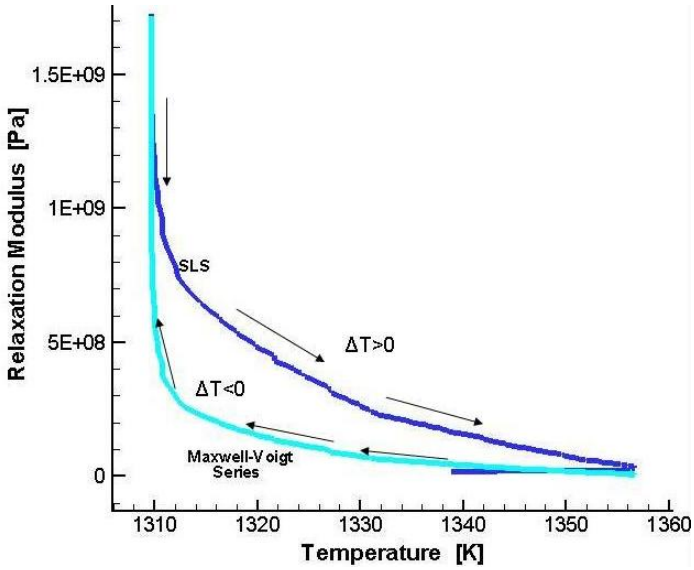

FIGURE 3.3.4. High temperature hysteresis cycle. A hot particle cooling down and heating up will not gain the same elastic condition due to intrinsic anelastic behavior.

to prevent the manufactured product to have undesired flaws and unpredictable mechanical properties. For glass particles (see results reported in Chapter 7), the Maxwell model was used for $\Delta T > 0$ while the four-element model was used for $\Delta T < 0$.

CHAPTER 4

Adhesion and Contact Mechanics of Solid Particles

"It is better to separate
than having never met at all..."
- Gustave Flaubert.

Hertz (1928), Bradley (1932) and Davies (1949) pioneered the mathematical description of the contact mechanics of elastic solids spheres and the principles of dry adhesion. Indeed two solids may adhere to each other as long as *"enough"* energy is provided to overcome their *"reluctance"*, or surface energy barrier. In other words, any two-body system is characterized by a energy threshold level that must be overcome either to have the two bodies stick together, or to separate them from each other. This energy is called *work of adhesion - separation.* The *"work of adhesion"* w, was introduce by Bradley as the energy per unit contact area required to separate the two solids. Nominally, there is no difference between work of adhesion and work of "separation" (Griffith, 1920) of two distinct but joined solids, since the work of adhesion is measured experimentally as the energy required to separate them, applying a pull-off force P_c. The work of adhesion w is defined by the Young-Dupré equation[1]

$$w = \gamma_1 + \gamma_2 - \gamma_{12} \tag{4.0.9}$$

where γ_1, γ_2 and γ_{12} are respectively the surface energy of the two solids and the interface. In literature either Γ or w as symbols can be found for the work of adhesion and the surface energy. Usually, Γ is

[1]As reported by Maugis [**19**].

used if $\gamma_{12} = 0$ between the solids, therefore $\Gamma = \gamma_1 + \gamma_2$ [**65, 52**]. The surface energy and the strength of adhesion between elastic bodies are certainly, but not obviously, related to the action of surface forces. In order to separate bodies in contact, mechanical work must be expended to overcome the adhesive forces and create a "new" surface. The energy required to create one unit area of a new contact surface can be defined as the free surface energy of the solid. In liquid-solid surface contacts, the final contact size at equilibrium may be predicted from surface energy considerations. For instance, the spreading or contracting of one liquid surface over another or over a solid to reach an equilibrium is dominated by the minimization of the surface energy.

In the decade $1970-80$, an interesting competition in the academic field began to be played between U.K and Russia. The controversy was on the modelling of the adhesion of spherical solids which arose in that period between Cambridge and Moscow University. The argument was about which of the two formulations known as JKR (Johnson-Kendall-Roberts)[**15**] and DTM (Derjaguin-Muller-Toporov)[**16**] theory, proposed respectively by Johnson in 1971 and by Derjaguin in 1974, was the superior one. This quite acrimonious debate was eventually solved by Tabor in 1977, who demonstrated that both theories were equally correct. In short, these theories were describing the same phenomenon (spheres adhesion) of two different spheres, at the opposite edges of the same adhesion scale. To briefly summarize, the DMT theory applies to hard while the JKR theory applies to soft spheres. Tabor demonstrated such a statement by introducing the non-dimensional parameter μ (see eq.4.0.10), pointing out the limiting assumption of each theory. This parameter may be interpreted as the ratio of the elastic deformation to the range of action of the adhesive forces. Therefore, large values of μ correspond to large radius compliant solids (the JKR model) and small values to small rigid solids (the DMT model):

$$\mu = \left(\frac{R^* w^2}{Y^{*2} z_o^3} \right)^{\frac{1}{3}} \tag{4.0.10}$$

where the equivalent Young modulus Y^* is $\frac{1}{Y^*} = \frac{1-\nu_1}{Y_1} + \frac{1-\nu_2}{Y_2}$, z_o is the equilibrium spacing and R^* is the equivalent radius of the two spheres defined as $\frac{1}{R^*} = \frac{1}{R_1} + \frac{1}{R_2}$. Concerning the equilibrium spacing, it is common to refer to the Lennard-Jones potential between the force p and the separation z:

$$p(z) = \frac{8w}{3z_0}\left[\left(\frac{z}{z_0}\right)^{-3} - \left(\frac{z}{z_0}\right)^{-9}\right] \tag{4.0.11}$$

Maugis investigated the intermediate regime between JKR and DMT, proposing in 1992 the so called *"continuum theory of adhesion"*[**19**] which describes both wet (non-chemical adhesive liquid meniscus only) and dry adhesion in respect with two parameters, the elasticity λ and the load parameter $\overline{P}$

$$\lambda = \sigma_0 \left(\frac{R^*}{2\pi w Y^{*2}}\right)^{\frac{1}{3}} = 1.16 \cdot \mu \tag{4.0.12}$$

$$\overline{P} = \frac{P}{\pi w R^*} \tag{4.0.13}$$

The Maugis model, better known as Maugis-Dugdale (Dugdale model by analogy with the Dugdale model for elastic-plastic cracks) assumes the force σ_0 to be constant up to the maximum separation h_0, beyond which it goes to zero. Therefore, in the Maugis approximation, $w = \sigma_0 h_0$ which returns $h_0 = 0.97{z_0}^2$ as reported by Johnson [**65**] (see Fig.4.0.1).

As shown in Fig.4.0.2, for $\mu \ll 1$ (hard solids of small radius and low surface energy) one has the DMT theory and for $\mu \gg 1$ (soft materials with large surface energy and radius) the JKR theory (see Table 1). Furthermore, JKR assumed that the cohesive zone[3] was infinitesimally small. Likewise, the DMT theory assumed an Hertzian

[2]In order to give the same value as Lennard-Jones requires.
[3]cohesive zone: area just outside the region of intimate contact that is subjected to adhesive traction

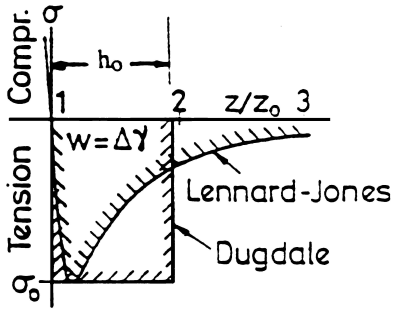

FIGURE 4.0.1. The Maugis-Dugdale Model in comparison with Lennard-Jones, from Johnson 1998[**65**]

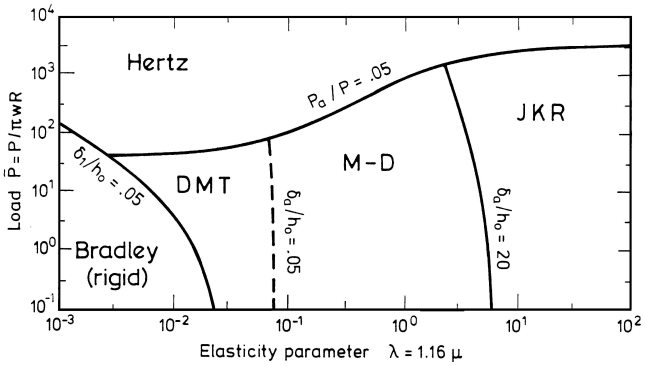

FIGURE 4.0.2. Continuum adhesion map, Johnson and Greenwood[**18**]

profile[4] distribution for the contact stress in the cohesive zone, see Appendix A.

However, the pull-off force normal to the contact area predicted by the DMT theory is

$$P_c = 2\pi w R^* \tag{4.0.14}$$

whereas, in the JKR theory, it is:

$$P_c = \frac{3}{2}\pi w R^* \tag{4.0.15}$$

Further details on contact mechanics, JKR, DMT and Maugis theories are reported in the Appendix A. However, interesting, extensive

[4]parabolic stress distribution which goes to zero at the border of the cohesive zone.

DTM	Maugis	JKR
hard solids small contact radius	*Adhesive regime between JKR and DMT theories*	*soft solids large contact radius*

TABLE 1. Adhesive contact of elastic spheres. JKR, DTM and Maugis qualitative comparison

and detailed reviews on the historical background of the mathematical controversy on the adhesion theory can be found in works written by Johnson, Maugis, Muller and Greenwood. In particular, Derjaguin[**16**] gives a clear view of the harshness of the dispute. A precise and short review on the contact mechanics theories and models can be found in Morrow[**21**].

CHAPTER 5

Particle Impaction

"A child of five would understand this.
Send someone to fetch a child of five..."
- Groucho Marx

5.1. Hard & Soft Sphere Models

Usually, impact of solids may simply be sorted into two main categories, according to the type of contact. These are:

(1) hard contact: the contact time is negligible, compared to the reference time scale of the solid dynamics, and interaction may be represented with a Dirac function. The contact is said to be instantaneous.

(2) soft contact: the contact time is not negligible and the forces acting on the contact areas are time integrated according either to the Discrete Element Model[**78**] or the Viscoelastic model[**3, 13**] mimicking the contact.

In the hard sphere approach, a particle get into contact with another solid body according to a quasi-instantaneous collision. Forces are modelled as impulses. Indeed such an assumption prevents the model from being valid for multiple collisions, where during one collision another may occur due to the elastic response of the previous collision. The error in modelling multiple instantaneous collision with a series of single collision may be only reduced by integrating forces with a very small time step. In the soft particle approach, collisions are integrated along the contact time. Hence load (compression) and unload (anelastic relaxation) are modelled according to the selected spring-dashpot

combination, as the models presented in Chapter 3 in Fig.3.3.1. Unlike the hard one, the soft approach allows for multiple collisions to occur and for finite contact forces, a fact that makes the soft model of specific use in granular dynamics modelling.

The adhesion theories introduced above have been developed assuming isothermal and constant loading conditions (quasi-steady states) which makes them eventually time independent theories. Indeed such a result implicitly suits them as perfect candidates to model impact when the hard sphere approach is used. Nevertheless, these adhesion theories can be well integrated into a soft approach only if collisions are grouped into load, unload and re-load contributions, or a series of compressions and relaxations.

It is to be noticed that for the hard sphere approach, the relaxation modulus formulation is required, whereas for the soft approach, the compliance modulus needs to be calculated. The latter describes energy losses in terms of the work of adhesion, friction and deformation during the contact period, which indeed requires the calculation of the deformation $\varepsilon = J\sigma$. In general, for the soft approach the smaller the integration time step and the more accurate the information about viscoelastic parameters, the better the prediction. For instance, as reported by Hoomans[**60**], for the Voigt model the normal and tangential viscoelastic contact forces are

$$\begin{cases} F_{\perp} = -k_{\perp}\varepsilon_{\perp} - \eta_{\perp}v_{\perp} \\ F_{\parallel} = -k_{\parallel}\varepsilon_{\parallel} - \eta_{\parallel}v_{\parallel} \end{cases} \tag{5.1.1}$$

where k, ε, η and v are respectively the elastic restitution, the displacement or solid indentation due to the impact, the viscosity and the velocity along the normal$\perp$ and tangential $\parallel$ directions.

In the case of hard models, energy losses are taken into account by the relaxation modulus Y. Simplified models, like the approach proposed by Thornton [**54, 55**], require the calculation of the residual energy after the anelastic impact, plastic deformation by quasi-steady state analysis and finally the work of adhesion, which implies the use of the formulation $\sigma = Y\varepsilon$.

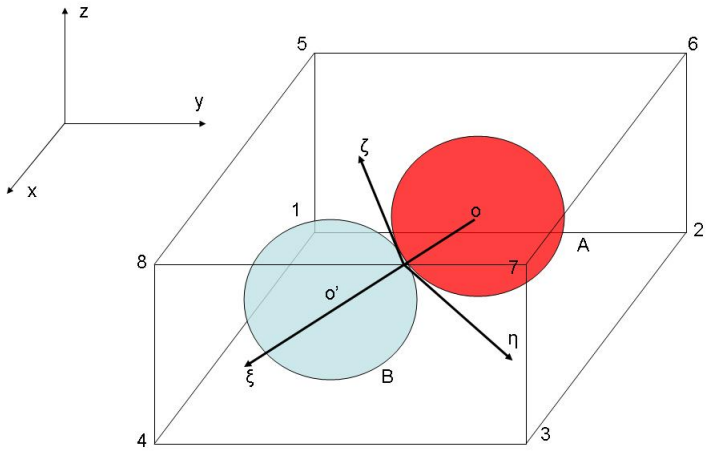

FIGURE 5.1.1. Particle collision in the local reference system. The mesh (only one hexahedron with 8 nodes is shown in this picture) is defined in a Cartesian reference system (global).

As shown in Fig.5.1.1, the impact local reference system is centered at the contact location. The vector $\vec{\xi}$ is defined as the centroids direction, $\vec{\eta}$ is the direction normal to $\vec{\xi}$ oriented towards the cell vertex V_2 whereas $\vec{\zeta}$ is defined as the direction $\vec{\xi} \times \vec{\eta}$ oriented towards cell vertex V_5. In case of a tetrahedral cell (four nodes only), V_5 is then obviously replaced by V_4. The orientation strategy follows the one described in Section 1.4 for the particle in-cell detection. Particle rotation was not accounted for because it was considered not relevant for most of the investigated cases presented here.

$$\begin{cases} \vec{\xi} = \frac{r_B - r_A}{|r_B - r_A|} = \frac{o' - o}{|o' - o|} \\ \\ \vec{\eta} = \perp \vec{\xi};\ \| V_2 \\ \\ \vec{\zeta} = \vec{\xi} \times \vec{\eta};\ \| V_5 \end{cases} \tag{5.1.2}$$

5.2. Energy Restitution Coefficients

Whether a particle rebounds or sticks to the wall depends mainly on two factors: particle properties (temperature, composition, angle of impact and kinetic energy), and impacted surface properties such as surface roughness, temperature and composition of the existing deposit layer [**49, 50**]. In order to evaluate the sticking *"propensity"* of a particle, the viscosity of the impacting particle is the key parameter [**9**]: the viscosity can be considered as an index (propensity) of the adhesion efficiency of the particle hitting on the surface. The sticking probability of impacting particles is usually evaluated as a function of its particle viscosity only, whereas in fact, a more rigorous approach would combine factors such as the temperature, the particle-wall viscous-elastic properties, the angle of impact, the kinetic energy, as well as the surface roughness and stickiness [**8, 9, 12, 25**]. Because of the statistical approach used here, a probability function to describe the particle-wall interaction is required. Such a function depends on the evaluation of both particle and wall viscosity: adhesion and hence deposition depends essentially on the particle and deposit properties. A more detailed, rigorous and different approach would calculate the energy restitution coefficient as a function of the viscoelastic properties of the particle. This model requires the calculation of the work of adhesion of solid particles [**4, 51, 52**]. Amongst others, Takahashi et al. [**53**] have applied visco-elastic theories to model different glasses at temperatures close to their specific glass transition temperatures, where the Young modulus dramatically decays. As far as the author knows, this approach was never applied before to the ash deposition problems. Vargas et al. [**24**] reviewed rheological studies on melts of coal and ashes and Newtonian and non-Newtonian liquids, focusing on the chemical properties of the deposit, without investigating the impact process leading eventually to the deposit. Deposition and adhesion of solid particles are a matter of mechanical impact analysis, as Johnson[**15**], Stronge [**3**] and Thornton [**54, 55**] have suggested and reported. For temperature dependent properties, as in combustion

cases, impact, adhesion and hence the deposition process can be investigated by applying the theory for viscous-elastic solids, better known as rheological solids [**13, 23**]. A simplified approach can be adopted by means of the calculation of the critical velocity [**54, 55**]. As suggested by Chau [**56**], knowledge of elastic contact can be *"borrowed"* to study viscoelastic contacts since plastic behavior and surface roughness can be modelled as anelastic impact occurring at higher energy dissipation. Greenwood and Williamson[**14**] (GW theory[1]) first, and Johnson[**15**] (JKR theory) and Derjaguin [**16**] have proposed models to study mechanical adhesion of solid particles. Maugis merged the theories above into one, the so called unified theory of adhesion[**19, 20**]. The JKR theory predicts better soft elastic materials, that are the majority of the cases of interest for this work. Therefore, the author applied the JKR theory on the studies performed by Thornton [**54, 55**] and Lim and Stronge[**57**].

It must be reported that, independently from the present work, Strandström et al.[**22**] have presented in 2007 a similar but simpler approach, evaluating the work of adhesion using the Young-Dupré equation, see eq. 4.0.9, only (no JKR or DMT theory) and including in the energy balance only the kinetic energy of the particle. Since surface energy data are extremely difficult to obtain and scarcely present in the literature and, moreover, not reported in their article, it is not really clear how they could have possibly calculated the work of adhesion. Applying the JKR or DMT theory, for instance, is like introducing a further degree of freedom in the system of equation which returns the restitution coefficients; since the energy balance is written by evaluating the (estimated) contact area as well as a (more) correct value for the energy dissipated during the impact. Such calculations reduce, instead of amplify, the (inevitable) errors the values for surface energies. Using the Young-Dupré eq. 4.0.9 is not sufficient to correctly predict solid particle adhesion, especially if particle inertia, hence mechanical

[1]The GW theory made the following assumptions: i) all asperities in contact were spherical with the same radius of curvature, ii) asperity heights follow a Gaussian distribution, and iii) there is no interaction between contacting asperities.

impaction, is the main driving force. For this reasons, the results of ash and sand mixtures deposition in a top-down gravity reactor (particles accelerating under gravity) presented by Strandström et al.[**22**] failed to correctly predict experiments for those particles larger than 75 μm (larger kinetic energy).

However, according to Malkin [**23**] and Lakes [**13**], if the material is thermorheological simple, particle elastic properties behave in the same manner with either time or temperature. On the other hand, Chau [**56**] stated that material thermorheological simplicity and linear visco-elastic behavior represent the exception rather than the standard for visco-elastic solids. For glasses the assumptions above are considered valid and hence they are applied in this work, and numerical results on glassy particle deposition are presented in the next section. In this dissertation, a time- and temperature- dependent formulation for the energy restitution coefficients is also proposed, in which the Young modulus is calculated by applying visco-elastic models as a combination of springs and dashpots: that is, in the present work, both the Maxwell model (see eq. 5.2.1) and the Standard Linear Solid (SLS) model (eq.5.2.2) were used to model glass particle behavior at temperatures respectively above and below the glass transition temperature (see Fig.3.3.1). The viscosity formulation is as in Urbain[**58**] while the interpolation functions for the viscosity parameters are calculated according to Senior and Srinivasachar [**11**]. According to this formulation, the Young modulus for Maxwell and the Standard Linear Solid (SLS) model may be written as follows

$$Y_p = Y \times \exp^{-\frac{t}{\eta_p / Y_p}} \tag{5.2.1}$$

$$Y_p = Y_1 + Y_2 \times \exp^{-\frac{t}{\eta_p / Y_p}} \tag{5.2.2}$$

where t, η_p, Y_p and Y_w are, respectively, time, viscosity and the Young modulus of the particle and the impacted wall; $Y_1$and Y_2 are the spring constant required by the visco-elastic SLS model, as in Fig.3.3.1. This

information is required in JKR theory to calculate the relative indentation of the two bodies during the load-unload process at the impact and the work of adhesion, which depends upon the surface energy Γ and the equivalent Young modulus Y^*.

$$\frac{1}{Y^*} = \frac{1-\nu_p}{Y_p} + \frac{1-\nu_w}{Y_w} \tag{5.2.3}$$

Concerning the mathematical modeling of elasto-plastic collisions with adhesion, the particle kinetic energy at impact, $E_{kin}|_i$, and $E_{kin}|_r$ at rebound satisfy the relationship

$$E_{kin}|_i = E_{kin}|_r + E_p + E_w + E_{ad} \tag{5.2.4}$$

where E_p is the work of plastic deformation, E_w is the energy loss due to wave propagation (typically $1-2\%$ of $E_{kin}|_i$) and E_{ad} is the work of adhesion, which is calculated using the Young-Dupré equation, see eq. 4.0.9, for two solids (1 and 2 subscript) at contact $W_{ad} = \gamma_1 + \gamma_2 - \gamma_{12} \cdot \cos\vartheta$ as described in [**52**], where ϑ is the angle of adhesion of the interface between the two bodies. At either equilibrium condition or for elastic materials (low mutual compliance), $\vartheta \approx \frac{\pi}{2}$. Stronge proposed to decouple normal and tangential stress contributions and corresponding forces by solving them independently [**3**]. In the JKR theory, the work of adhesion is defined as the energy required either to lift or to remove the particle along the normal direction. On the contrary, Batyrev et al. [**59**] distinguished the work of adhesion from the work of separation, which they found to be in some cases substantially different (and higher). In the present work, the JKR theory is assumed valid, with no distinction between work of adhesion and separation. Hence, the normal and tangential energy restitution coefficients are (see eqq. 5.2.5-5.2.6):

$$e_n = \sqrt{\frac{\frac{1}{2}m_p v_n^2\big|_r}{\frac{1}{2}m_p v_n^2\big|_i}} = e_p \times e_w \times e_{ad} \tag{5.2.5}$$

where e_p is the elasto-plastic energy restitution coefficient after compression and relaxation, $e_w \simeq 0.98$ is the wave dissipation restitution coefficient and e_{ad} is the adhesion restitution coefficient. In other words, if $E_{kin}|_i - E_p - E_w - E_{ad} > 0$ then e_n is calculated as in eq. 5.2.5, otherwise $e_n = 0$. The tangential energy restitution coefficient is

$$e_{tg} = \sqrt{\frac{\left(\frac{1}{2} m_p v_{tg}^2\big|_i - E_{fr}\right)}{\frac{1}{2} m_p v_{tg}^2\big|_i}} \tag{5.2.6}$$

where E_{fr} represents the energy loss due to the sliding and rolling friction. The variable Γ or the single components γ_1, γ_2 and γ_{12} should be derived experimentally for each couple of materials and their dependence on temperature may not have a simple form. For some materials they can be assumed constant with temperature. For glass particles impacting on steel $\Gamma = 25 \cdot 10^{-3} \quad \frac{N}{m}$. In the hard particle approach (used by Hoomans et al. [**60**] amongst others), particles are considered deposited when they simply stop along the surface as a result of inelastic collisions, namely, the work of adhesion is not considered. In a more appropriate approach, the evaluation of the deposition should take into account the time required to either stick or bind itself to the surface or to other particles, increasing the strength of the adhesion as well as the work of separation. The adhesion time may be considered as a sort of chemical relaxation time that particles require to form a bond to the surface and hence adhere. If a thermodynamic approach of adhesion applies, a particle might be removed from its location and put back into motion if hit by another particle before the bounding is completed, see Section 2.2. To save computational time when many particles are tracked, in this dissertation is proposed a limit velocity criteria, which is presented in subsection 7.4.1 in the following chapter 6. If particle-particle interaction is enabled, a particle can be removed from its location only if not already included in the deposit layer. In short, if the RTDE algorithm is used, every time the deposit is updated the particles deposited are considered sticked and not removable anymore.

CHAPTER 6

Adhesion Criteria

"Those are my principles, and if you don't like them...
well, I have others."
- Groucho Marx

6.1. Introduction

In this chapter the criteria to assume whether a particle is sticking (able to adhere) are briefly reported. Differences in the criteria are strictly motivated by the typology of the impact, i.e. high/low temperature, wet or dry adhesion. The approach proposed in this work is much more general than that of contact mechanics where a particle sticks if the condition $\left|F_{\parallel}\right| < \tau_{fr} \left|F_{\perp}\right|$ is fulfilled, where τ_{fr} is the friction coefficient. As a matter of fact, Lagrangian particle tracking is severely affected by high CPU time, which increases proportional to the number of the particles tracked. To reduce the computational load, it is critical to minimize the number of the "moving" particles, by sticking or stopping those particles fulfilling the sticking criterion selected . In literature several criteria are used. depending on the materials involved. They may be grouped as following:

(1) Contact time-independent (equilibrium)
  (a) Energy balance
    (i) viscosity
    (ii) particle molten fraction
    (iii) limit velocity (normal critical velocity or arbitrary value)

(iv) negative energy balance or Gibbs free energy calculation

(b) Force equation

(2) Contact time-dependent

(a) Force equation

The approach 2a requires either the *"a priori"* knowledge or the calculation of the contact time. The criteria 1a based on the energy may be simplified by assuming only a single variable, such as viscosity, temperature, velocity or Young modulus, representative of the energy status at the equilibrium of the particle at the impact, hence neglecting the contact time.

6.2. Contact time independent

6.2.1. Viscosity Criterion.

Concerning the mechanical properties of a solid, one may look either at the viscosity, the melting temperature (molten solid fraction) or the Young modulus. Such approach is still widely used in solid fuel combustion studies, since it based on the viscosity or temperature-composition formulae obtained by experimental data interpolation. Urbain [**58**] pioneered this approach providing a set of coefficients for ashes from solid fuel combustion. Such a formulation comes pretty handy when implemented in numerical codes. To this purpose, Senior and Srinivasachar [**11**] increased the accuracy of the method providing a set of coefficients based on the interpolation of a wide number of ash components. As reported in literature, the critical range of viscosity is $10^4 - 10^8\ Pa \cdot s$, for an ash particle on a clean surface tube. However, in coal combustion boilers viscosity was found to be most likely lying in the range of $10^5 - 10^7\ Pa \cdot s$ [**11, 9**]. More details about the Senior and Srinivasachar model are given in the Appendix B.2. As reported in [**8**], this approach does not consider the second body viscosity, which indeed plays the same role in the particle sticking assessment. Pyykönen and Jokiniemi

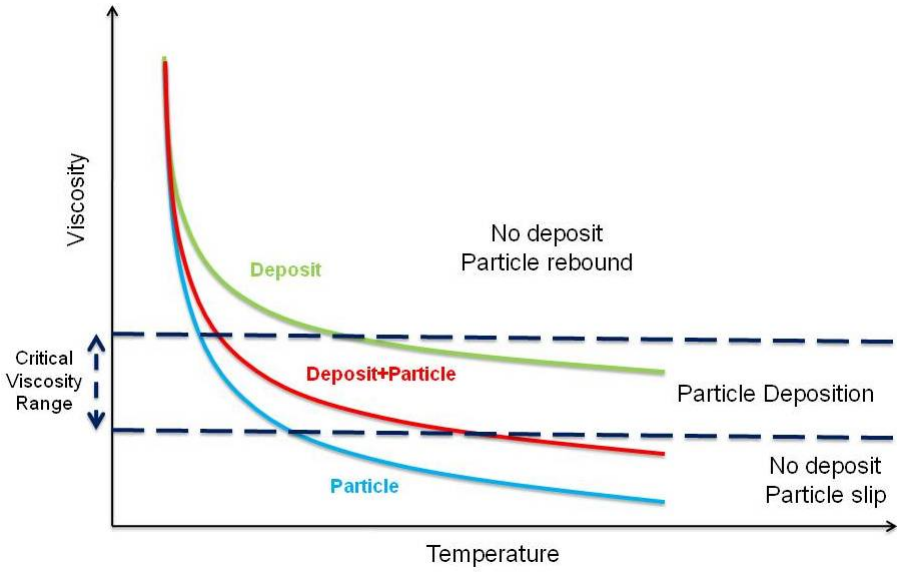

FIGURE 6.2.1. Particle and deposit qualitative viscosity behavior

[**71**] included the wall viscosity in the assessment of whether a particle may stick on it or not.Mueller and al. proposed to estimate such a probability calculating the particle molten fraction [**72**]. Although both colliding solids are considered in the viscosity evaluation, a particle is still considered stuck according to the critical viscosity range above mentioned or if the particle solid molten fraction is in the range of $25 - 75\%$, which may either over or underestimate the prediction, see Fig. 6.2.1. As shown in Fig. 6.2.2, in the approach followed in this thesis, the collision of a particle on a deposit (not clean) surface is modelled using an equivalent ghost particle whose properties and local curvature mimic the original particle-deposit impaction. This approach extends the validity of the JKR model to visco-elastic impactions.

6.3. Contact time dependent

The viscous and elastic forces acting on the particle during contact are can be time integrated applying a viscoelastic model. For instance, see Hoomans [**60**], if the Voigt model is applied, the contact force in the normal and tangential directions are

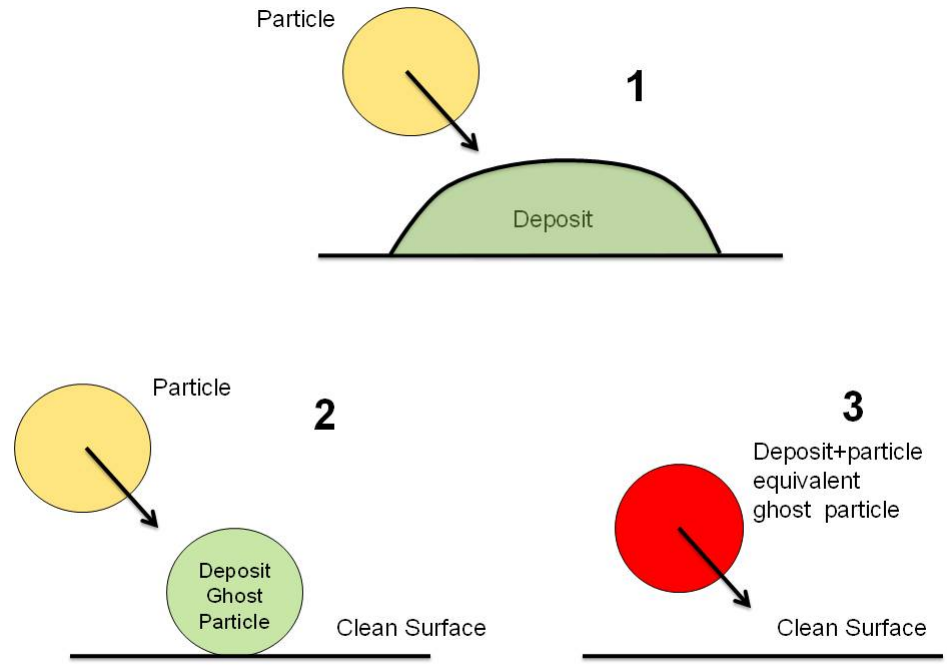

FIGURE 6.2.2. Ghost Particle-Deposit 3 step Algorithm

$$
\begin{aligned}
F_{\perp} &= -\kappa_{\perp}\xi_{\perp} - \mu_{\perp}v_{\perp} \\
F_{\parallel} &= -\kappa_{\parallel}\xi_{\parallel} - \mu_{\parallel}v_{\parallel} \\
F_{contact} &= \sum_{i}^{n} F_{i_{\perp}} + F_{i_{\parallel}}
\end{aligned}
\tag{6.3.1}
$$

where κ, ξ, μ, v are the elastic restitution coefficient, the solid compression displacement, the viscosity and the velocity in the normal and tangential direction respectively. n is the total number of the i forces acting during the contat period. The energy dissipated is then $E_d = \int_0^{t_c} F_c \cdot v dt$.

As reported in [**60**], only two type of collision may exists: sliding/bouncing and sticking. Therefore, particle adhesion criterion is evaluated on both the tangential and normal direction. If the tangential inertia component of a particle is sufficient to overcome the friction dissipation, such a particle slides and it may rebound only if its normal

velocity component is positive (same direction of the normal-to-surface direction). It is expected that such approach uses a limit velocity or kinetic energy criteria (cutt-off velocity/energy value) to reduce the computational cost. In the contact time-dependent approach the integration time step must obviously be smaller then the contact time. Therefore, such a model is computationally expensive. This model is commonly used in granular dynamics and in all those field where multiple collisions may occur in a chain reaction, with the overall energy loss depending on the number and the duration of each collision.

6.4. Conclusions

In this Chapter adhesion criteria were discussed. In the simulations presented in this dissertation in the following chapters, the velocity limit criterion was applied. This approach is indeed less strict compared to the critical viscosity range criterion. In the latter, particle adhesion is evaluated depending only on viscosity, which depends on temperature and composition. In CFD modelling, if a particle reaches the wall boundary surface having a viscosity in the critical range, such a particle will adhere no matter the impaction angle or the velocity (kinetic energy) at the impaction. Indeed this model has been revised and improved during the past decade. Several improvements have been made concerning a better identification of a critical range specific to the composition investigated and based on both deposit and impacting particle properties. However, this criterion has an upper and a lower limit which provide two degrees (values) of uncertainty. On the other hand, in the limit velocity approach only one limit (lowerest velocity for a particle before being considered stuck) is required and can be simply estimated by generic considerations on the fluid dynamics (main velocity of the flow) and particle relaxation time (or the Stokes number similarly). Furthermore, such a limit criterion is not necessary to assess the sticky capability of a particle since the viscoelastic modeling is applied. The limit velocity criterion presented here has the solely aim to speed up the particle tracking calculation, removing from the list of the *"alive"* particles those nearly stopped.

CHAPTER 7

Numerical Results

"It didn't matter how small your life was.

What happened to you was just as important as what happened to everyone else..."

- 'The Brooklyn Follies', Paul Auster.

7.1. Particle Deposition: Validation

Numerical results from the particle diffusion model and the deposition model have been compared to experimental results. Concerning particle diffusion modeling, a highly homogeneous turbulent case has been selected, namely, the experimental data collected by Snyder and Lumley[**26**] ($Re = 10^5$). They have been used for the validation, while for the deposition model experimental data obtained at ECN have been used. Results on dispersion are in agreement with those reported by Milojevic[**61**].

For non-homogeneous particles, it is necessary to estimate bulk values for all the thermo and mechanic variables in order to apply the viscoelastic modelling presented here. Depending on the model used, such as the Maxwell, the Voigt or other combinations of springs and dashpots, some assumptions have to be made to convert non-homogeneous solids into the equivalent solids having the same elastic and thermal response. For instance, the bulk density of hollow particles can be calculated from the mass balance

$$\frac{4}{3}\pi\rho_b r_1^3 = \frac{4}{3}\pi\rho_s \left(r_1^3 - r_2^3\right) \tag{7.1.1}$$

$\frac{r_2}{r_1}$	0.8	0.85	0.9
$\rho_b \left(\frac{kg}{m^3}\right)$	1220	964.68	677.5

TABLE 1. hollow glass bulk density and radius ratios

Density(bulk)	*Specific heat*	*Thermal Conduct.*	*Y(bulk)*	*T inlet*
1000 kg/m^3	840 $j/(kg \cdot K)$	1 $W/(m \cdot K)$	$70 \cdot 10^6$ Pa	300 K

TABLE 2. Glass particle data

$$r_1^3 \left(1 - \frac{\rho_b}{\rho_s}\right) = r_2^3 \Rightarrow \frac{\rho_b}{\rho_s} = 1 - \left(\frac{r_2}{r_1}\right)^3 \tag{7.1.2}$$

$r_1$and r_2 being the outer and inner radius of the particle and ρ_b the bulk, or equivalent, density of the hollow particle, and ρ_s the density of the solid material, which in the case of glass is 2500 kg/m^3.

Due to manufacturing limits and tolerances, the internal radius r_2 depends on the dimension selected for r_1, $r_2 = g(r_1)$. In the experiments, two particle sizes 75 μm and 105 μm were used. As reported in Table1, hollow glass mimicking high silicates ashes may have a density in the range $250 - 2000$ kg/m^3[**8**]. For simplicity, it is was assumed that $\rho_b = 1000$ kg/m^3. To take into account the non-linearity of the mechanical properties of glass at high temperatures (beyond the author's intent in this thesis), the bulk relaxation modulus was simply assumed to be 50 MPa, three orders of magnitudes lower than the $70 - 50$ GPa[1].

7.2. The Lab-scale Combustor Simulator (LCS)[2]

In recent years solid fuels such as coal, biomass and wastes started to be thoroughly investigated using small-scale test facilities. To this purpose, ECN has developed in the past few years the Lab-scale Combustion Simulator (LCS), a cylinder-shaped combustion facility which allows to investigate ash formation and deposition, corrosion and NO_x

[1]Young modulus reference value for commercial standard glass at room temperature.

[2]Information and pictures available at www.ecn.nl, [Weblink ECN LCS]

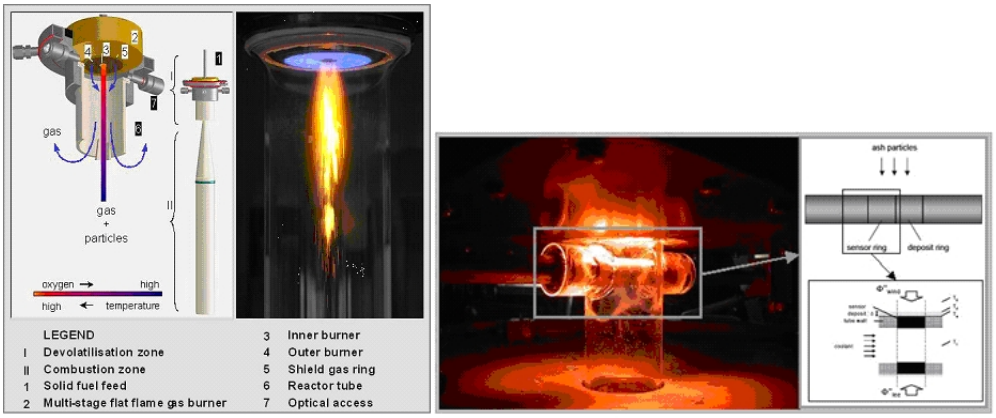

(a) LCS gas/solid fuel injector overview

(b) LCS deposition probe detail

FIGURE 7.2.1. The Lab-scale Combustor Simulator (LCS), fuel injection and deposition probe details. (www.ecn.nl) [Weblink ECN LCS]

performance of pulverized solid fuels at feeding rates in the range $1 - 10\ g/hour$. The final goal is to provide information and assess performance of fuels for coal fired power stations. In Fig.7.2.1 the LCS injection system is presented: this versatile rig combines high heating rates and temperatures with a realistic residence time and flue gas composition. Furnace slagging is studied by chemical and microscopic analysis of the ash samples collected by means of a vertically adjustable probe.

The efficiency and the accuracy of the deposition models presented in this dissertation are validated against the LCS glass particle deposition results. In the experiment performed with glass particles, the LCS configuration was slightly changed, from the cone shaped shown in Fig. 7.2.1a to the straight cylinder shown in Fig.7.4.1. Furthermore, the sampling probe is placed close to the outlet of the burner to collect part of the fouling material, and next to analyze the thermal resistance (fouling factor) of the deposit, see Fig.7.2.1b.

A full description of the LCS can be found in **[63, 64]**. The probe mimics a steam pipe of a typical super heater in the early part of the

Case	*Particle Diameter*	*Overall LCS Temperature*
Test 1 (Fluent T_1V_3)	105 μm	925 C
Test 2 (Fluent T_2V_1)	71 μm	965 C
Test 3 (Fluent T_4V_3)	105 μm	1090 C
Test 4 (Fluent T_4V_2)	105 μm	1015 C

TABLE 3. ECN Lab-Combustor Simulator (LCS). Values of particle diameter and furnace temperature in the tests.

convective section of a pulverized coal-fired furnace. This experimental facility works at a Reynolds number between $1 \cdot 10^{-3}$ and $5 \cdot 10^{3}$. The temperature of the gas approaching the probe is around 1200 C, whereas the surface of the probe which is facing the particle-laden gas flow is kept at 600 C by its air cooling system. Glass particles of different size have been used to mimic deposition occurring when the ash is rich in silicate components. In this work, numerical and experimental results on glass particles are compared to validate the deposition model, in particular, important variables are interface energies and Young Modulus as function of particle-surface viscosity, hence temperature and composition of both particles and deposit.

7.3. Steady Particle Tracking

To validate the particle adhesion model, RANS simulations combined with steady and unsteady particle tracking were carried out. In Table 3 the experimental facility settings are given, while in Table 4 steady particle tracking results on the deposited mass are listed. To validate the CFD computations of the gas phase, from the experiments the axial temperature profile and the mean axial velocity, calculated at the center (0.5 m from the top inlet) of the reactor, were given. Numerical results are compared with measurements for several cases with different mean velocities. Temperature profiles are presented in Fig.7.3.1. V_1 and V_2 are 3.1 m/s while V_3 is 6.2 m/s. Both Fluent and Cinar CFD codes were used. In Fig.7.3.3, the deposit of the test case 4 is shown.

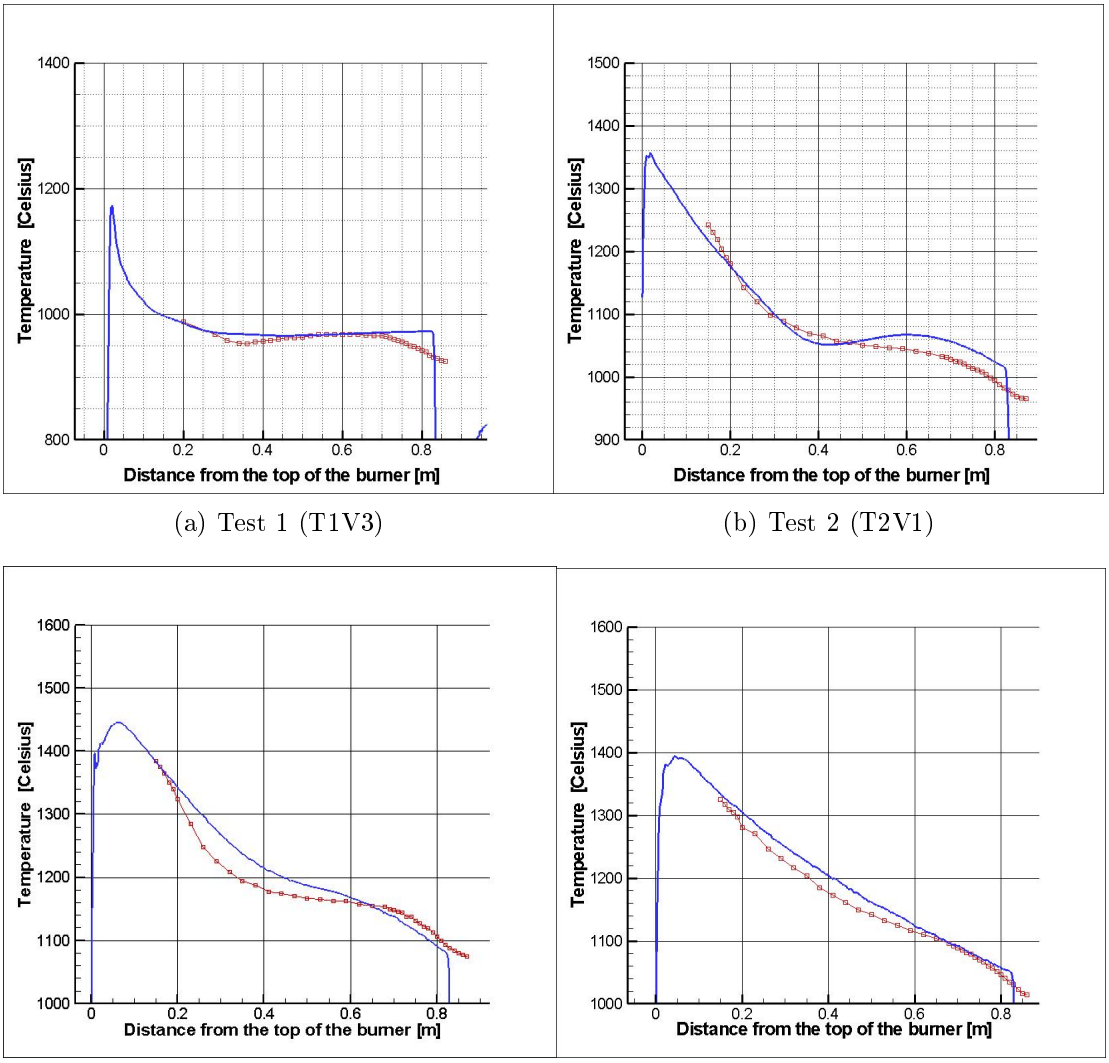

(a) Test 1 (T1V3)

(b) Test 2 (T2V1)

(c) Test 3 (T4V3)

(d) Test 4 (T4V2)

FIGURE 7.3.1. LCS center-line temperature profiles. Fluent, RANS $\kappa - \varepsilon$. $\boxminus$experiments, $-$ numerical data

In Fig. 7.3.4, 7.3.5, 7.3.6, 7.3.7, numerical results on deposit thickness are presented whereas in Table 5 results on the deposited mass are reported. Tracking 10^4 particles instead of 10^3 had the effect of widening the deposit area, not the amount of the deposit. The thickness of the deposit is certainly influenced by the CFD mesh resolution (see Fig.7.3.2 and 7.3.4). The fact that the amount of the deposit

Case	*Experimental Deposited Mass*	*Numerical Deposited Mass*
Test 1 (Fluent T_1V_3)	0.02 g	0.03988 g
Test 2 (Fluent T_2V_1)	0.08 g	0.31875 g
Test 3 (Fluent T_4V_3)	0.82 g	0.878 g
Test 4a (Fluent T_4V_2)	1.89 g	1.58 g
Test 4b (Cinar T_4V_2)	1.89 g	2.4173 g

TABLE 4. Experimental and numerically calculated deposited mass results. Numerical simulations details: 1000 Particles, RANS, Steady Particle Tracking, no RTDE.

Case 4	Deposited mass
1000 *Particles*	1.58 g
2000 *Particles*	1.53 g
5000 *Particles*	1.62 g
10000 *Particles*	1.54 g

TABLE 5. LCS Case 4, Fluent RANS $\kappa - \varepsilon$, steady particle tracking deposited mass vs. particle number

differs between the calculation performed with Fluent and Cinar can be explained by considering the consistently different mesh resolution: Cinar 15264 hexahedral cells, Fluent 218793 tetrahedral cells. Mesh resolution may influence both the fluid dynamics of the gas phase and the particle time integration.

7.4. Unsteady Particle Tracking

The case No. 4 was selected to validate the RTDE procedure with the reduction of the computational domain. Unsteady particle tracking was performed on the reduced (red color) domain shown in Fig.7.4.1.

Particle properties like temperature, Young modulus and in particular x, y and z velocities have been assigned as input data collected as statistics from the steady simulation of the complete domain. Such a strategy allows not only to account for the particle history but it may also increase the accuracy of the calculation tracking a larger number of particles. To save computational time it is possible to do the mesh

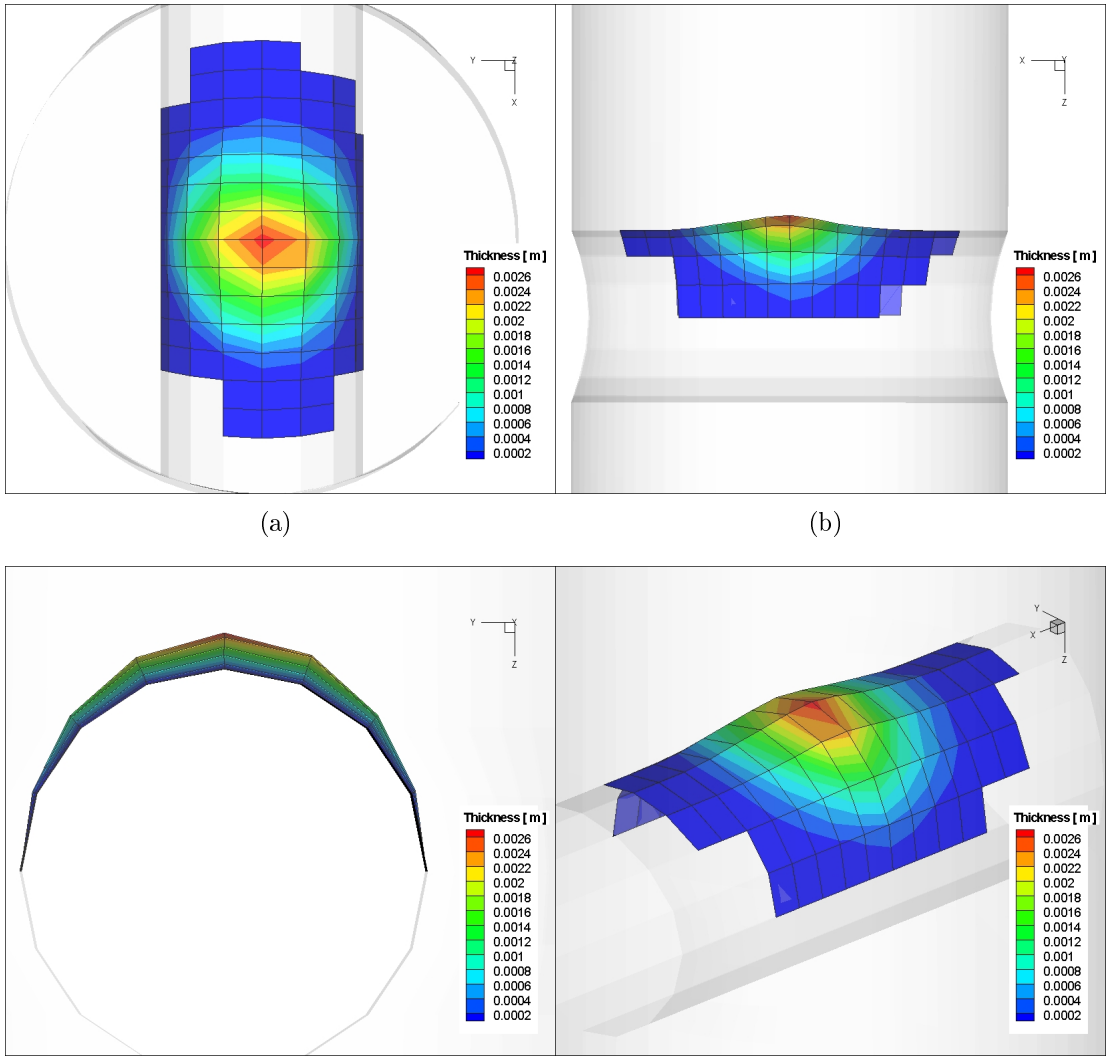

(a) (b)

(c) (d)

FIGURE 7.3.2. Steady particle tracking, 1000 particles deposit thickness results (Cinar, case 4)

updating not after every particle deposition but setting a minimum amount of particles to be deposited before starting the mesh updating procedure: In this case, the mesh update procedure starts only if the limiting number, set by the user as input parameter, is exceeded.

In Alg. 6 a brief overview of particle deposition and mesh update algorithm is presented. For full coupling, the *limit* parameter must be

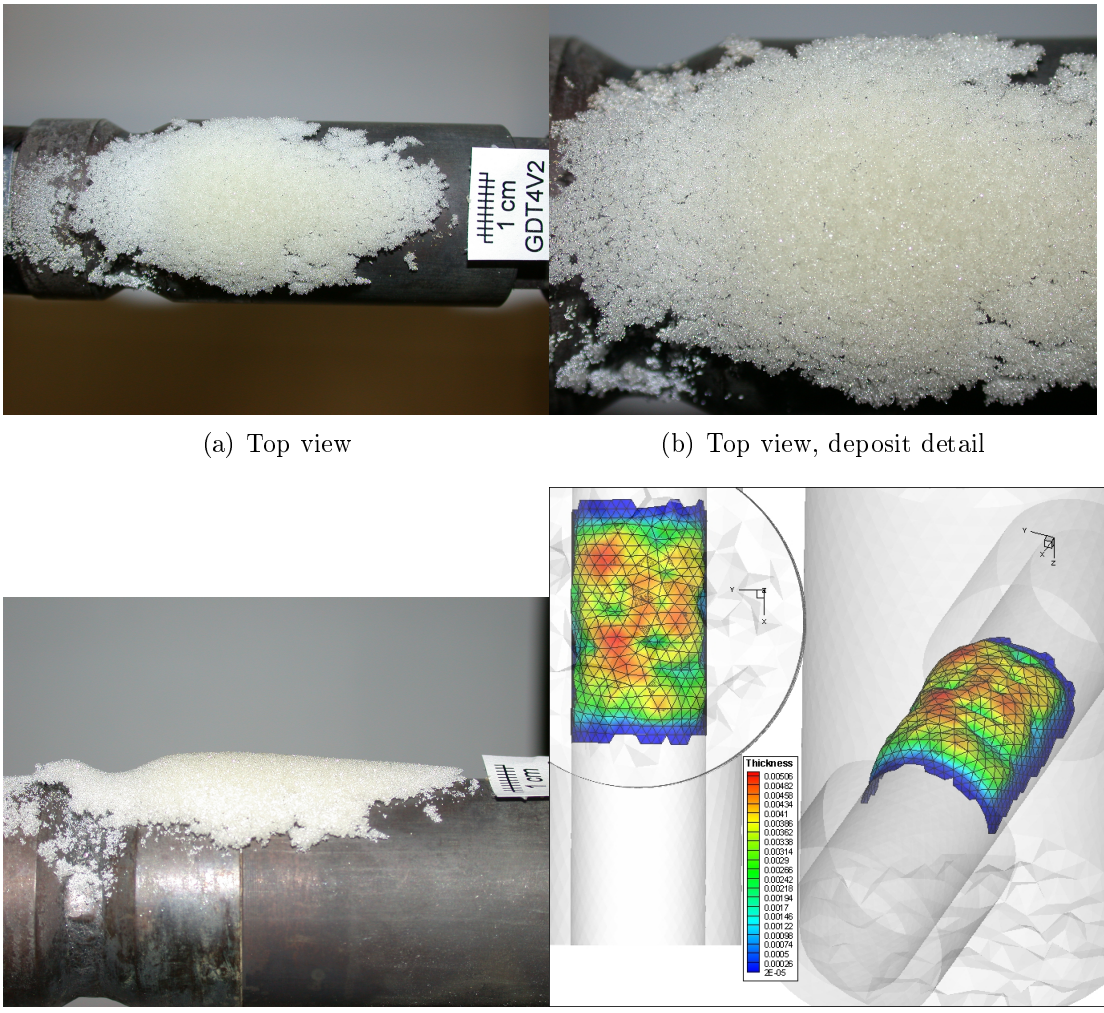

(a) Top view

(b) Top view, deposit detail

(c) Side view

(d) Num. Result: Unsteady particle tracking on the reduced volume

FIGURE 7.3.3. LCS Glass Experiment Case 4 (T_4V_2)

$limit \to 0$ while for a complete decoupling (no mesh update) $limit \to \infty$. It is to be noticed that results obtained in the latter case ($limit \to \infty$) would simply coincide with those collected as the steady particle tracking were applied (no deposit evaluation while computing particle tracking).

Numerical results concerning the use of the RTDE algorithm and the unsteady particle tracking are reported in the following pages in

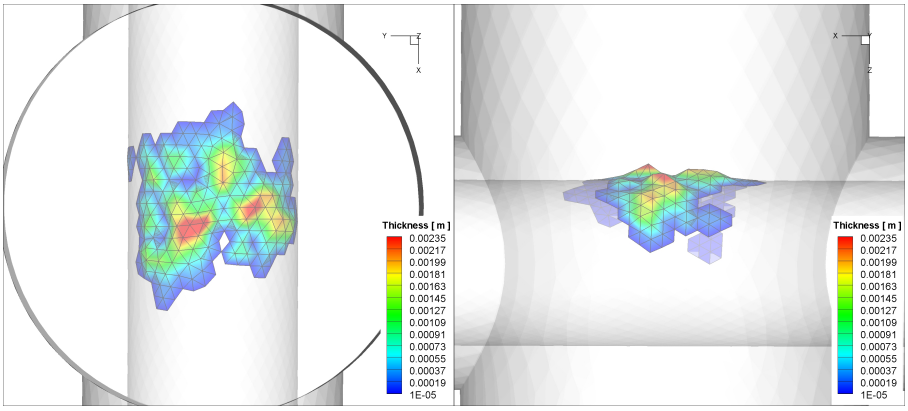

(a)

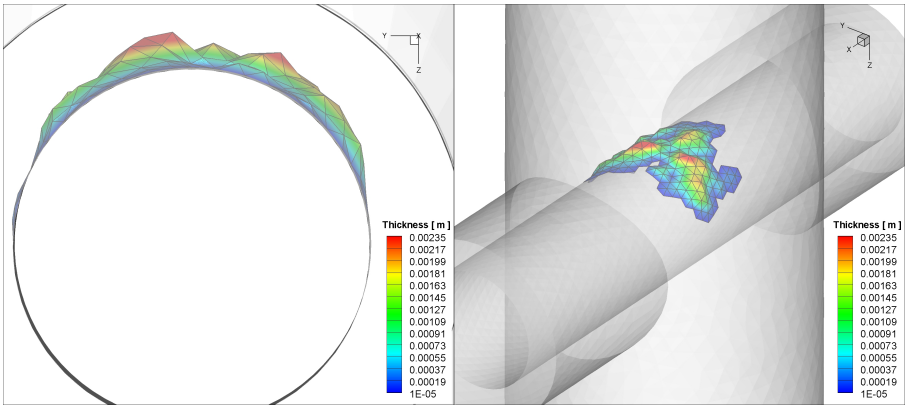

(b) (c)

FIGURE 7.3.4. Steady particle tracking, 1000 particles deposit thickness results (Fluent, case 4)

Table 6. The test case 4 was used to test the particle adhesion criteria. As mentioned in chapter 6, a particle is considered stuck when the residual energy is negative after the impact. The criteria used by Thornton[**54**] considers a particle stuck if the normal velocity is lower than the *"critical"* velocity V_s[3].

7.4.1. Particle Velocity Sticking Criteria.

[3]The critical velocity is considered the velocity below which the particle adheres to the surface. In literature it is usually referred as a normal velocity.

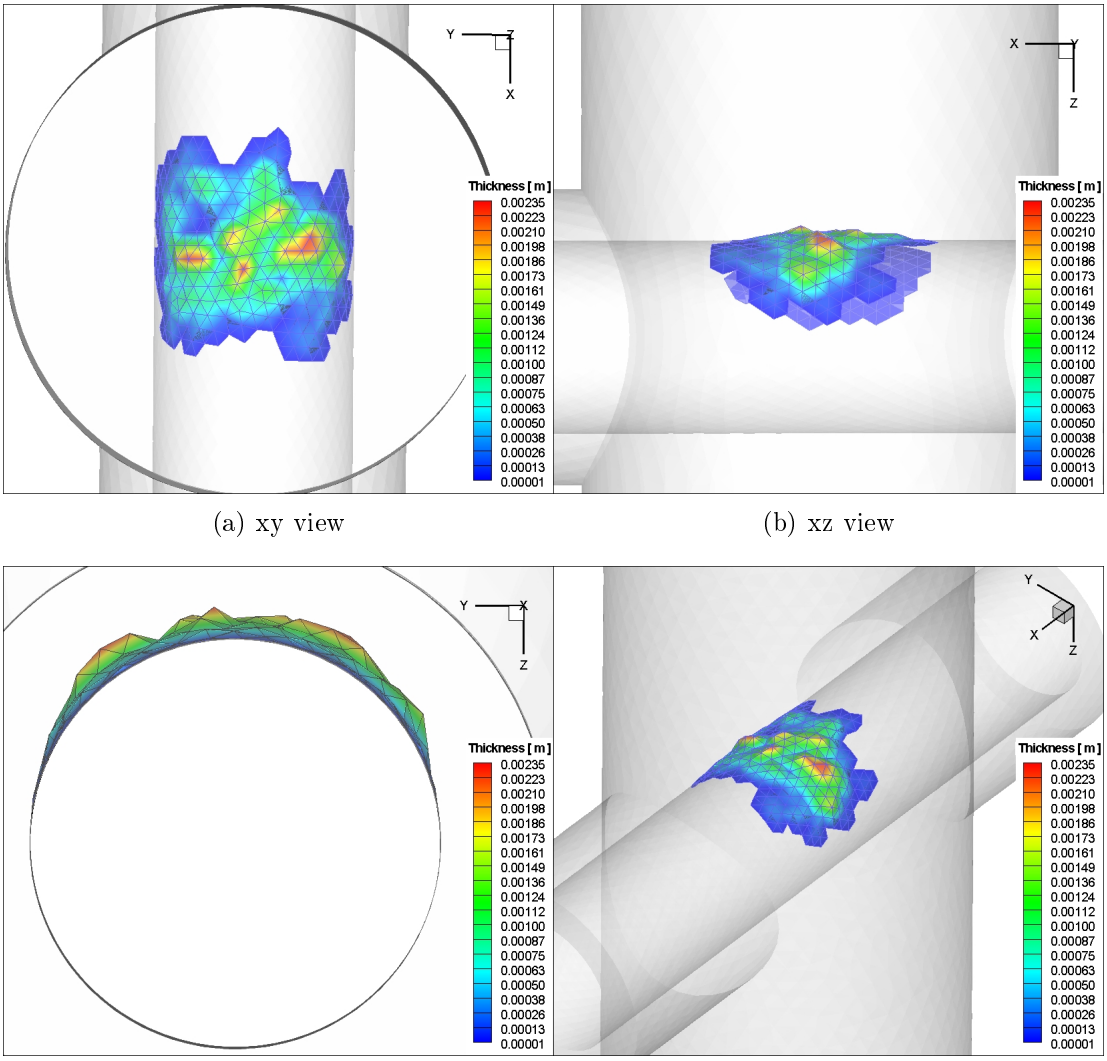

(a) xy view (b) xz view

(c) yz view (d) 3D view

FIGURE 7.3.5. Steady particle tracking, 2000 particles deposit thickness results (Fluent, case 4)

When tracking many particles, in order to save computational time particles may be considered stuck (i.e. stopped) if conditions set on the velocity are fulfilled. These conditions are usually set either on the module $\left|\vec{V}\right|$ or on the normal $V_\perp$ component[4] as in **[54, 55]**. That is, the adhesion conditions are $V_\perp \leq V_{lim}$ or $\left|\vec{V}\right| \leq \overline{V}_{lim}$. To V_{lim}

[4] $V_\perp$ can be considered as the escape or bouncing off velocity.

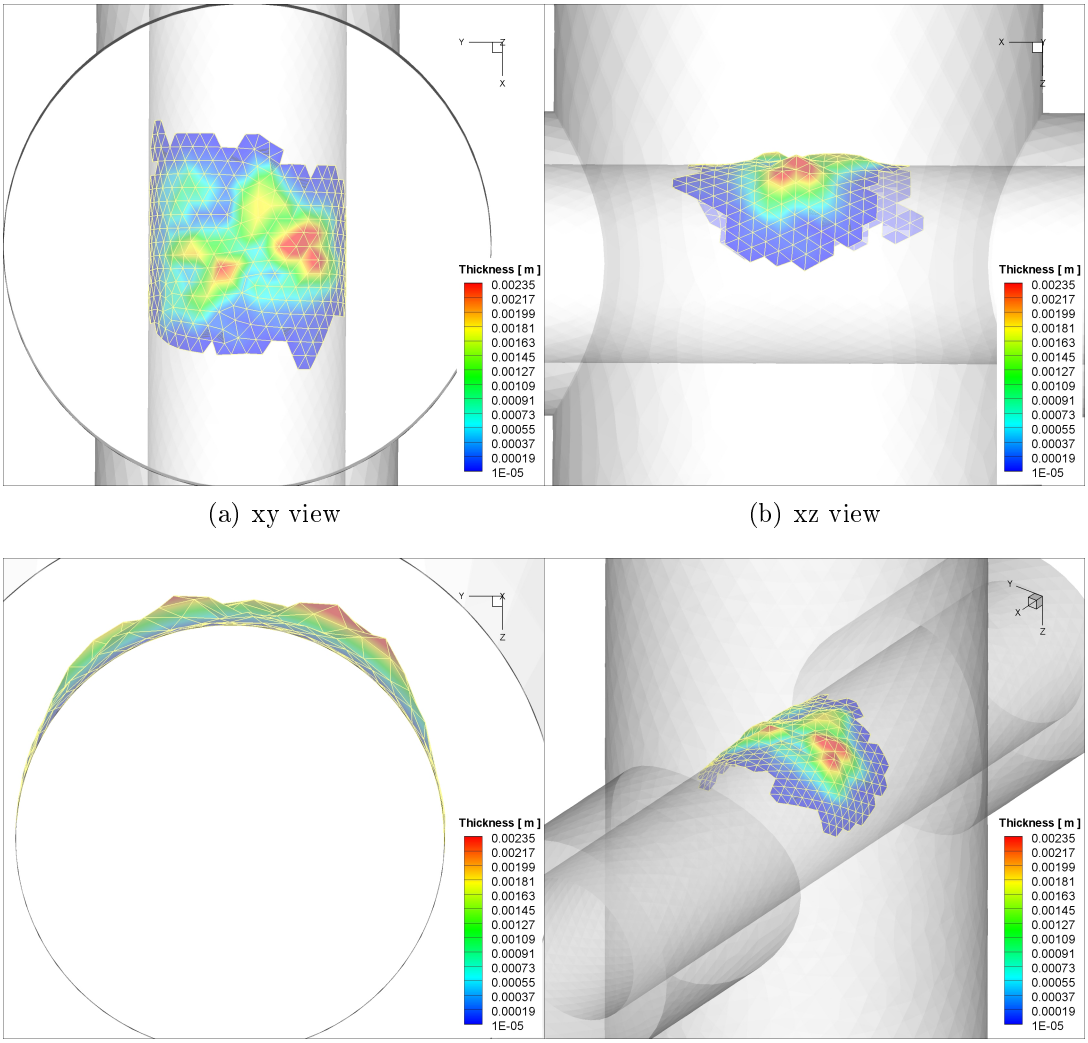

(a) xy view (b) xz view

(c) yz view (d) 3D view

FIGURE 7.3.6. Steady particle tracking, 5000 particles deposit thickness results (Fluent, case 4)

either a reference value $\overline{V}_r$ can be assigned[5] or the critical velocity V_s. Since the calculation of the critical velocity V_s is based on the mechanical analysis of the kinetic and the stored elastic energy (see

[5]lower than the critical velocity, $\overline{V}_r \leq V_s$

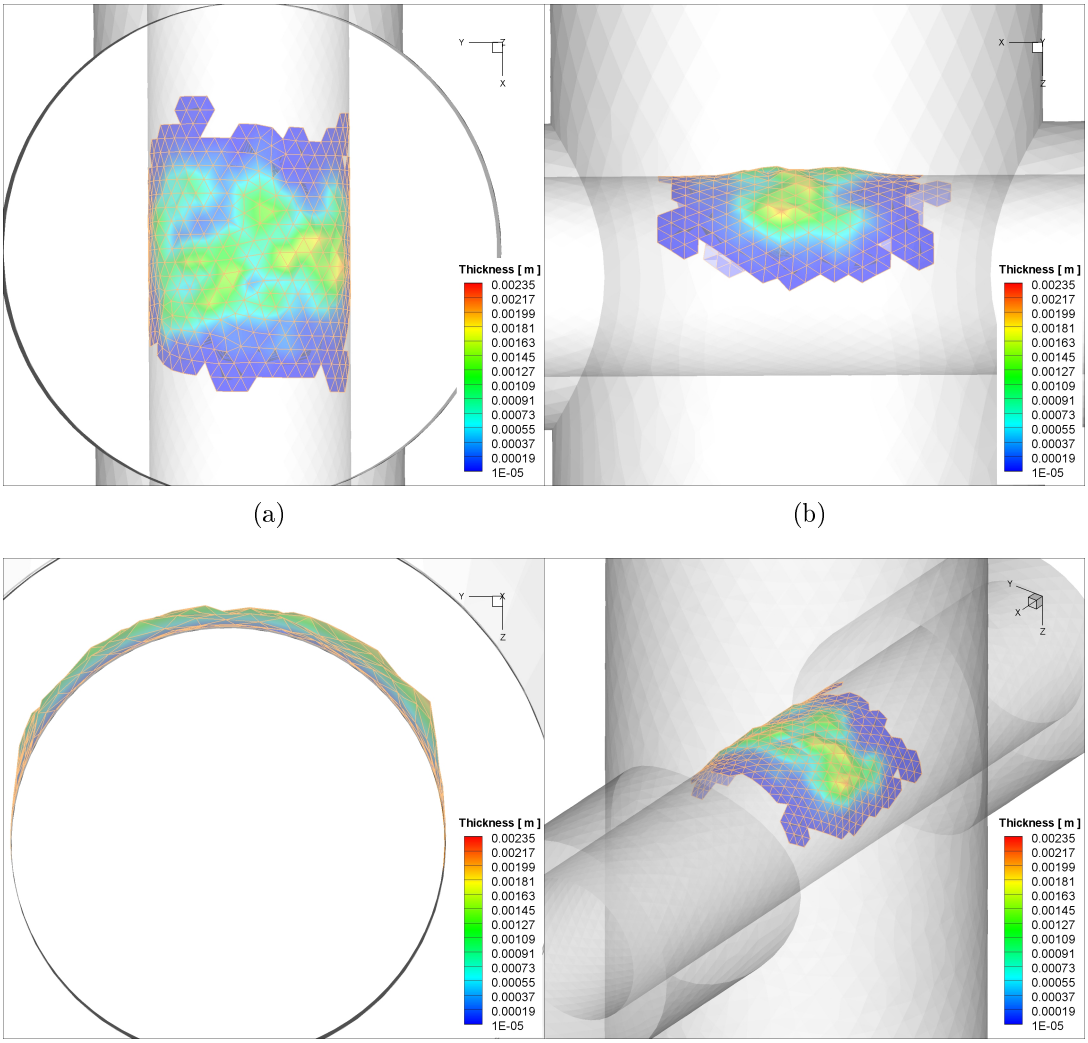

FIGURE 7.3.7. Steady particle tracking, 10000 particles deposit thickness results (Fluent, case No. 4)

section 1a), it represents the highest velocity limit[6]. Although there are several different possibilities to combine the limit velocities, only two combinations are really relevant.

[6]As in[**54**], the critical velocity is calculated for normal elastic impacts. Such a formulation can also be used for some non-normal impact cases with a few more assumptions[**55**].

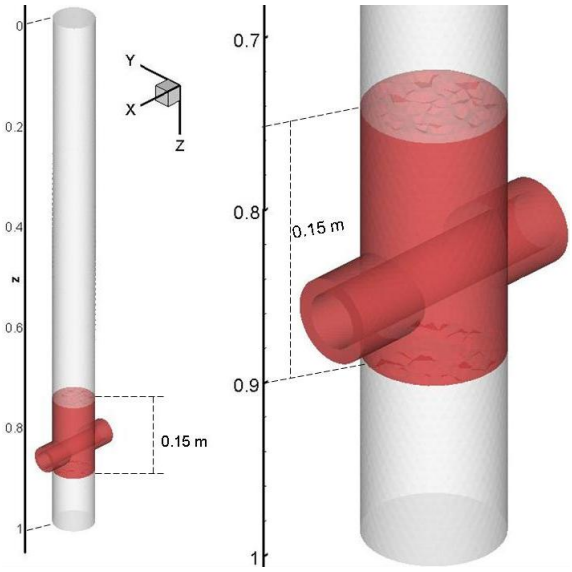

FIGURE 7.4.1. LCS Complete and Reduce Domain

Algorithm 6 Mesh Update

(1) limit number = *limit* (input parameter)
(2) counter_stop= 0
(3) Loop on all the moving particles
  (a) Particle-wall collision detected
  (b) Calculate particle-wall adhesion (restitution coefficients)
  (c) meet the criteria to consider the particle as stopped (not moving and considered not deposited yet)
  (d) if criteria are met, then
    (i) the particle is labeled as stopped $\Rightarrow$ counter_stop = counter_stop+1
  (e) end if
(4) end loop
(5) if $counter\_stop \geq limit$, then
  (a) update mesh (node position, thickness, composition and viscosity)
(6) end if

7.4.1.1. *Normal Velocity Criterion:* $V_\perp \leq \overline{V}_{lim}$ *and* $\overline{V}_{lim} = V_s$.

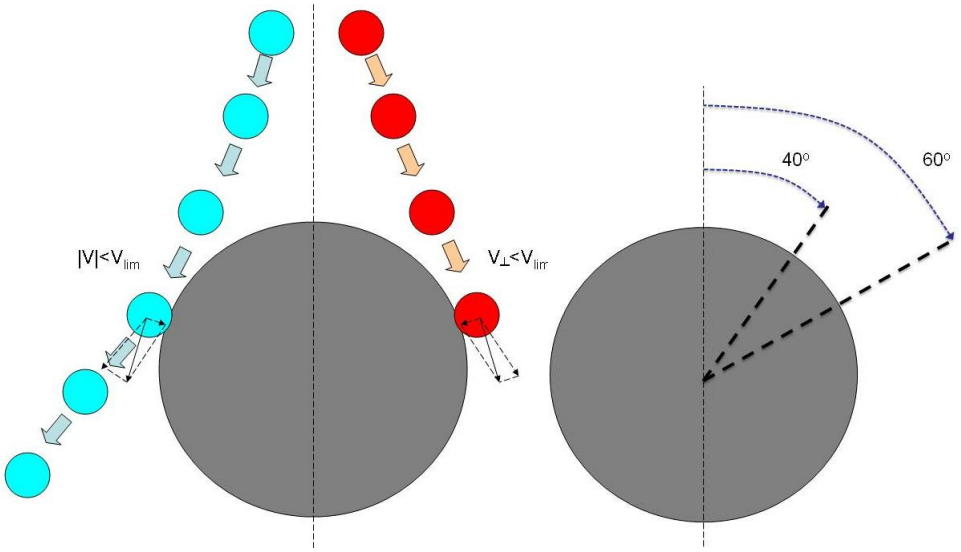

(a) Particle limit velocity condition sketch (b) Sketch of side deposition: normal velocity limit criterion

FIGURE 7.4.2. Sticking Velocity Conditions

For low impact angle collisions, this condition may provide significantly wrong adhesion predictions. It can be applied only if particle rotation and sliding are also calculated, and knowing, not assuming, the correct viscoelastic model for the specific case. Collisions on round surfaces, such as tubes or other particles, are a clear example. As shown in Fig. 7.4.2, if a particle impacts at a normal velocities smaller than the limiting one chosen, and if no particle rotation is taken into account, the particle may eventually adhere instead of bouncing off. Such a behavior leads to wrong deposit predictions of mass, thickness and certainly locations. The result of such a misprediction is shown in Fig. 7.4.3 and at [Weblink LCS Wrong Deposit]. Applying this criterion implies that particles adhere on the left and right sides of the tubes, providing an unrealistic deposit shape, which is not supported by the visual experimental inspection shown in Fig. 7.3.3.

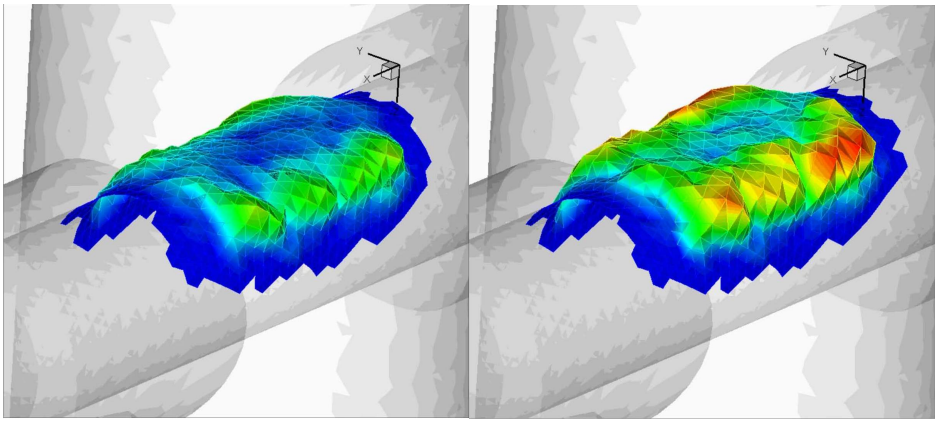

(a) (b)

FIGURE 7.4.3. Deposit prediction for the normal velocity criterion: velocity adhesion condition $V_{\perp} \leq \overline{V}_{lim}$ and $\overline{V}_{lim} = V_s$. Simulation: LCS test case 4 (Fluent).

7.4.1.2. *Velocity Magnitude Criteion:* $\left|\vec{V}\right| \leq \overline{V}_{lim}$ *and* $\overline{V}_{lim} = \overline{V}_r$.

This condition allows the particle to bounce off even at very small impact angles[7] as long as the limiting velocity is lower than the critical velocity, and it is calculated assuming the fluid-particle main relative velocity: in the LCS, the range of velocities is $1 - 10\ m/s$, hence $\overline{V}_r = 10^{-3}\ m/s$ was chosen as reference value. When tracking thousands of particles, the computational time may be considerably reduced assuming this condition on the velocity to consider a particle eventually sticked. Results obtained with this assumption are shown in Fig.7.4.4 can be compared with those in Fig.7.4.3; output animations are shown at [Weblink LCS Deposit] and [Weblink LCS Particle-Deposit].

7.5. Ash Deposit Validation

7.5.1. Description of the case.

[7] at non-negative energy balance at the impact

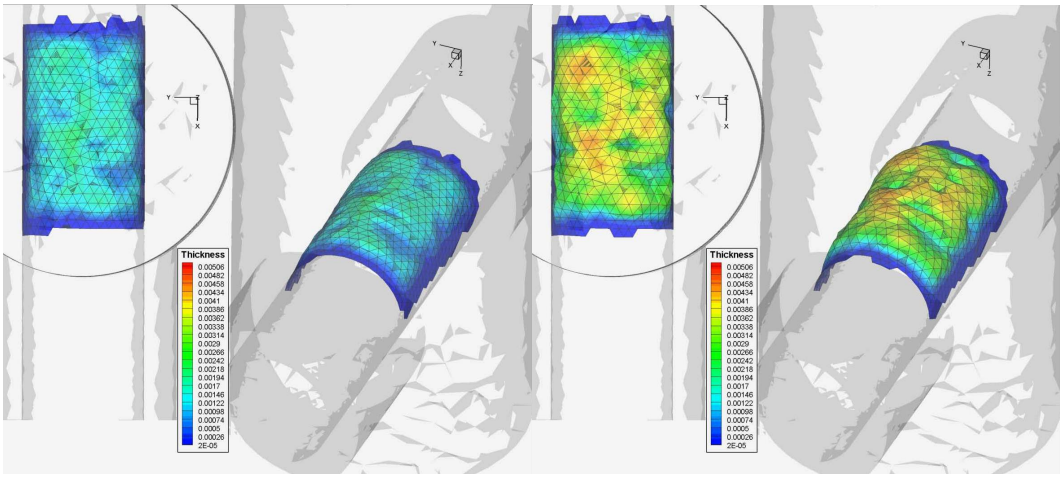

(a) (b)

FIGURE 7.4.4. Deposit prediction for the velocity magnitude criterion: velocity adhesion condition $\left|\vec{V}\right| \leq \overline{V}_{lim}$ and $\overline{V}_{lim} = \overline{V}_r$. Simulation: LCS case No.4 (Fluent).

Deposited Mass		Thickness	
Exp.	*Numerical*	*Exp.*	*Numerical*
1.89 $g\,(1\ hr)$	1.91 g	2.8 $mm\,(1\ hr)$	2.3278 $mm\,(1\ hr)$
			$\simeq 5\ mm\,(2.14\ hr)$

Time ($DEC = 5 \cdot 10^3$)			
Experimental Time	*Simulated Time*	$DEC \cdot Time_{Simul}$	*Deposition Rate*
1 hr	1.5465 s	$\simeq 2.14\ hr$	$5.3 \cdot 10^{-4}\ g/s$

TABLE 6. RTDE Glass Case: Test 4 (Fluent T_4V_2), 309200 particles tracked. The numerical deposited mass 1.91 g is calculated as *deposition rate* $\cdot$ 1 hr. The deposition rate is estimated on 1.5465 s, which linearly represents 2.14 hr by means of the DEC coefficient.

The model presented in this dissertation was validated against ash experimental data collected in the LCS facility. The deposited ash information are concerning the ash composition (input for the P^3) and the deposited mass only (validation result).

Deposited ash (in mg/kg ash d.b.)		Density
SiO_2	489409	2200 kg/m^3 $\pm 0.48\%$
Al_2O_3	250037.7	4000 kg/m^3 $\pm 0.25\%$
Fe_2O_3	85170.8	5240 kg/m^3 $\pm 0.085\%$
CaO	71534.6	
MgO	55945.6	
Na_2O	12124.0	
K_2O	28351.9	
P_2O_5	3071.4	
SO_3	2839.6	
Cl	38.2	
MnO	1443.5	
ZnO	29.3	
PbO	4.4	

TABLE 7. Ash Composition

Combustion coal: gas flow through the reactor tube= 4.56 Nl/min = 0.0000635 kg/s with $\rho = 0.8353575$ $kg/Nm3$.

Gas composition in mass fraction:

$N_2 = 0.74474$

$O_2 = 0.05521$

$CO_2 = 0.11110$

$H_2O = 0.08895$

Diameter inlet 20 mm positioned at $z = 140$ mm and centered to x,y.

Temperature inlet=1641.15 K, Temperature probe=863 K.

Feeding rate of fuel=3680 mg fed at $1g/h$

Ash content =18.92 $w\%db$

Deposited mass=290 mg

Deposit thickness=1.70 mm

Approximate size of ashes=36.36 μm

Estimated ash density: $2500 - 2600$ $kg/m3$

7.5.2. Numerical Results.

$No.Particles$	$Deposited\ Mass$	$Fragmentation\ inlet\ distance$	Cd
50	236.7270420019 mg		$0.25 \cdot Cd$
100	292.396608 mg		
500 $frag$	281.287424225 mg	0.6 m	$0.5 \cdot Cd$
1000 $frag$	287.2056002298 mg	0.4 m	$0.25 \cdot Cd$
5000	288.9206586477 mg		$0.25 \cdot Cd$
$experimental$	290 mg		

TABLE 8. Ash Deposition Numerical Results

Validation of the numerical model was demonstrated based on the deposited mass. In fact, the numerical results in Table 8 are in good agreement with the experiments (290 mg).

7.5.2.1. *Fragmentation Model.*

Implementing a particle fragmentation model was attempted in order to test the capability of the P^3 code. The criterion explicited into an $IF - THEN - ELSE$ loop, was based on particle position: the particle was assumed to fragment in two parts when beyond a limit axial location. This simple logical condition is meant to be replaced by a proper temperature-pressure gradient condition in a more advanced fragmentation model. Velocities along x, y and z directions were assigned according to each particle momenta, see Fig.7.5.1. A random number (from a Gaussian distribution) was used to mimic particle dispersion and energy loss that may occur in fragmentation. Although the excessive simplicity of this model did not significantly affect the results, the capability of the P^3 code to straightforward implement fragmentation was demonstrated.

7.6. Conclusions

In this chapter the validation of the numerical simulation of particle tracking and deposition model using a viscoelastic approach, with

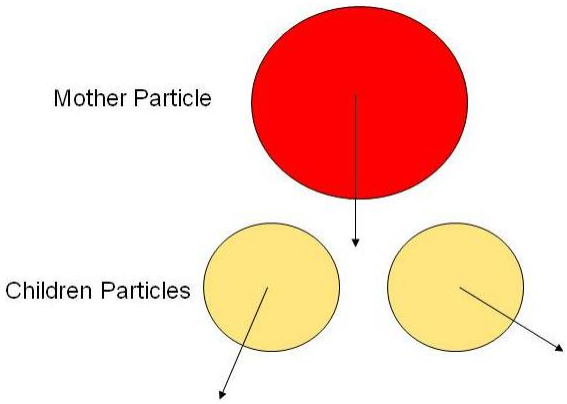

FIGURE 7.5.1. Sketch of the Particle Fragmentation Model

time-temperature material and mechanical properties dependency, has been presented. Numerical results otained for glass and ash particles show that the algorithms implemented may correctly predict location, area, amount and thickness of the deposit. Although some results are qualitative, they are significantly in good agreement with the experimental data. In any case, a qualitative estimate may help to optimize facilities and prevent fouling to occur. A short summary of the strategy applied is reported in Table 9.

In low ash deposition conditions, the joined steady-unsteady particle tracking strategy (including the complete and reduced computational domain) seems not to improve the numerical accuracy of the result, compared to the simple steady particle tracking. The same statement is also true in severely high deposit conditions, where particles would stick anyway at the first contact with (any) kind of surface, either clean tubes or already deposited particles. At the contrary, the use of the combined steady-unsteady computational strategy turns useful in those cases when either stratification may occur (long time duration operation and different composition in time) or neither the particles nor the deposit conditions lies in the sticking range which may differ according to the composition. In the latter case, it is important to evaluate the properties of both the deposit and the impacting particles. Applying the approach presented here, deposit properties are updated

CFD	P^3 $Strategy$	$Particle$ $Tracking$	VEM	$Particles$
$RANS$	$a)$ $Complete$ $Domain$ $b)$ $Reduced$	$a)$ $Steady$ $b)$ $Unsteady$	$Maxwell$ $Model$	1) $Glass$ $(a-b)$ 2) Ash (a)

TABLE 9. Numerical Validation Summary Table

with the boundary node displacement (mesh update algorithms, Alg. 3-4 in Section 7.4).

Part 3

Industrial Cases

CHAPTER 8

Bundle of Tubes

"When one admits that nothing is certain one must,
I think, also admit that some things are much more nearly certain than others."
- Bertrand Russell

8.1. Introduction

In this chapter particle deposition on a bundle of tubes is presented. The aim is to show, test and provide a better insight of the deposition occurring in unsteady flow fields. To perform such a numerical test, several hundreds of thousands particle being continuously tracked, the facility illustrated in the work of Abd-Elhady et al.[**42**] was employed, as it has a threefold advantage: i) simple shaft geometry, ii) isothermal deposition of simple Calcium Carbonate $CaCO_3$, iii) use of the critical velocity introduced by Thornton[**54**] on the basis of the JKR theory to asses whether particles deposit or not. A drawing taken from[**42**] of the facility is shown in Fig.8.1.1.

In [**42**], four cases were investigated: vertical downstream, vertical upstream and vertical 45 *deg.* upstream and horizontal flow. Since in the horizontal case deposition may occur alongside the shaft walls, it appeared not a suitable benchmark for the numerical strategy presented in this dissertation. Sketches of the three experiments chosen to be simulated are shown in Fig.8.1.2. As reported in [**42**], an air blower was used to introduce the particles. Nine 3.2 cm diameter tubes were placed in the 3x3 configuration (as shown in Fig.8.1.1). The $CaCO_3$

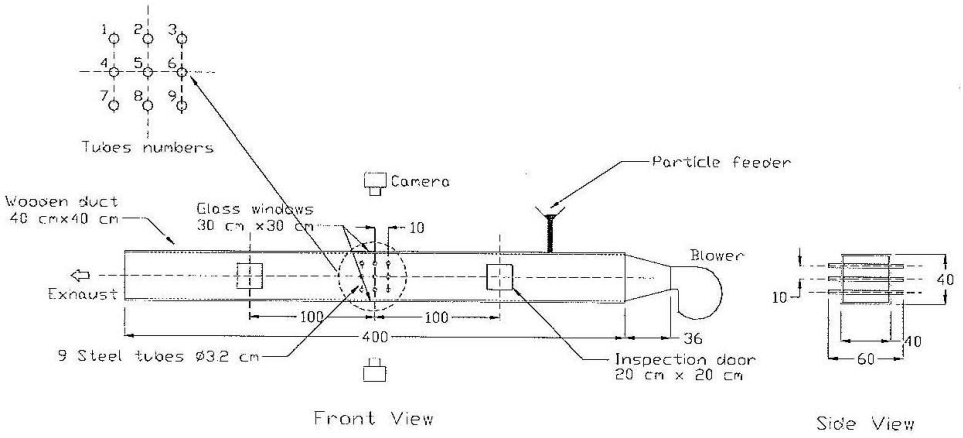

FIGURE 8.1.1. Drawings of the simulated facility taken from [**42**]. Dimensions are in cm.

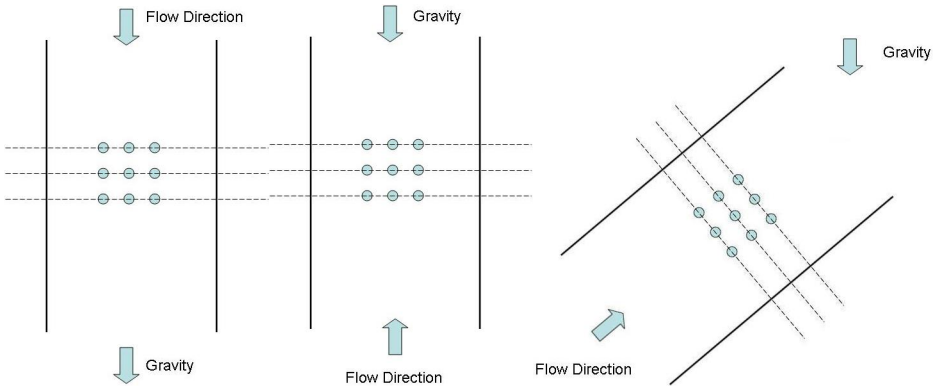

(a) Downstream (b) Upstream (c) Stream 45 deg

FIGURE 8.1.2. Sketches of the cases selected for the simulations[**42**].

particles had a Gaussian distribution of 40 μm mean and ± 16 μm as standard deviation. Particle injection rate was of 20 g/m^3, air flowrate it was 0.2 m^3/s.

8.2. Numerical Strategy

The fluid dynamics of a narrow configuration 3×3 of tubes in a constant air stream is affected by shedding and unsteady swirl motion, which influence flow behavior on rows of downstream tubes. Therefore, 3D Large Eddy Simulation (LES) was chosen for the CFD investigation.

An overview of the fluid dynamics is shown in the animation [Weblink Bundle Downstream], for the downstream configuration.

Since the injected particles are homogeneously distributed in the main air stream, to run a steady particle tracking, to identify the most probable hosting cells[1], was considered unnecessary. A LES simulation was performed of the entire facility, see Fig.8.2.1a, with an integration time step of 10^{-3} s. 5000 LES frames were saved and processed for the domain reduction. Particles were injected at the upstream side of the reduced domain, see Fig.8.2.1b. Particle to particle interaction was enabled to simulate particle removal due to particle impact. RTDE was not enabled because of storage memory (hard disk) capacity: the P^3 elaborates and saves data on the local drive where the source files from the commercial CFD were stored, and data exceeded the available capacity of 1 Tera Byte. Furthermore, the main aim was to investigate the motion of the greatest number of particle, both to capture backside tube deposition and to test the robustness and the computational speed of the particle tracking algorithm. Concerning the latter issue, implementation of the algorithms require indeed a computational optimization.

8.3. Numerical Simulations

8.3.1. Downstream Configuration.

Concerning the three cases investigated, the focus was on to the two upstream cases since the downstream deposition has been already extensively investigated and validated on the deposition of glass particles in the LCS facility, described in the chapter 7. The downstream simulation is qualitatively in agreement with the experimental pictures reported in[**42**], see Fig.8.3.1: deposition occurs mostly on the first row of tubes, decreasing in thickness and becoming scattered on the second and third row.

[1]Such operation is required to go from the complete to the reduced domain, since depending on the domain selected, particles have to be injected in the most probable locations pointed out as particle hosting cells.

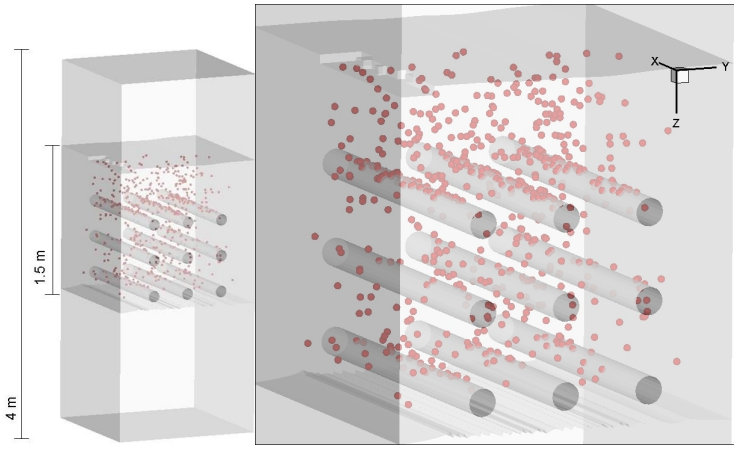

(a) Complete domain (b) Reduced Domain

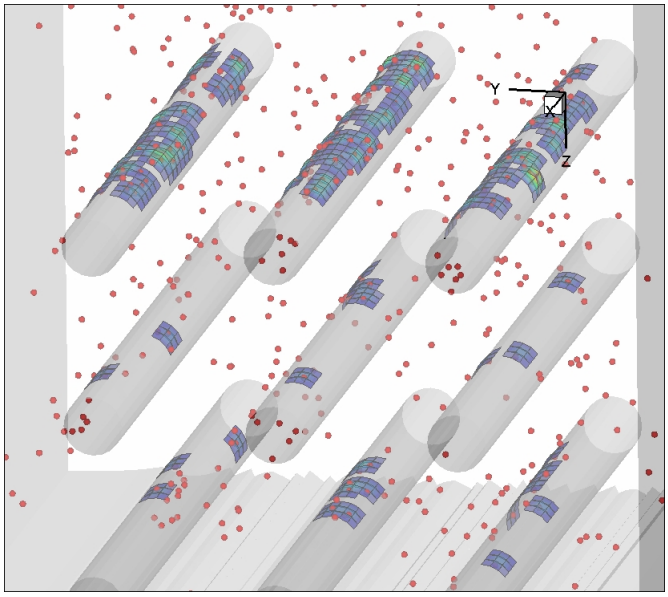

(c) Particle deposition, downstream configuration

FIGURE 8.2.1. Complete and reduced computational domain example, taken from the simulation performed on the experimental facility described in Elhadi and Rindt[**42**]: a) Complete and reduced domain. LES CFD calculations have been performed on the complete domain while the unsteady particle tracking has been performed only on the reduced domain. b) Snapshot of particle deposition in the reduced domain. c)Detailed snapshot of particle and deposit growth.

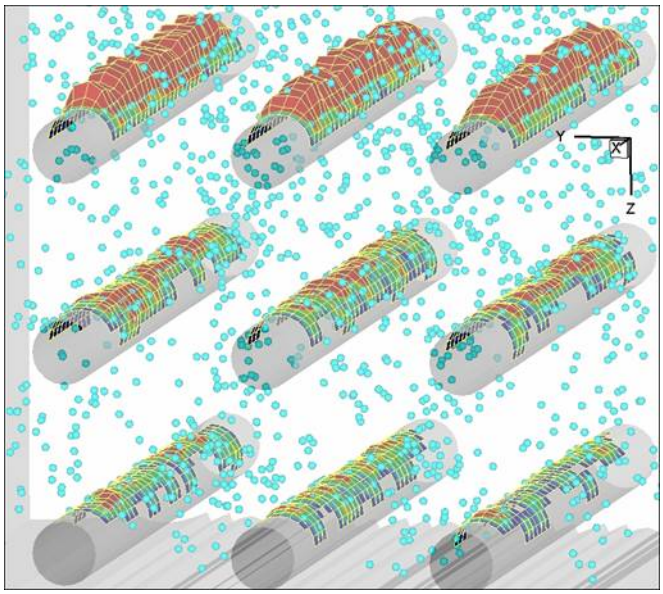

FIGURE 8.3.1. Downstream deposition

8.3.2. Upstream Configuration.

Deposition in the upstream cases, straight and 45 *deg.*, occurs also at the downstream side of the tubes: due to swirl and gravity effect heavy particles fall near on the downstream stagnation point where they cannot be removed by other particles or by the main stream. This behavior is captured both in the 90 *deg.* and in the 45 *deg.* upstream simulation, see Fig.8.3.2 and Fig.8.3.3. Particles depositing on the backside of the tubes belong mostly to the biggest particle size class. Very light particles are instead dragged towards the outlet, with a very few of them depositing, while intermediate size particles (i.e., near the mean value of the given Gaussian distribution 40 μm) constitute the majority of those deposited.

Animations are available at [Weblink Bundle Upstream 90 deg. - a], [Weblink Bundle Upstream 90 deg. - b], [Weblink Bundle Upstream 45deg] and [Weblink Bundle Upstream Multiparticle 90 deg.], while a summary of the strategy applied is reported in Table 1.

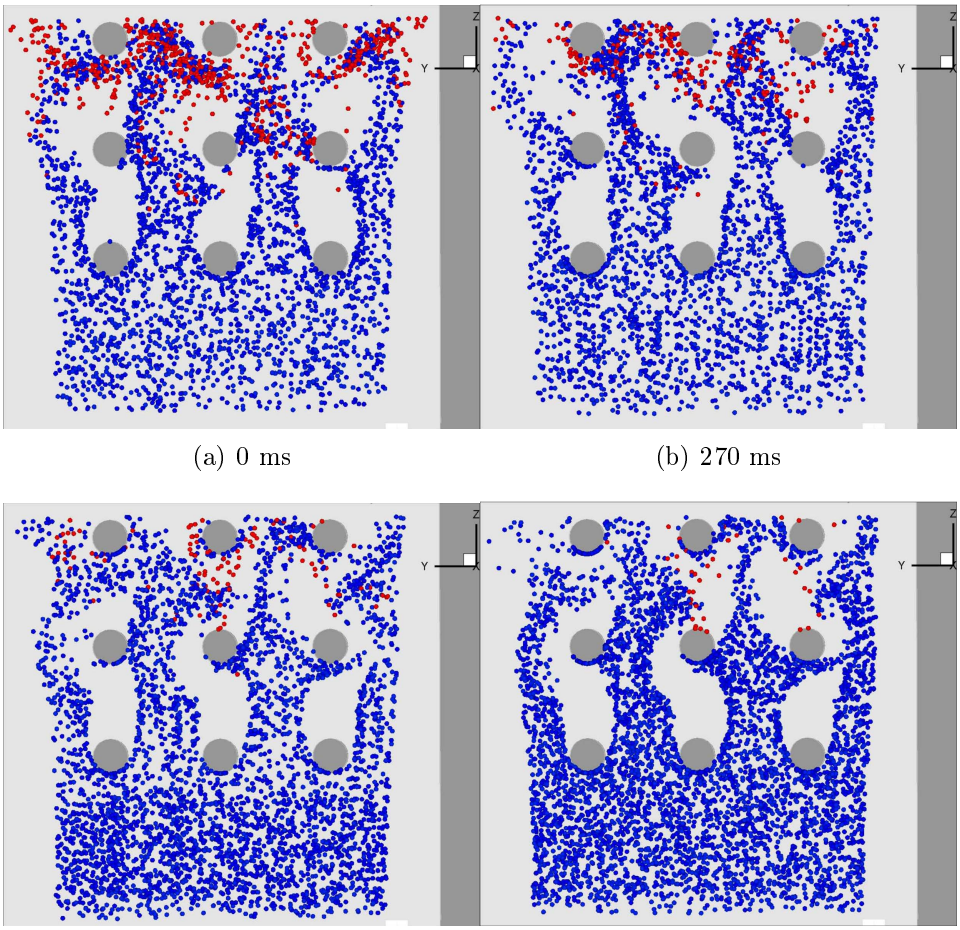

(a) 0 ms (b) 270 ms

(c) 420 ms (d) 510 ms

FIGURE 8.3.2. Upstream 90 *deg.* flow. [Weblink Bundle Upstream 2P-a] and [Weblink Bundle Upstream 2P-b]

CFD	P^3 *Strategy*	*Particle Tracking*	*No.Particles*	*VEM*
LES	*Reduced Domain*	*Unsteady*	294828	*SLS*

TABLE 1. Bundle of Tubes Summary Table

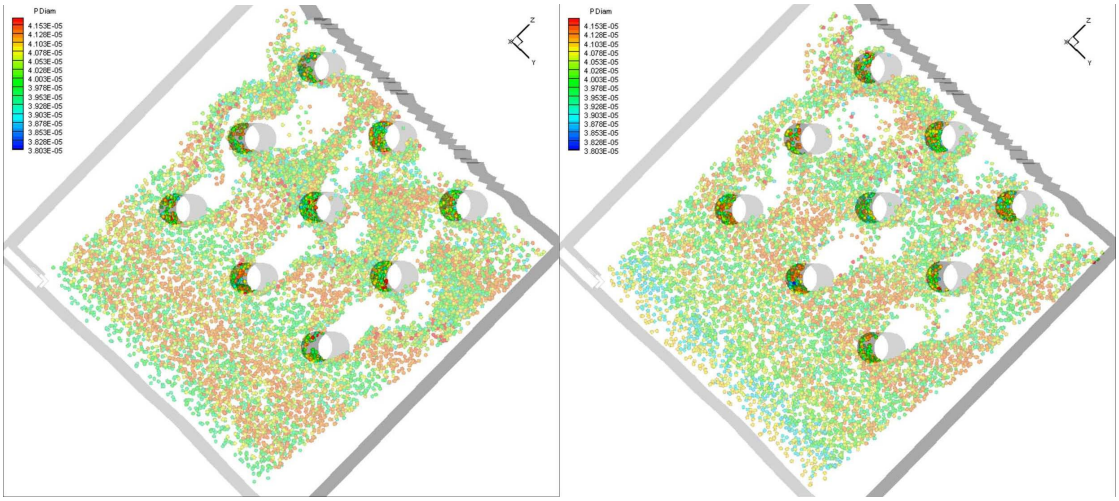

(a) 150 ms (b) 210 ms

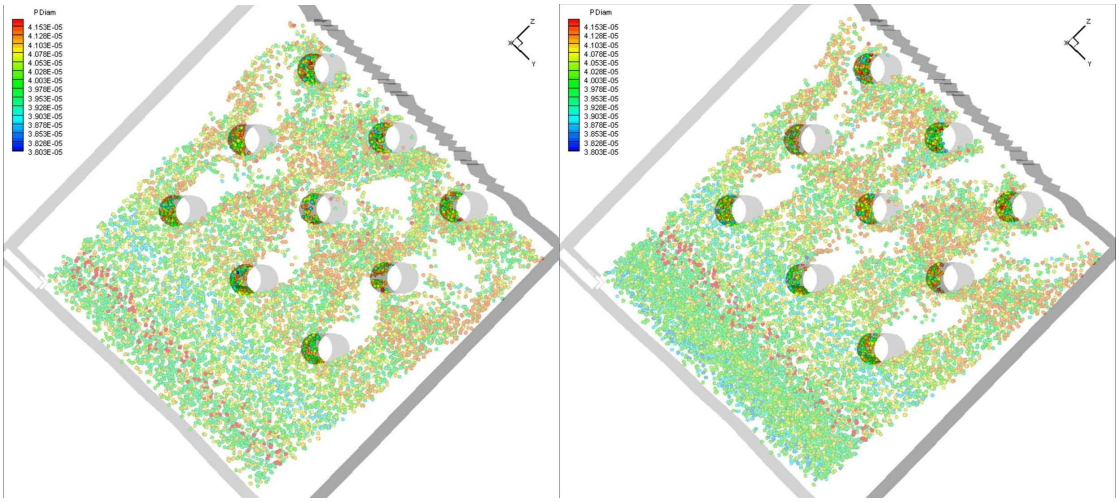

(c) 360 ms (d) 540 ms

FIGURE 8.3.3. Upstream 45 deg. [Weblink Bundle Upstream 45deg]

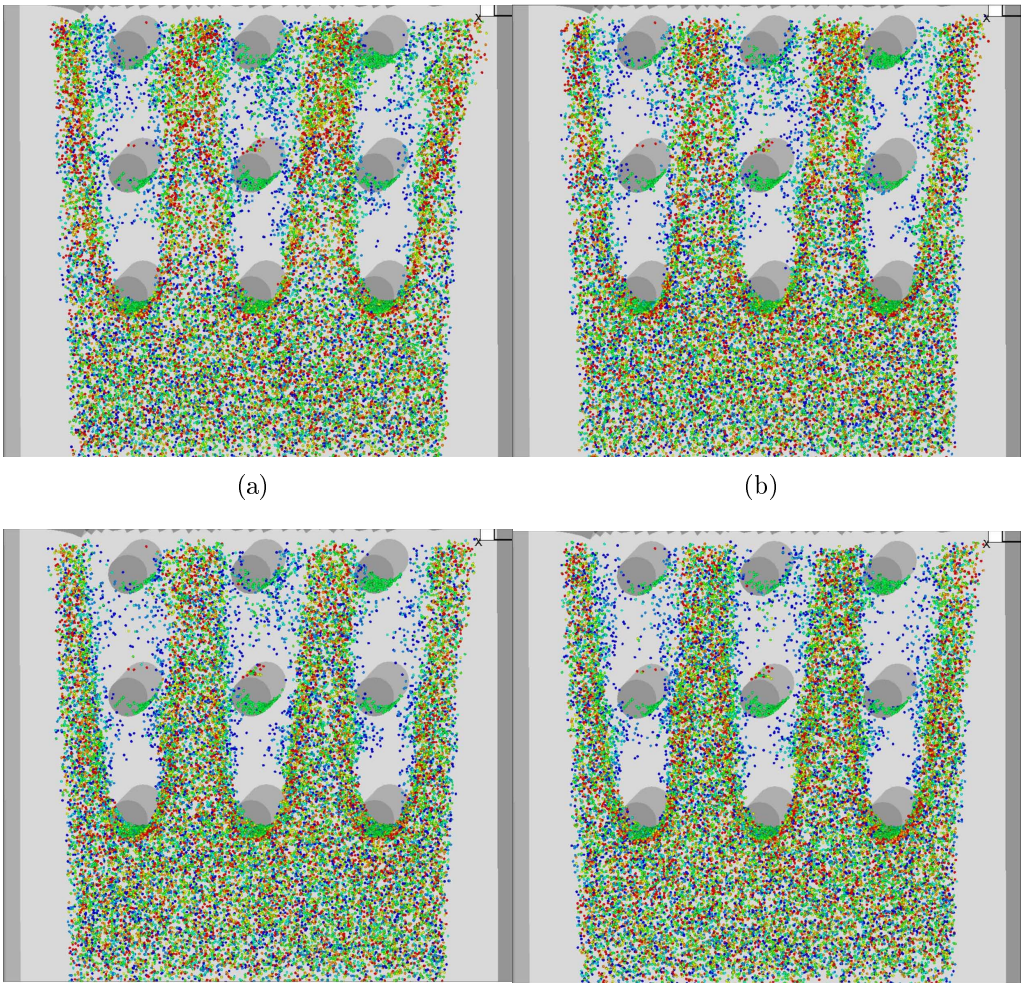

(a) (b)

(c) (d)

FIGURE 8.3.4. Upstream 90 *deg.* case. [Weblink Bundle Upstream Multiparticle]

CHAPTER 9

Sand and Soil Separation

"Time cools, time clarifies; no mood can be maintained quite unaltered through the course of hours..."

- Mark Twain

9.1. The Reflux Classifier

"A reflux classifier is a device in which inclined plates are used for segregating particles by size or density using a fluidized bed in a chamber. Arrays of inclined plates form lamellae and divide the chamber into zones into which particles of predetermined size or density migrate. Particle differentiation is controlled by plate length, inclination and spacing in each array, combined with fluidization rate."

9.1.1. Introduction.

In this section the work performed on the Reflux Classifier is presented. Such a technology was patented by Dr. Galvin[1] [Weblink Reflux Classifier Patent] at the University of Newcastle and currently in use in coal mining, and in ashes, sand and waste particle separation processing. A picture of the patented geometry is shown in Fig.9.1.1a. Because of the natural link of the particle tracking post-processor to

[1]Reflux classifier. United States Patent 6814241. Inventor: Galvin, Kevin Patrick (New South Wales, AU). *http://www.freepatentsonline.com/6814241.html*

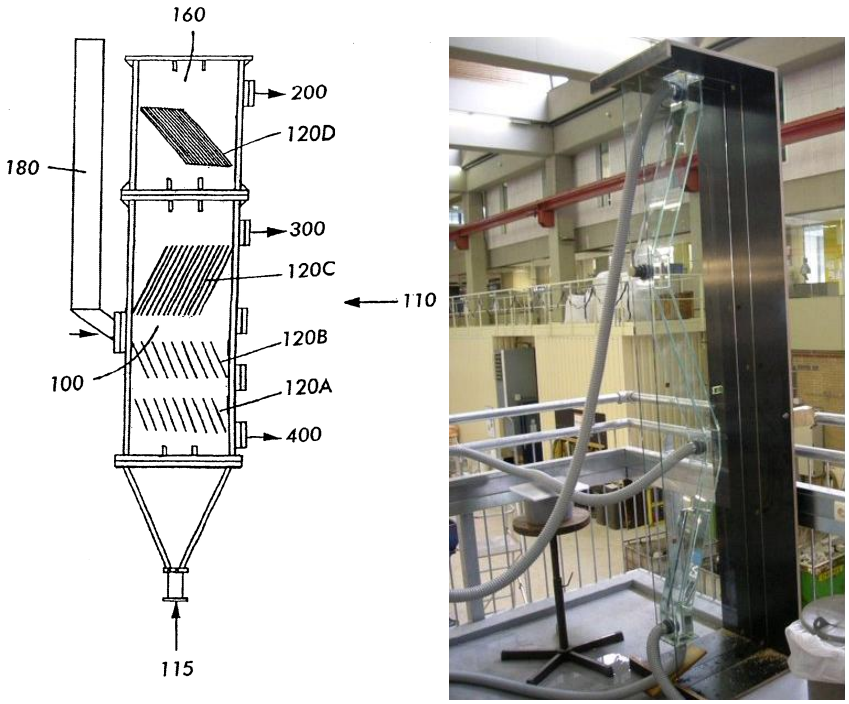

(a) (b)

FIGURE 9.1.1. Reflux Classifiers. a) USA patent drawing. b) TU Delft facility

granular dynamics and (mechanical) particle separation, the reflux classifier is a suitable candidate to investigate CFD RANS and LES particle dispersion in post-processing. Furthermore, a simplified model is under investigation at TU Delft[2] [Web Link TUDelft Reflux Classifier]. This simplified geometry was then selected for the purpose of the numerical tests on the P^3, see Fig.9.1.1b.

9.1.2. Background of the invention.

In many industrial processes it is necessary to classify particles according to their size or density. For example, screens, cyclones, and

[2]Recycling Technology Group at the Faculty of CiTG (Department of Geosciences) of Delft University of Technology[CiTG Homepage]: http://www.tudelft.nl/live/pagina.jsp?id=7d284c0f-39f1-42ce-9124-8dac69ff40c6&lang=en.

elutriators are often used in mineral processing to sort particles. Classification, or separation, may proceed either in a wet or dry state. Although the aim may be to separate the particles of specific sizes, there is usually a high degree of so-called misplaced material, that fulfills the conditions specific for other material.

(1) Sieve separation devices[3] provide perfect separation of particles, only if smaller than the openings. However, if particles are not allowed sufficient time on the sieve, poor separation results. Relatively fine particles, less than 45 μm in diameter, readily adhere to other particles, and are therefore difficult to separate using sieves. Sieves also tend to become blinded by particles which are similar in size to the openings, and operate poorly when particles are fed on a continuous basis.

(2) Elutriators[4] separate particles according to their settling velocity. If the particles are of the same density, then the separation proceeds in accordance with the particle size. A liquid passes up through the elutriator vessel at a specific velocity, carrying slower settling particles to the top, thus allowing faster moving particles to be withdrawn from near the base of the vessel. However, elutriators may fail to provide satisfactory throughputs, especially when the separation size is relatively small.

(3) Cyclones[5] provide remarkably high throughputs although their efficiency is substantially poor and the separation size more difficult to control, or simply limited into splitting particles into 2 categories (coarse and small).

[3]Typically mechanical separation devices as membranes and screens, whose piercing dimension (sieve) gives the filtering capacity

[4]From Latin *elutriatus*: to put in a vat, to purify, separate, or remove by washing

[5]High velocity devices at use in fluidized beds and gasifiers to separate coarse and small particles by means of forcing the flux to be separated by gravity during their swirling motion into a upside-down cone shape device. Coarse particles are collected at the smaller bottom-end.

(4) Inclined classifier have the potential to offer satisfactory throughputs, and efficient separations. They are better known as Vertical Elutriators (VE) or "S" shape Elutriators.

However, even with 4 solid particles settle on inclined or horizontal plate devices and may move downwards as a secondary phase flow. In laboratories, inclined devices have also been used to classify particles according to both size and density. Indeed, this methodology of segregation or classifying particles may also extend to the following applications:

i): the classification of particles less dense than the fluidization fluid, where the system described operates in reverse, with the fluidization fluid flowing downwards and the particles settling upwards;

ii): gas fluidization of relatively fine particles;

iii): segregation or classification of liquid droplets or air bubbles such as that required in the draining of a foam in foam fractioning.

9.1.3. The Inclined Classifier Segregation Strategy.

According to the so called Inclined Classifier strategy, the system is fed with particles to be separated. Due to buoyancy and wall shear stresses, solid particles gradually settle towards the inclined surfaces as the solid-liquid mixture is carried upwards. Finer solids or particles are transported along the stream (overflow) while coarse solids or particles may slide down the incline separator surfaces (underflow), as depicted in Fig.9.1.2. The fluid moves through the plates, or the vessel itself, at velocity U, hence fluid residence time is $t = l/U$, where l is the plate length. During this period the solid particle moves at a velocity $V \cdot \cos\theta$ normal to the incline, where V is the particle velocity , and θ is the angle with the horizontal. Assuming a width, h, between the plates, then $V \cdot \cos\theta = \frac{h}{t} = \frac{h \cdot u}{l}$. Therefore, the critical particle velocity is, $V = \frac{h \cdot u}{(l \cdot \cos\theta)}$ (see Fig.9.1.2).

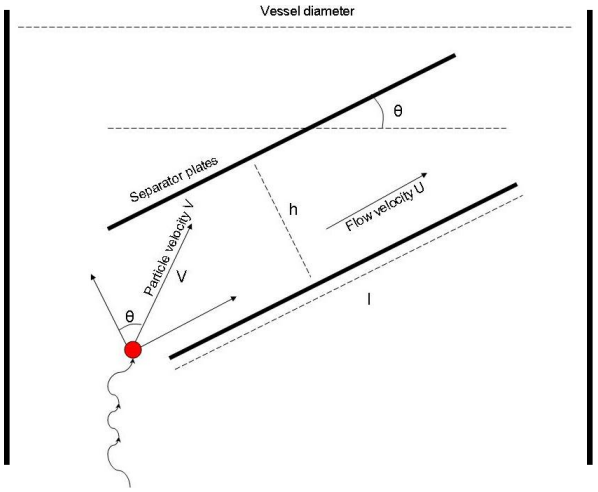

FIGURE 9.1.2. Sketch of Reflux Classifier

At a given suspension concentration, the value of V depends on the particle size, assuming the solid particle density is constant. This equation provides a basis for selecting the separator plates width, length and angle. Ideally, the angle should be about 60° degrees. Higher angles will not amplify the segregation significantly. Lower angles may lead to build up of solids or particles on the incline. Since the increase in the settling rate is given by the ratio of the projected settling area to the cross-sectional flow area, by inclining a vessel the length l and narrowing the width h, significant rates of separation can be obtained. That is, $U/V = l\cos\theta/h$. A separator device consisting of many plates separated by a narrow gap h may consistently increase the particle segregation efficiency.

The segregation efficiency of the inclined classifier mainly depends upon mass, momentum and energy ratios between the solids and the liquid solution. The geometrical parameters l, h and θ have the effect of reducing the vertical velocity (limiting height reduced by $\sin^2\theta$). The main paramenters are:

(1) particle buoyancy, hence the ratio $\frac{\rho_p}{\rho_f}$
(2) feeding rate ratio or momentum ratio $\frac{\rho_p V_p}{\rho_f U}$

(3) Particle kinetic and potential energy $\frac{1}{2}V_p^2 \sin^2\theta = g \cdot H_{limit}$, where H is the vertical limit height (heavy particles)

For colloidal mixtures or for very fine particles, the classifier may segregate but not collect all of the injected particles, leaving the smallest to fluctuate and reach the outlet. Every filtration or separation system has a particle diameter range of selectivity. As reported in the patent, the inclined classifier works in a range 5 mm to 45 μm using water based fluids. As in item 1, decreasing the buoyancy, increases the segregation between the solid and liquid phases.

9.1.4. Numerical Results.

Unsteady particle tracking simulations have been performed on a geometry resembling the one at use in TU Delft. Dimensions were roughly estimated according to the dimension ratios showed in Fig.9.1.1b and information in the patent. Different size sand, 0.5, 1.0, 1.5 and 2.0 mm, (particle density $\rho_p = 1300\ kg/m^3$) to mimic soil separation were injected in water. An overview of the simulated facility is given in Fig.9.1.3. Since no specific experiment was attempted, no particle statistics (time averaged results) were known. Therefore only unsteady particle tracking by RANS and LES CFD simulations is reported here.

Two flow configurations have been investigated, at $\overline{U} = 1\ m/s$ and $\overline{U} = 2\ m/s$, where $\overline{U}$ is the average velocity of the water inlet at the bottom. Despite the very low overall Reynolds number and the low velocities, the author refers to them here respectively as *"low"* and *"high"* velocity cases, see Table.1. RANS and LES simulation were performed using the Fluent CFD code. RANS $\kappa-\omega$, LES Smagoringky SGS model, integration time step 0.001 s, mesh: 103314 hexahedral cells, fluid: liquid water.

9.1.4.1. *RANS Simulations Results.*

According to the patent description, the classifier is meant to separate dilute solid-liquid mix. The more the difference in density between

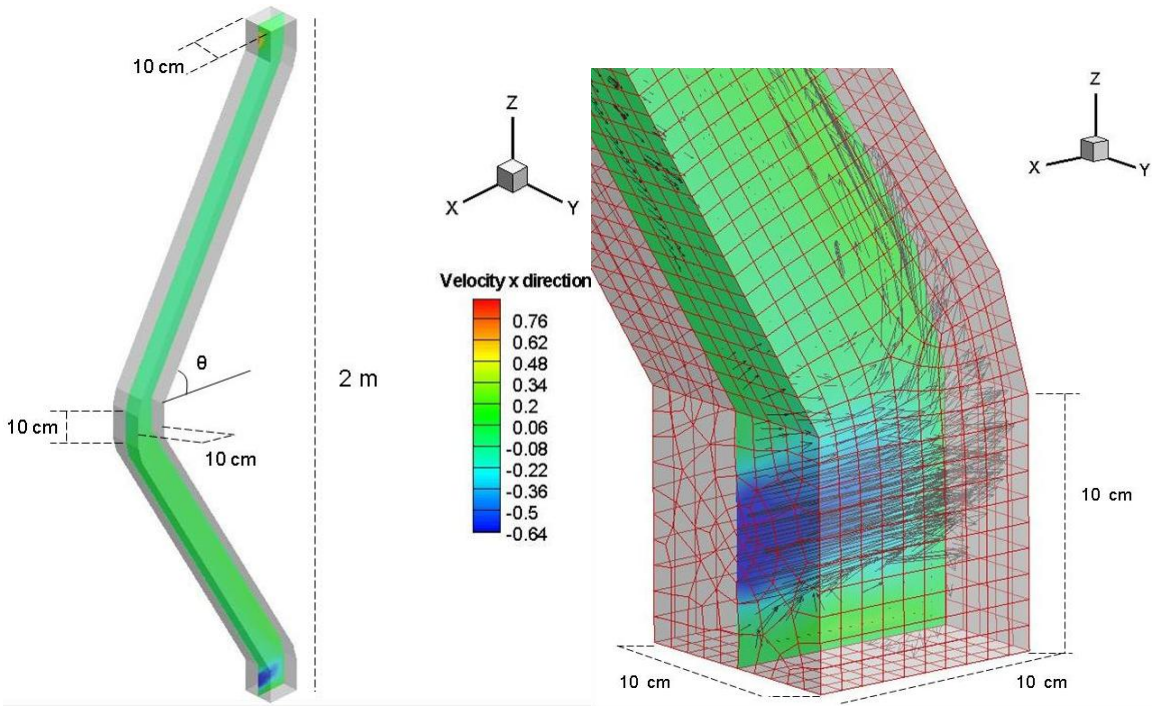

(a) (b)

FIGURE 9.1.3. Reflux Classifier Overview. $\theta = 60°$

Velocity	*Data*	CFD Simulation
Low	$middle:\ 0.1\ \frac{kg}{s} \Rightarrow \bar{V} = 0.0351\ \frac{m}{s}$ $bottom:\ 1.2\ \frac{kg}{s} \Rightarrow \bar{V} = 0.4215\ \frac{m}{s}$	RANS
High	$middle:\ 1.0\ \frac{kg}{s} \Rightarrow \bar{V} = 0.3512\ \frac{m}{s}$ $bottom:\ 2.0\ \frac{kg}{s} \Rightarrow \bar{V} = 0.7025\ \frac{m}{s}$	RANS, LES

TABLE 1. Reflux Classifier Simulations Data

the solid and the liquid phase, less is the buoyancy and the more efficiently the classifier works. Working with a dilute water solution at

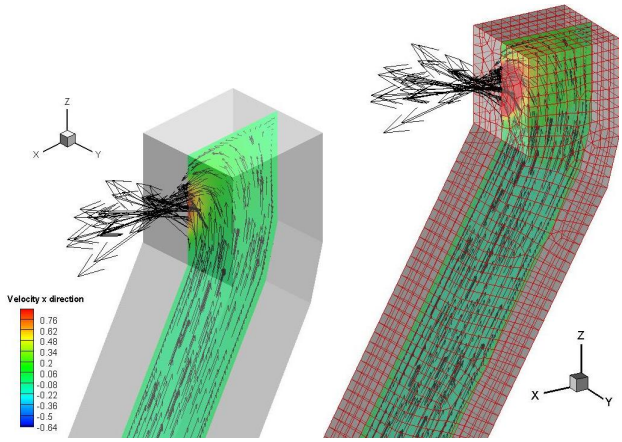

(a) Low Velocity - Top (b) High Velocity - Top

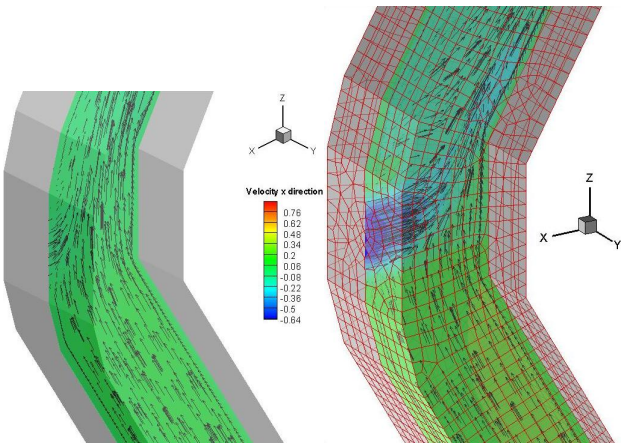

(c) Low Velocity - Middle (d) High Velocity - Middle

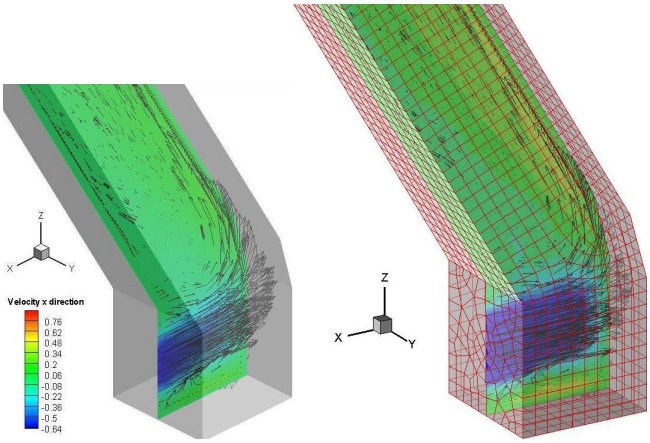

(e) Low Velocity - bottom (f) High Velocity - Bottom

FIGURE 9.1.4. Reflux Classifier: RANS comparison between slow and fast water velocity injection

low Reynolds numbers[6] is a perfect test case to be investigated using a RANS approach. The $\kappa - \omega$ turbulence model was selected only to debug the switching subroutine $\kappa - \varepsilon$ / $\kappa - \omega$ of the P^3. The total time investigated is about 40 s. As shown in Fig.9.1.5 and on internet at [Weblink Relfux Classifier RANS - Low], heavy particles deposit primarily downstream and at the tip edge of the upstream inclined shaft. The lighter the particles, the higher along the classifier they deposit. With the assumed water mass flow rate, density and size of the particles, none of them reaches the way out at the top. On the contrary, in the higher velocity case shown in Fig.9.1.6 and [Weblink Relfux Classifier RANS - High], heavy particles deposit only upstream, whereas nearly 13% of the total, which is 6.6% of the lightest group of particles, reach the outlet of the classifier. Due to the higher velocity of the flow phase, particle can obviously deposit only in low speed locations, such as at the edges connecting the walls of the shaft. Alongside the corners the flow velocity is nearly zero, and the energy loss due to viscous drag and wall friction[7] may be sufficient to stop particles. The same deposition behavior is captured by the LES investigation (*"higher"* velocity).

9.1.4.2. *LES Simulation.*

Due to the configuration and the particle deposition of the classifier, increasing the velocity in the separation zone (central location) may let swirl appear, and the steady state CFD analysis no longer appropriate. Concerning this matter, no substantial differences between the unsteady particle tracking on RANS and LES background were noticed except for the fact that particles (at the injection location) appear to be more uniformly distributed. Furthermore, even heavy particles are transported along the upstream shaft for a longer distance before depositing. Nevertheless, for the assumed mass flow rates, the more

[6]This is the assumption of the author of this dissertation

[7]Alonge the corner edges particles are tangent to the bottom and the side wall, fact that counts for two impacts and energy loss on two wall at the same time.

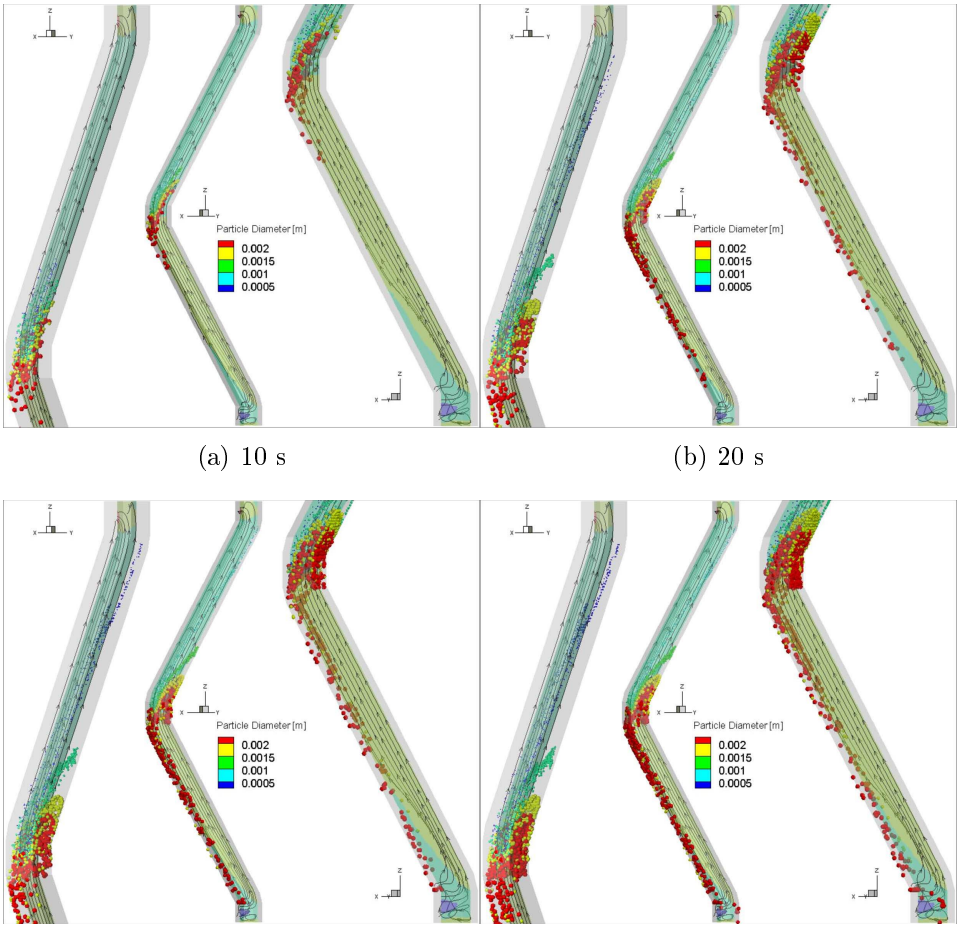

(a) 10 s (b) 20 s

(c) 30 s (d) 40 s

FIGURE 9.1.5. Reflux Classifier, RANS low Velocity. Total time 40 *s*. Animation available at [Weblink Relfux Classifier RANS - Slow].

intense diffusion captured in the frameshots does not substantially influence the overall deposition rate. The CFD streamline visualization is shown at [Weblink Relfux Classifier LES Streamlines]. Particle animation is available at [Weblink Relfux Classifier LES].

A brief summary of the strategy applied is reported in Table 2.

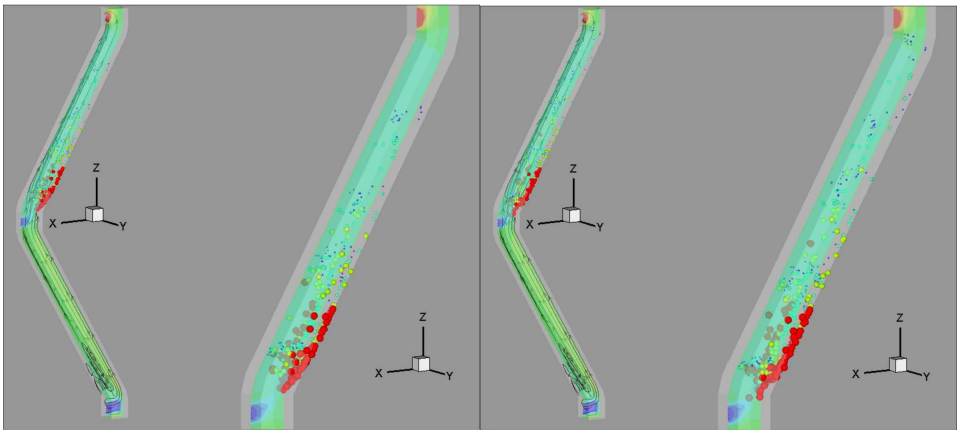

(a) 3 s (b) 4 s

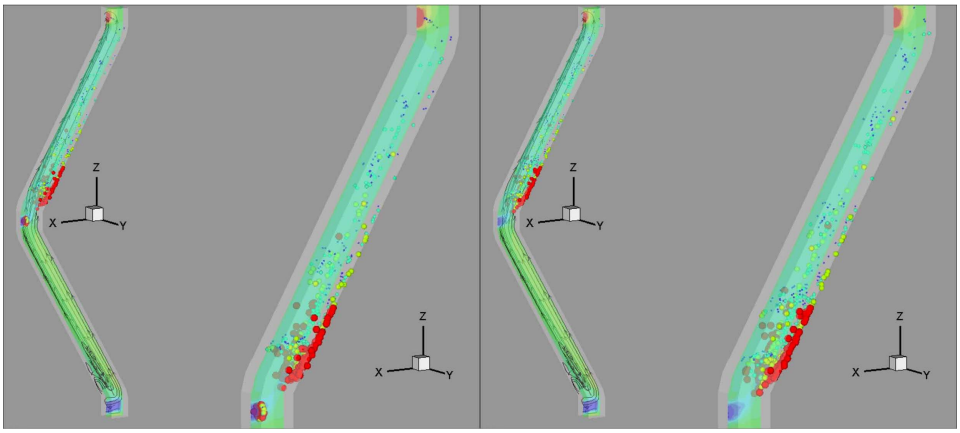

(c) 5 s (d) 6 s

FIGURE 9.1.6. Reflux Classifier, RANS High Velocity. Total time 6 s.

CFD	*Particle Tracking*	*No.Particles*	*VEM*
RANS	*Unsteady*	3080	*SLS*
LES	*Unsteady*	6088	*SLS*

TABLE 2. Reflux Classifier Summary Table

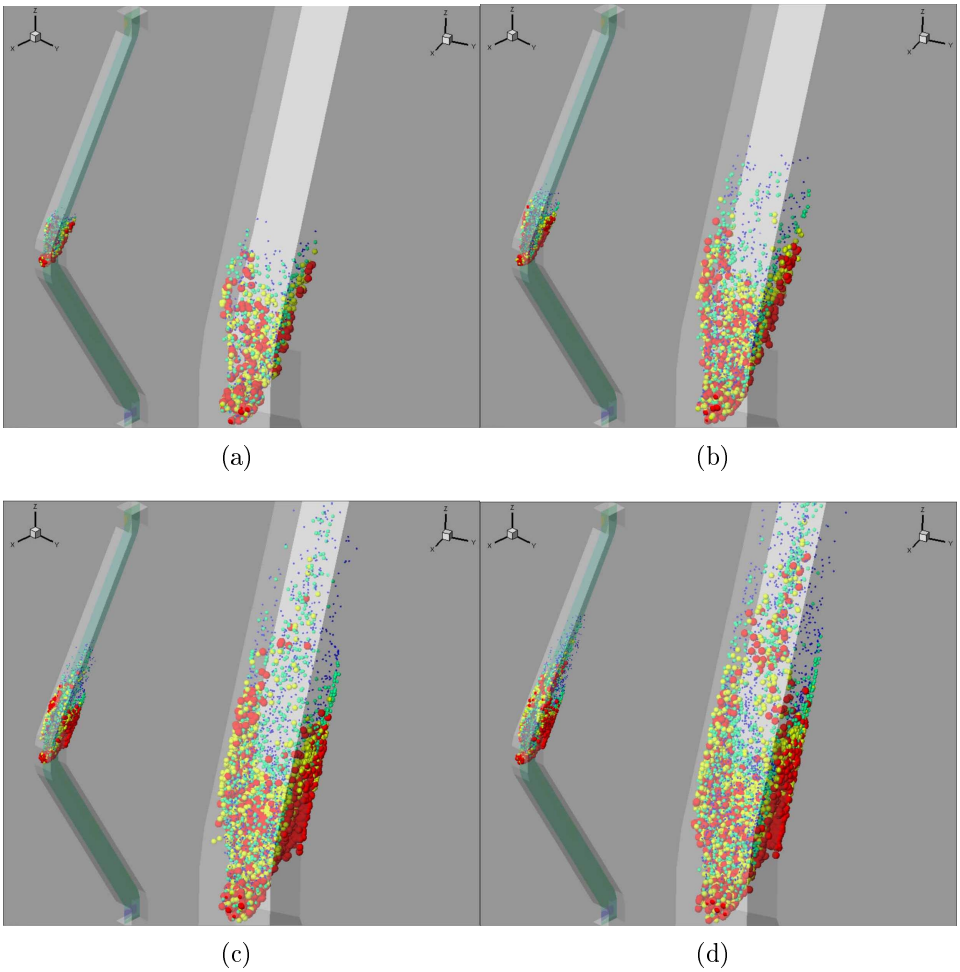

(a) (b)

(c) (d)

FIGURE 9.1.7. Reflux Classifier LES. [Weblink Relfux Classifier LES]

9.2. Horizontal pipeline

9.2.1. Introduction.

In several industrial process pipelines may get obstructed either by fouling or simply continuous deposition of solid granular matters advected downstream. In Fig.9.2.1a, the cross section of the deposit occurred along an old industrial water pipe is shown, whereas Fig.9.2.1b shows an attempt to simulate water limestone scaling, which occurs by fouling and sedimentation due to local shear stress, temperature

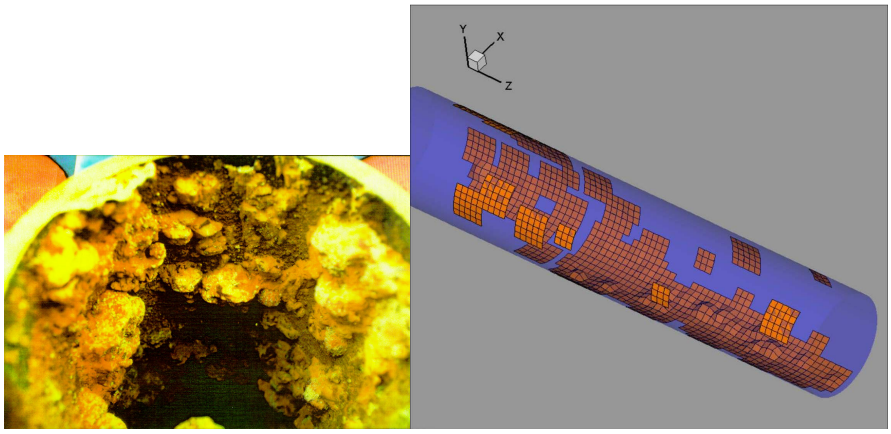

(a) 30 years old 8 inch water pipe (b) 2 m diameter, 10 m length water pipe

FIGURE 9.2.1. Water scaling. a) real severely obstructed and b) example of Step-RANS in a water pipe.

gradients and evaporation in shallow water. Even though limestone is generally identified with calcium carbonate ($CaCO_3$), it may considerably vary in composition having among its main components also silicates, clay and sand. Such a composition still lies in the range of ashes where the viscosity interpolation implemented in the P^3 computer code is valid. The main assumption in this scenario is the fact that deposition mainly occurs because of slow sedimentation due to shear stress at the solid surfaces, while the model implemented considers only the mechanical impact as the cause of deposit. This modelling limit can be overcome by assuming:

(1) Large number of tracked particles
(2) Scatter factor = 1

Concerning the first item, mechanical impact may correctly predict local concentrations only if a statistically significant number N of particles is tracked. Since the deposit thickness may be locally overpredicted, unless $N \to \infty$, it seems reasonable to set the scatter factor to 1 to account for the calculated deposit on a wider area.

9.2.2. Numerical Strategy and Results.

The numerical strategy, nicknamed Step-RANS, is based on sequential RANS and steady particle tracking calculations: the goal is to simulate long term deposits by means of progressive (sequential) steady states. The non trivial part of this approach is the generation of the new grid (deposit-updated) to be introduced again into the commercial CFD code for each sequential new RANS run. Theoretically, there are no limiting assumption preventing this approach from being applied to LES calculations as well as for RANS. The computational procedure described in Fig.9.2.2a has been demonstrated using Fluent and is listed in Alg. 6 (following reported). The P^3 exports text file which has nodes and Cartesian coordinates listed in the same order required by the commercial CFD code. Each new mesh keeps the same node connectivity, so it is not necessary to perform any re-triangulation process. The new set of coordinate is simply meant to be cut/copied and pasted into the original CFD file containing the mesh information[8]. Information about node deposit thickness or thermal resistance cannot be imported (back) into the commercial CFD, since these variables were not present in the CFD source itself. Concerning the node temperature and composition, the main problem (not solved in this dissertation) is the inconsistency of the updated value of these variables with the CFD code boundary conditions. Boundary conditions are assigned as a uniform conditions (for pressure, temperature, heat transfer, etc...) span all the nodes belonging to the boundary surface of interest. In other words, the process of moving mesh nodes may assign (update) a new temperature to the nodes according to time and local node thickness and thermal resistivity (which primarily depends upon node composition). The new temperature will be lost anyway after the first iteration is performed when back into the CFD code, because the temperature assigned in the CFD at the boundary surface will be re-assigned to all the nodes belonging to that surface.

In the chart in Fig.9.2.3, the Step-RANS loop and steady particle tracking has been performed eleven times, that is roughly equivalent

[8] For Fluent, the file to be opened and changed is the *.cas file.

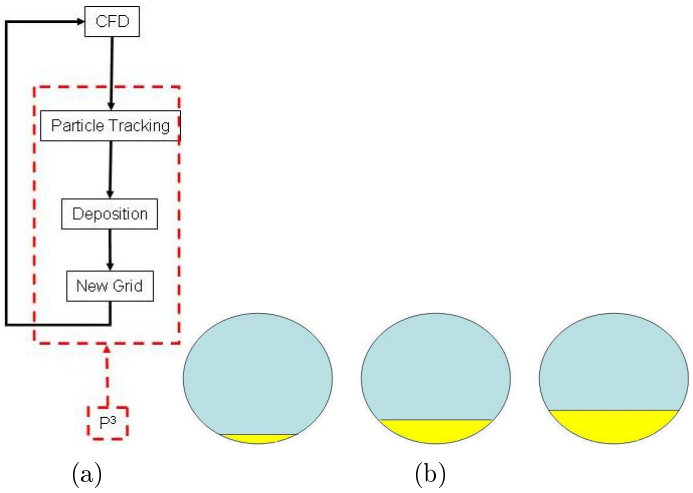

FIGURE 9.2.2. Sand-Water Pipeline Deposition. a) Step-RANS Computational Scheme, b) sketch of the deposition process to be simulated.

Algorithm 7 Step-Rans Algorithm

(1) A "clean" RANS (or LES) is run (zero deposit)
(2) start loop
  (a) particles are added and tracked in post-processing (see animation [Weblink Sand-Water Particle Deposition])
  (b) deposit thickness locally evaluated and node position updated
  (c) the new grid is exported and uploaded back into the CFD
  (d) a new CFD run is performed on the new mesh.
(3) go to point 2 (end loop)

to 250 *hrs* running under sedimentation conditions. In Fig.9.2.4a-d, a few snapshots from the animation [Weblink Sand-Water Deposition] are reported. The facility simulated is 2 m diameter and 10 m length. The most important result is the switching between the curves representing the deposited and the ejected particles: due to the rapid growth of the deposit, the flow axial velocity increases (at constant inlet mass flow rate), a fact that inevitably speeds up the particles towards the outlet. It is the numerical assumption of constant inlet flow rate that implies and produces the asymptotic behavior to the deposit growth (mass of

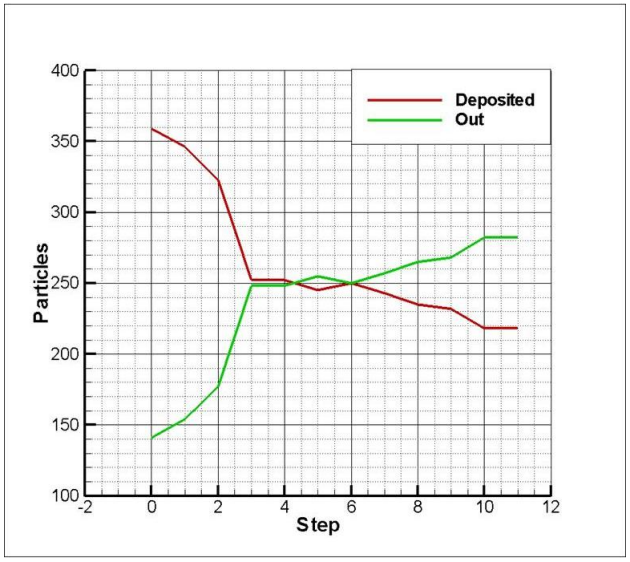

FIGURE 9.2.3. Step-RANS. Prediction of Deposited-Out particles

CFD	P^3 $Strategy$	$Particle$ $Tracking$	$No.Particles$
$RANS$	$Step - RANS$	$Steady$	$500/RANS$

TABLE 3. Sand Deposition Summary Table

deposited particles$\rightarrow$ 0). In a real facility, the inlet mass flow rate varies, decreasing its value due to the chocking effect or obstruction of the pipeline. Reducing the flow velocity, and hence the particle velocity, keeps actually the number of deposited particle increasing which leads to an increasing deposit thickness, finally obstructing the facility. A brief summary of the applied strategy is reported in Table 3.

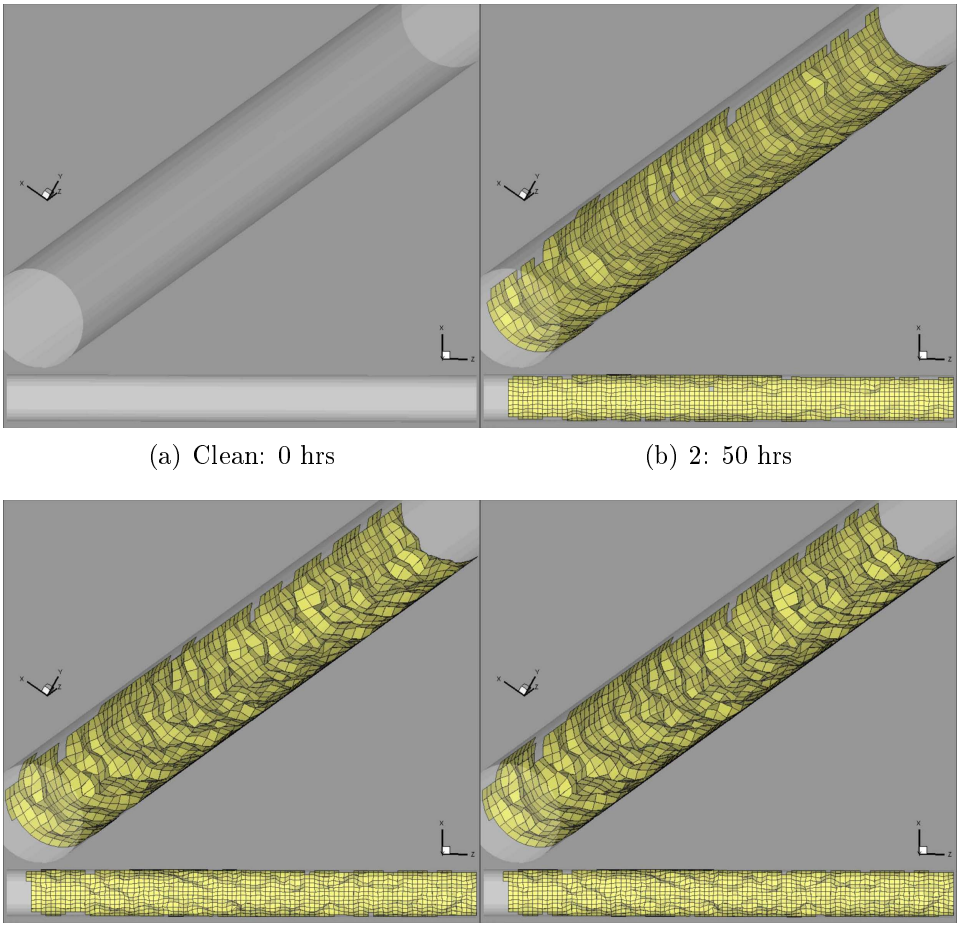

(a) Clean: 0 hrs

(b) 2: 50 hrs

(c) 6: 150 hrs

(d) 10: 250 hrs

FIGURE 9.2.4. Simulation of sand-water pipeline deposition. Animation available on Internet [Weblink Sand-Water Deposition]

CHAPTER 10

Scraper Crystallizer

"Nothing is as far away as one minute ago..."

- Jim Bishop

10.1. Motivation

In this chapter the work performed in co-operation with M. Rodriguez, Ph.D. student at the TU Delft in the Process & Energy Department is reported. This interdisciplinary work represents a practical example of the straightforward applicability of deposition studies applying a viscoelastic approach. The main aim is to investigate and point out the limiting assumptions of both the Large Eddy Simulation data post-processing and the mathematical modelling. In this attempt, the linear viscoelastic formulation was used. Future works will be focusing on non-linear approaches for melting solids and liquids at freezing temperatures (ice). The animations concerning this work are available on Internet at [Weblink Salt Scraper] and [Weblink Salt Scraper-monosize]. The simulation with one size salt crystals was performed assuming the initial position of the crystals to be within a 2 cm strip from the scraper plate (bottom). Such an initial condition was meant to mimic the volumetrical dispersion of the particles due to the start-up motion of the scraper.. Simulating 2 mm salt crystals produced indeed a built up which is closer to the experiment but the crystals were originally of different dimensions and placed at ground level, whereas in the case shown [Weblink Salt Scraper Single Size]. Solid glass particles were also simulated, even though no experiments

of this kind were meant to be performed. Glass particles were homogeneously distributed on the bottom of the tank. Since particles were distributed in boundary wall cells at the bottom tank surface, the non-negative normal velocity condition of the fluid phase and the weight of the solid particles (heavier than salt crystals) prevented the particles from forming any consistent built up at the front end of the scraper [Weblink Glass Particles single size]. The main conclusion is that an homogeneous distribution of single size particles, tangent to the bottom surface may not correctly represent particle agglomeration at the front end of the scraper.

10.2. Introduction

Fouling is a problem in several crystallization processes such as evaporative, cooling, freeze or eutectic freeze crystallization, and also in other industrial processes such as slurry storage, boilers and food processing. The higher supersaturation close to the heat exchangers compared with supersaturation of the bulk solution is the main cause of this phenomenon. This supersaturation provokes higher nucleation and growth rates. If no action is taken a scale layer of crystals builds up on the heat exchanger surfaces thus drastically decreasing heat transfer efficiency. Since heat transfer is necessary to crystallization, this decrease can cause failure of the crystallization process. Continuous scraping of the heat transfer surfaces is commonly used to prevent scaling (fouling). This mechanical action affects the fluid flow and particle dynamics in the crystallizer. The shapes, velocities and positions of the scrapers and the heat exchangers create a new turbulence situation close to the heat exchanger surface. The turbulent fluid flow which keeps the particles suspended enhances mass and heat transfer between the crystal particles and the liquid, accelerating crystallization. Therefore special attention has to be given to the geometry of the scraper. The geometry of the scraper is responsible for the flow and the degree of turbulence close to the heat exchanger surface. The removal of the fluid boundary layer on the heat exchanger and mixing with the nearest bulk fluid enhances the heat transfer of the process.

In some crystallizer designs the scrapers are responsible for the temperature and particle distributions of the whole crystallizer. The scraper geometry not only plays a role in the flow but also in the crystal layer removal efficiency. Once the particles are removed from the heat exchanger surface the geometry should allow the particles to leave the surface. After they leave the surface the forces experienced by the particles should in principle bring them to the bulk solution where after a sufficient residence time they grow to the required crystal size. Therefore the dynamics of crystals on the scraping surface area are relevant to avoid unwanted problems such as agglomeration, reseeding effects, insulated areas and inhomogeneous particle distributions in future designs. During years of research in Eutectic Freeze Crystallization several Scraped Heat Exchanger Crystallizers have been developed and studied [**73, 74, 75, 76**]. Apart from the development of heat exchangers, crystallizer (and the rest of equipment) designs such as different scraper geometries, materials and ways to apply the necessary forces have been studied. In this chapter the experimental and the numerical study of particle dynamics on one of these scraper geometries is presented and compared. During crystallization, visualization of particles and fluid flow is extremely difficult. Alongside experiments and theoretical considerations, numerical modelling is a way to investigate these issues and predict the behavior of new scraper and crystallizer designs. The experimental and computational studies focused on the start-up behavior of the flow-particle dynamics of the scraping area, when the flow-particle conditions get more or less stable. In section 10.3, the experimental test rig is shown. In section 10.4 the computer program and the computational techniques used are presented. In section 10.5, experimental and numerical results are then reported while conclusions are given in section 10.5.3. The mathematical approach applies viscoelastic models to non-reactive isothermal particles to model collisions. Such modeling was implemented and carried on the P^3 code.

The final goal of this work is threefold:

(1) to test the capability of linear viscoelastic models to describe particle clustering and sedimentation in high turbulent flows
(2) to investigate the use of particle to particle interaction in CFD data post-processing. The *"three-way"* particle-fluid coupling, section 3 is applied
(3) to point out the limits of such a computational strategy, in view of possible application to ice adhesion and removal. However, unlike salt crystals, ice requires a non-linear viscoelastic approach [**3, 13**], which certainly implies further studies on this matter.

In short, a qualitative particle-fluid dynamics study in the scraping area of a Scraped Heat Exchangers Crystallizer is presented in this chapter. Visualizations of the flow and the particle trajectories in the scraper area have been computationally and experimentally investigated. Numerical simulation have been carried out with the joint use of a commercial CFD code and the in-house Lagrangian particle tracking code P^3 presented in this dissertation. The computational strategy used combines the CFD Large Eddy Simulation (LES) with particle dynamics, overlapping the dispersed solid phase, with particle-particle interaction, on the flow phase background previously LES calculated. Particle-particle interaction on a fluid phase background, nicknamed three-way particle-fluid coupling 3, was applied. The numerical strategy developed as well as the experimental facility and the results are presented. Numerical results substantially compare to the experiment.

10.3. Experimental Techniques

10.3.1. Apparatus and Particle visualization.

To apply (linear/non-linear) viscoelastic models to mimic ice slurring and scaling behaviour, a lab scale scraper heat exchanger crystallizer, specifically designed for ice scaling investigations, was selected. The crystallizer setup consists of a cylindrical $10 - liter$ transparent Plexiglas tank of $30\,cm$ height and $20\,cm$ diameter. In the middle of

the tank a vertical shaft is connected to a rotor. Halfway the shaft, a turbine mixer is installed to keep the slurry homogeneously mixed. The crystallizer has a 1 mm stainless steel bottom plate with a heat transfer area of 0.031 m^2, which is scraped by four rotating Teflon scraper blades of 95 mm length driven by the vertical shaft (see Fig.10.3.1a). The scraper geometry was specially designed for ice scaling experiments (see Fig.10.3.1b) and tested at first with inert particles (salt crystals). The shape is a vertical wall ending in a sharp tip and fixed by a top holder. Between the holder and the scraper a normal force to the heat exchanger plate is applied by springs or air pressure balloons. A similar kind of scrapers is commonly used in different types of crystallizers and industrial machinery.

For particle visualization, $MgSO_4 - 7H_2O$ crystals were used as particles in a saturated $MgSO_4$ aqueous solution. The density of the crystals is 1680 kg/m^3 whereas their size varies from 0.5 to 2 mm, to simulate a situation similar to crystallization. The particles were released at the bottom of the crystallizer and scraped off from there before mixing with the bulk solution. Camera pictures and movies recorded this process with the rotating camera synchronized with the scraper, as shown in Fig.10.3.2. Scraper operation was recorded during rotation at 75 rpm by a digital Cannon IS Powershot camera attached to the shaft rotating at the same speed. In this way it is possible to see the flow from the reference frame of the scraper. Correct light intensity was ensured by illuminating the tank with a light projector. Furthermore, to prevent undesired light reflections, two cross polarizers were placed in front of the camera and the light projector (Fig.10.3.2).

10.4. Computational Strategy

10.4.1. Overview on the Algorithm.

Salt crystals are modelled as particles using the discrete elements (DEM modelling [**78**]) approach. Due to the generic grid reconstruction algorithm presented in this dissertation, see section 1.2, for polyhedral $P1$ elements, the P^3 computer program can elaborate LES CFD data.

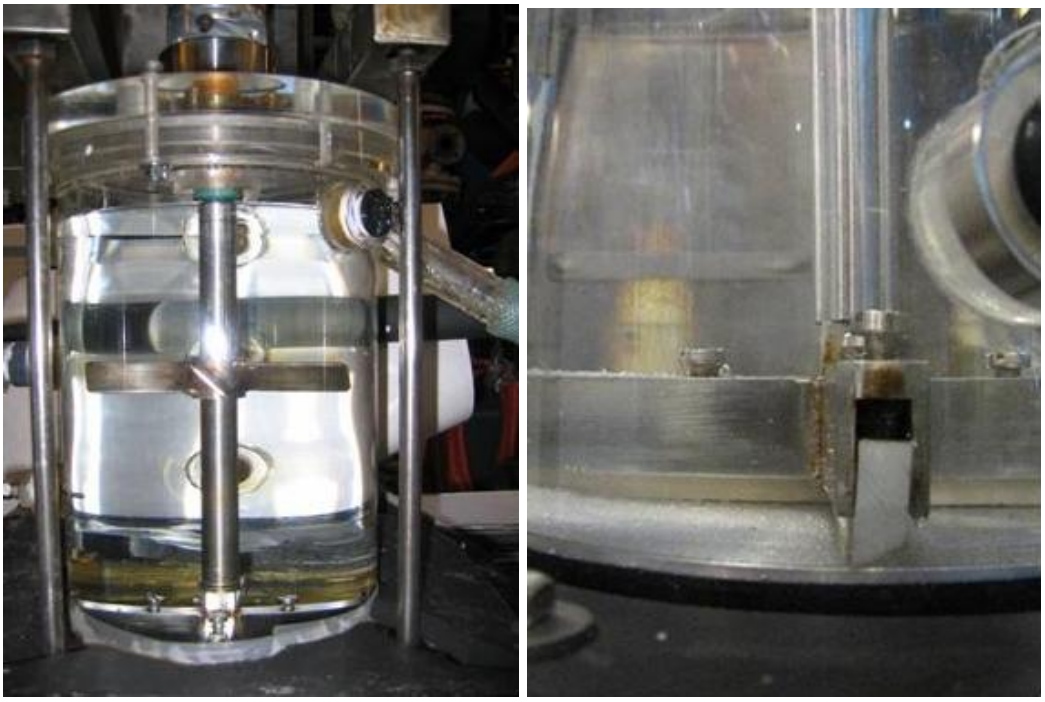

(a) (b)

FIGURE 10.3.1. Ice Scaling Crystallizer setup.

Even though, a post-processing approach could only be applied to locally dispersed secondary solid phases (low particle concentration), it may successfully model also locally high concentration cases if particle inertia represents the main driving force. In such cases, particle motion is locally not influenced by the motion of the other particles, unless by direct collisions, and, by using a more rigorous definition, particles happen to have a long relaxation time, hence a particle Stokes number $\gg 1$. In the case of high spin velocity stirring scrapers, particles are mainly driven by inertia, impacting on rotating surfaces and colliding with each other, eventually even agglomerating in low velocity recirculation zones. In such cases, particles are mainly driven by inertia and the fluid is kept in continuous motion by the rotating parts of the facility. Multiphase calculation techniques, which fully couple flow and particles interaction, may result in CPU time too long (and expensive)

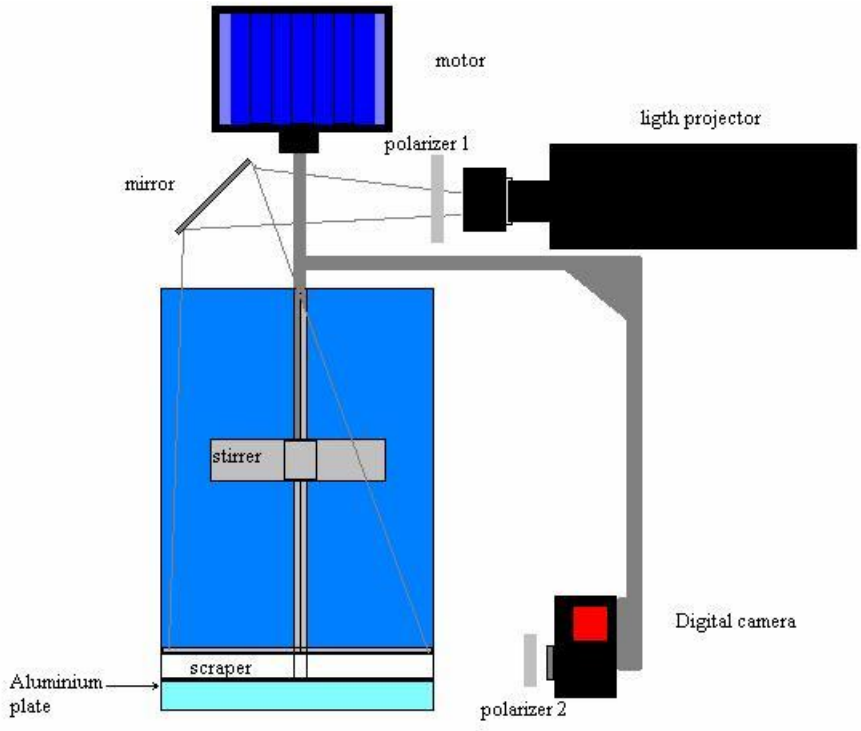

FIGURE 10.3.2. Setup for flow and particle visualizations.

and are not easly implemented in a computer program. If applicable, the particle post-processing approach may combine high computational accuracy with a considerably lower CPU time compared to a fully multiphase calculation. Although in a stirred reactor the flow is usually highly turbulent with strong particle-fluid interaction, there are a few works where the post processing approach (or: one-way coupling) has been used. Among others[**79, 80, 81**], Bakker and Van den Akker[**82**] applied the one-way approach for bubble modelling in the vortex trailing of impeller's blades, which resembles the facility the authors have investigated in this work. However, the fact that particles might considerably agglomerate and therefore consistently influence the fluid dynamics represents the main substantial limit of this modelling approach and it may lead to some error in particle trajectory calculation. In general, solids with memory, better known as rheological solids[**23**], represent a possible solution to model complicate

impact/adhesion processes, like in ice fouling and adhesion cases. Such modelling implies the use of a Lagrangian (solid particles) - Eulerian (fluid phase) reference frame. That is, post-processing the CFD flow data (Eulerian) overlapping a secondary solid phase which does not consistently alter the main fluid phase, is a valid approach to test viscoelastic models which may mimic solids with memory with acceptable numerical accuracy.

The Standard Linear Solid (SLS) model of springs and viscous dashpots (see section 3.3 and Fig.10.4.1) was used in the DEM approach to mimic the particle elastic compliance as a function of time, composition and temperature. A viscoelastic model allows to calculate compliance and energy dissipated during an impact. The SLS model, introduced in Section 3.3, describs in eq.10.4.1 the Young Modulus, as reported in section 3.3. The SLS model is applied to mechanical collisions and to thermal stress to calculate the energy restitution coefficients. Since this process is isothermal, it implies using of any viscoelastic model only as far as mechanical particle impact and particle adhesion (stickiness). Particle-particle collisions are modelled as instant collisions, also known as hard-sphere modeling, therefore interaction between particles is limited to momenta exchange. The algorithm implemented to couple the unsteady CFD LES flowfield and particle motion is outlines in Section 1.2 and briefly sketched in Fig.10.4.2. The pre-processor elaborates the LES flow field data obtained from the CFD code, providing a set of flow frames for the particles to move in. When particles have moved for a time larger than the time period between the CFD flow frames (time step n), then a new flow field corresponding to the following time step $(n+1)$ is uploaded into the code.

$$Y_p = Y_1 + Y_2 \times \exp^{-\frac{t}{\eta p / Y_p}} \tag{10.4.1}$$

where Y_p, Y_1, Y_2 are respectively the Young modulus of the particle, the spring elastic constants, η the particle viscosity. The elastic constants are assumed to be $Y_1 = Y_2 = 0.5 Y_P^{(n-1)}$, where n indicates the current time step.

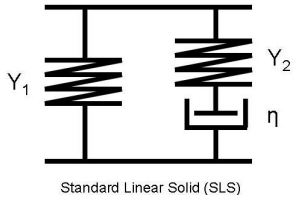

FIGURE 10.4.1. Standard Linear Solid Model (SLS), spring and spring-dash pot set in parallel.

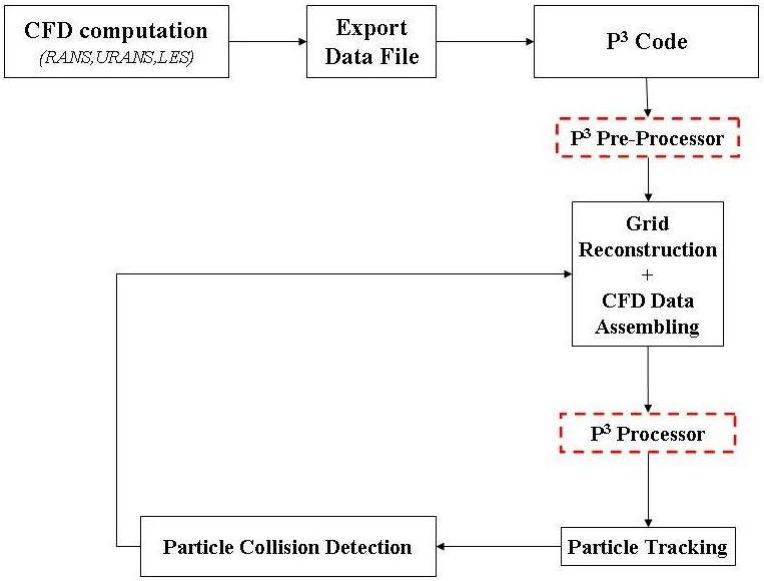

FIGURE 10.4.2. Overview of the global algorithm of the particle post-processor implemented to couple LES fluid dynamics with particle motion using the post-processing approach.

10.4.2. Calculation of the flow field.

The flow field used as background to process particle tracking was computed using the Fluent CFD code. The Large Eddy Simulation numerical approach and the Smagorinsky Sub-Grid Scale (SGS) model were applied to calculate the unsteady flow field frames. In the post-processing approach presented here, flow variables such as temperature, velocity and density are saved in separate files at each time step. A time

integration of $1\,ms$ was estimated to be suitable to capture significant turbulent flow fluctuations in the CFD LES simulation.

10.5. Results and Discussion

10.5.1. Experimental Results.

During the start up of the facility, see the pictures in Fig.10.5.1(a) and (b), there is a sort of swinging particle motion between the two blades of the scraper. This motion is due to the impulsive scraper motion which generates a pressure difference between the back-end (low pressure, driving possibly cavitation) of the upstream scraper blade and front-end (high pressure) of the downstream blade. Afterwards, salt crystals start agglomerate (Fig.10.5.1(c-d)) on the front bottom location of the downstream blade of the scraper, creating a build up of particles which is then pushed, towards the upper edge of the scraper. Eventually, some of these front-side particles cross the top side of the scraper being further dragged away from the bottom build up (Fig.10.5.1(e-h)). The rest of the particles show a fall-back motion (Fig.10.5.1(i-n)), which produces a sort of thick "cloud". Such a "cloud" indeed modifies the fluid dynamics at the bottom of the blade in such a way that the incoming particles are diverted to the top edge of the blade and then released downstream. Both the swinging and fall-back motion were not reproduced in the numerical simulation. The swinging motion was not captured because the LES flow field frames were saved assuming the facility already in rotational motion, whereas the fall-back was not completely reproduced because of the limited number of particles (limited number of collisions) and the one-way[1] coupling between the fluid and solid phase.

10.5.2. Numerical Results.

The scraper fluid dynamics was calculated with $FLUENT^{TM}$ using the Large Eddy Simulation (LES) with the standard Smagorinsky

[1]one way coupling: fluid not influenced by the particle motion

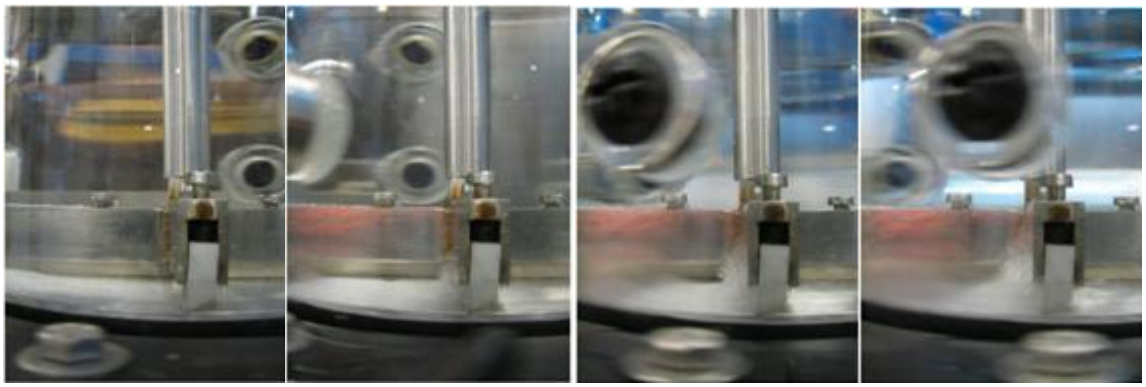

(a) 0 ms (b) 400 ms (c) 600 ms (d) 800 ms

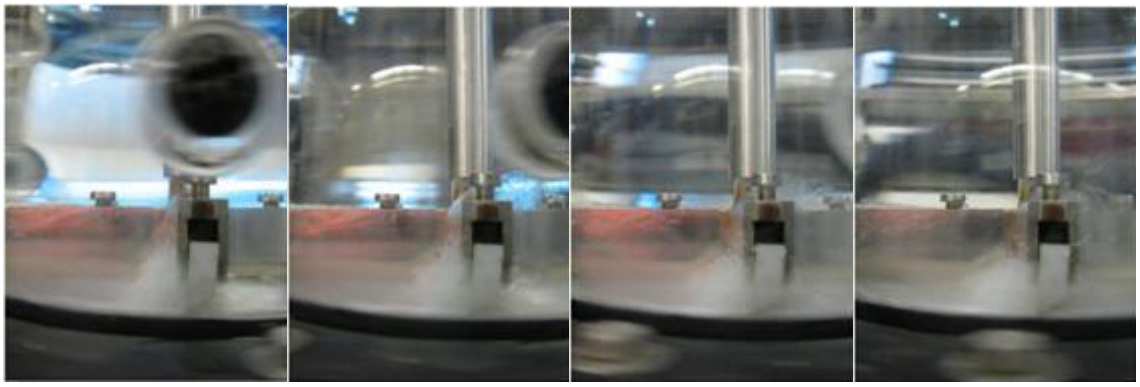

(e) 1000 ms (f) 1200 ms (g) 1400 ms (h) 1600 ms

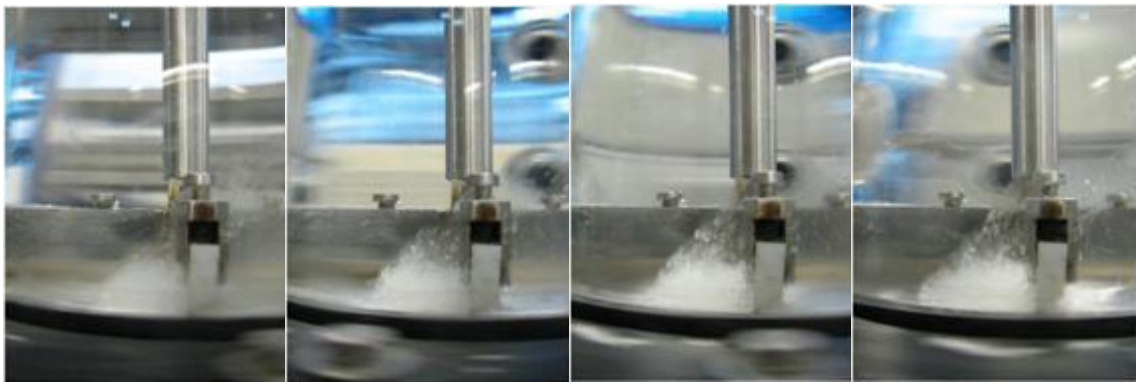

(i) 1800 ms (j) 2000 ms (k) 2200 ms (l) 2400 ms

FIGURE 10.5.1. Snapshots of the $MgSO_4 - 7H_2O$ crystal particles scraped from the heat exchanger surface during start-up behavior.

sub-grid turbulence model. The computational domain chosen is the one used for flow visualization analysis performed injecting dye (see Fig.10.3.2) which differs from the facility used for the salt scraping experiments shown in Fig.10.5.2a and Fig.10.5.2b in that the tank diameter was 4.0 cm longer. The dynamics of both the fluid and the particles were strongly affected by the gap between the scraper radial tip and the tank (see Fig.10.5.2b) which induced some particle dispersion in the radial direction. Nevertheless, this configuration seemed suitable to meet critical CFD mesh modelling requirements for moving/rotating elements as well as to verify the possibility to compare LES results to experimental results. In this work it is attempted to model particle-particle interaction by post-processing LES computations combined with the Discrete Element Model (DEM) with Viscoelastic Modelling (VEM) of solid particles and the restitution coefficients of particle-solid wall and particle-particle collisions. Although the fluid dynamics is consistently influenced by the gap between the scraper and the tank at the scraper radial tip location, the results shown in Fig.10.5.3 are qualitatively in good agreement with the experiments, and the *"three-way"* particle tracking in unsteady flowfields (LES) has proven capable of both describing the main particle dynamics and capturing critical particle behaviors occurring in multiple instantaneous collisions (hard particle model). More in details, particles accumulate at the scraper front bottom location and form a built up agglomerate which is progressively pushed to and piles up from the bottom end up to the leading edge moving along the front side of the scraper. Dragged by the main stream, particles cross the top side and the radial tip of the scraper and disperse downstream. When most part of the particles have crossed the scraper and the thickness of the pile up along the scraper front side is consistently reduced, then the remaining particles slightly lower towards the bottom of the tank (this is the so called fall-back, see Fig.10.5.1e-h and Fig.10.5.3e-h). In fact, since the total momentum of the group of particles clustered at the bottom is not sufficient to hold up the others, these fall down. Indeed, there are

some differences between the (corresponding) frames in Fig.10.5.1 and Fig.10.5.3, mainly caused by:

(1) the fact that the number of particle was lower than in the experiment (which anyhow unknown)
(2) the diameter of the geometry simulated is 4.0 cm longer (see Fig.10.5.2)
(3) particle concentration may locally not be homogeneously dispersed in the fluid phase
(4) salt crystals were represented as spheres.

The last two assumptions 3 and 4 imply that a complete particle-fluid interaction might be locally required (fully multiphase flow, four way particle-fluid coupling) and that the shape of a salt crystal agglomeration may strongly differ from an agglomeration of the same amount of sphere particles as a result of a substantial different aerodynamic drag and friction force acting on the particles. The joint effect of the four causes mentioned prevented the simulation to correctly mimic the particle fall-back behavior.

10.5.3. Conclusion.

Particle-flow simulations show good agreement with the particle-flow visualization experiments. To better describe the particle built up process, particle-particle collisions was modelled. This fact prevented results from being unrealistic in terms of particle build up at front end of the scraper. In this work it was attempted to model particle-particle interaction by means of post-processing LES data computed in $FLUENT^{TM}$ combining the Discrete Element Model (DEM) with Viscoelastic Modelling (VEM) of solid particles to calculate the restitution coefficients of particle-sold wall and particle-particle collisions, see Table 1. A fully multiphase approach (four way fluid-particle coupling) may be locally required as the liquid flow is inevitably altered by the presence of neighbour particles, especially near the particle built up. Although further work is still required and despite the fact that the

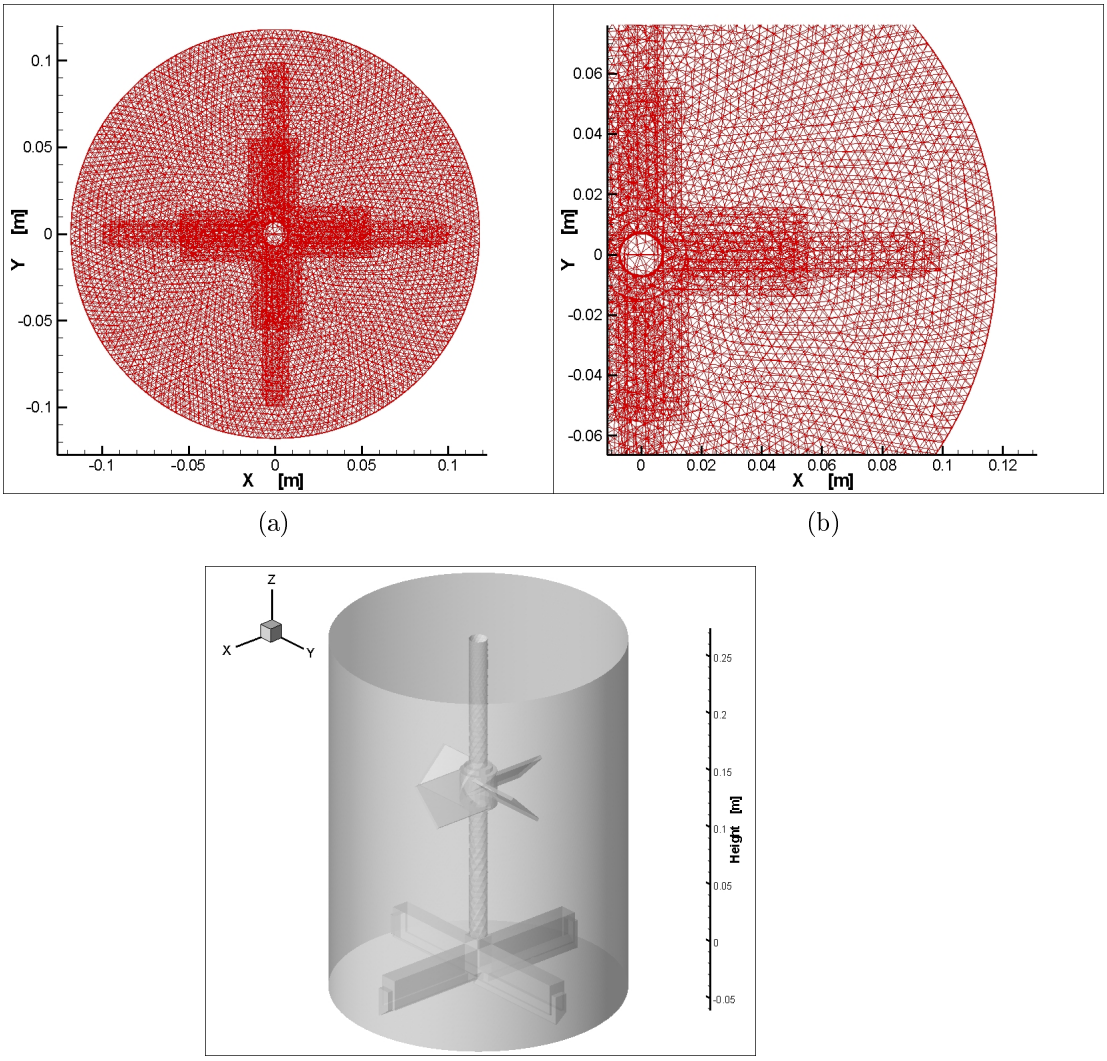

FIGURE 10.5.2. a) Computational domain. 897996 cells, 170125 nodes. b) gap between the scraper and the tank. c) complete overview on the simulated facility.

CFD particle post-processing strategy (three way fluid-particle coupling) showed some constraints in modelling such unsteady particle dynamics, the results presented here provide a good insight into the behavior of the particles and fluid motion. The (linear) viscoelastic

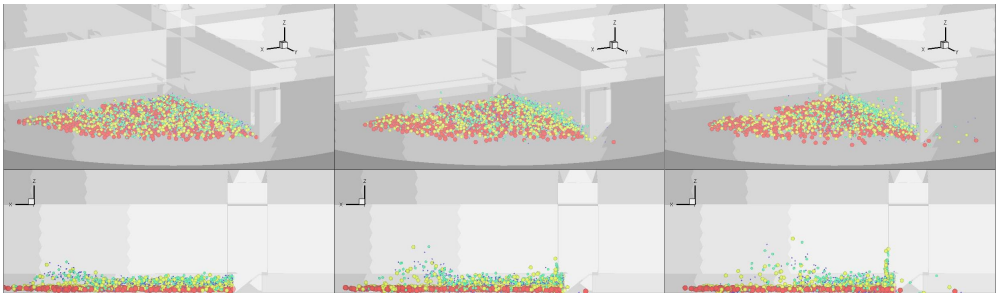

(a) 200 ms (b) 400 ms (c) 600 ms

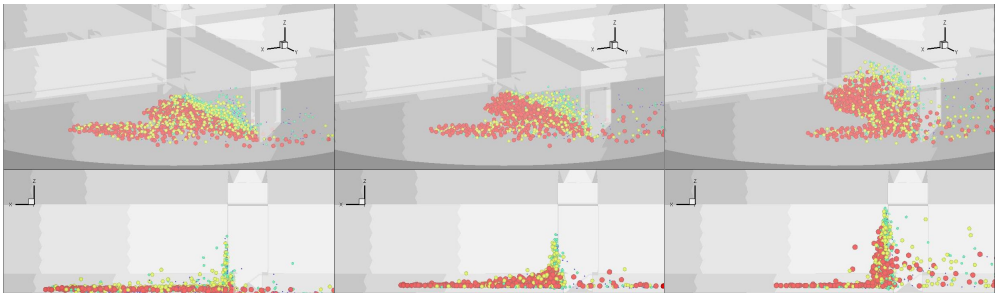

(d) 800 ms (e) 1000 ms (f) 1200 ms

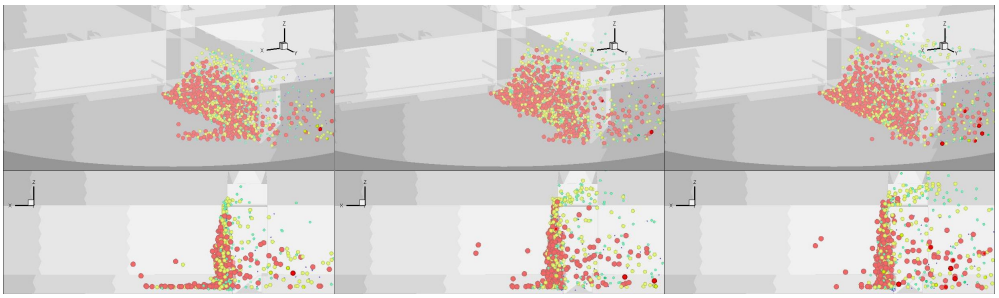

(g) 1400 ms (h) 1600 ms (i) 1800 ms

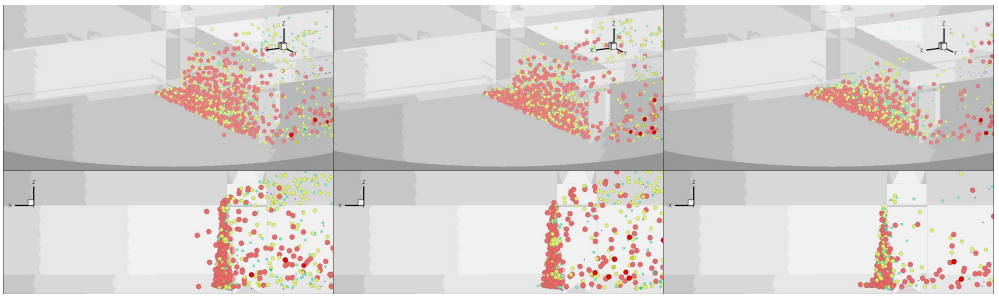

(j) 2000 ms (k) 2200 ms (l) 2400 ms

FIGURE 10.5.3. Snapshots of the simulation on the $MgSO_4 - 7H_2O$ crystal particles. 2000 Particles. Diameters: 0.5, 1.0, 1.5 and 2.0 mm. Animation available either on internet at [Weblink Salt Scraper].

CFD	$Particle\ Tracking$	$No.Particles$	VEM
LES	$Unsteady$	2000	SLS

TABLE 1. Scraper Summary Table

approach was applied to model the impact of non-reactive solid particles. Collisions resulted to be substantially elastic, returning tangential and normal restitution coefficients close to 1. The computational strategy and the results obtained actually represent a preliminary computational test prior to implementation of this (nonlinear) viscoelastic behaviour to ice built up in crystallization processes in time and temperature dependent cases. Although including Coriolis, Saffman and Magnus forces may indeed improve both particle dynamics modelling and accuracy of the results, their modelling is considered not relevant for the qualitative study presented here.

Part 4

Biomedical Applications

CHAPTER 11

Extrathoracic Idealized Mouth and Throat Model

"Be careful about reading health books.

You may die of a misprint..."

- Mark Twain

11.1. Introduction

This chapter presents the results on aerosol tracking and deposition in an idealized mouth-throat model. The intrinsically versatile P^3 algorithm allows many applications to those field where particle deposition occurs due to mechanical dynamics. With several limitations, it is possible to extend the validity of the mechanical deposition even to cases where the thickening or the growth of bluff obstructions depends upon absorption and species concentration. This is the case of the application to hemodynamics, briefly described in the following Chapter .

In the field of numerical and experimental studies of aerosol deposition, Matida et al.[**27**] applied the particle post-processing on the flow field solution obtained using $\kappa - \omega$ turbulence model with Kato and Launder modification. The $\kappa - \omega$ model was chosen as suggested in [**27**] where it demostrated that the standard $\kappa - \varepsilon$ model overpredicts deposition for "turbulent" particle tracking compared to the $\kappa - \omega$ model. A user-defined Fortran code was implemented to describe the transient flow rate boundary condition at the mouth inlet. Similarities with the computer program developed and presented in this dissertation induced

the author to attempt to apply in a straightforward manner what already validated for combustion cases. The following assumptions have been made:

(1) Droplets coalescence neglected
(2) five class size particles only: 2, 5, 10, 15 and 20 μm
(3) 30 l/min as inlet air mass rate, for RANS and LES simulation
(4) mesh: 453594 cells, computational domain volume: $9.436207 \times 10^{-05}\ m^3$
(5) near wall turbulence fluctuation applied only at boundary cells for $y^+ < 80$
(6) to simulate liquid dropelets, the Young modulus was assumed 1 Pa

A brief description of the idealized model proposed is sketched in Fig.11.1.1. The Simulated domain is introduced in Fig. 11.1.2. The mesh resolution selected is consistent with the one chosen by Jayarajua et al. [**83**] which was 550000, for a similar computational volume. Although the mesh adopted in this work is 100000 cells lower in number compared to the Jayarajua model, it was estimated sufficient to capture vortex motion and fluid dynamic fluctuactions which may affect aerosol particle motion.

The numerical simulations presented here do not represent any specific experiment reported in literature. Previous works presented a wide range of geometries, airflows and particle distributions. The main aim of the work presented here is to demonstrate the direct applicability and versatile of the numerical strategy that structures the P^3algorithm. The 30 l/min airflow and the particle sizes were chosen as the most representative of an adult person and the aerosol performance of the most common aerosol devices currently in use.

Furthermore, the geometry used for numerical simulation differs from the one proposed by Johnstone et al. [**84**] in some details.

(1) the epiglottis and larinx-thrachea connection have a different shape (compare to Johnstone's model)

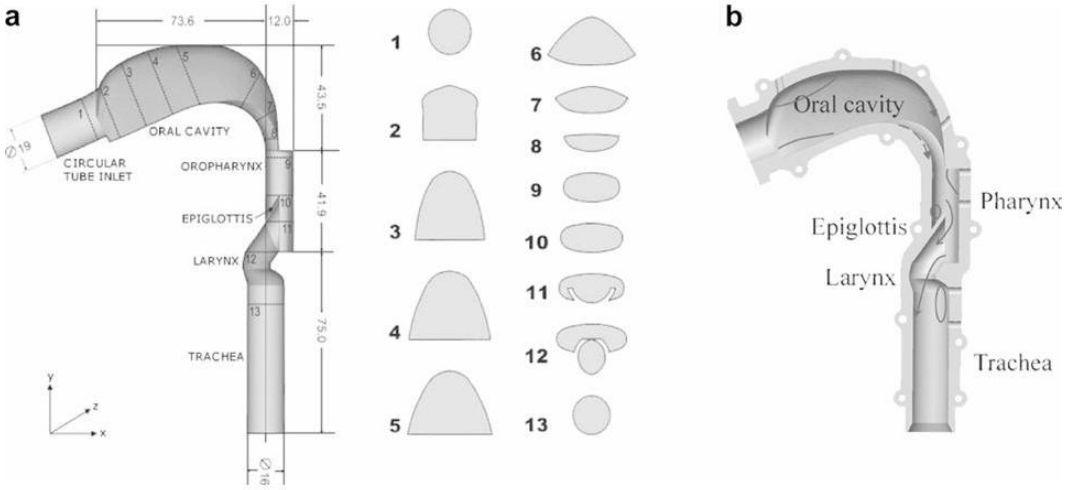

FIGURE 11.1.1. Sketch of the idealized mouth and throat taken from[**27**]

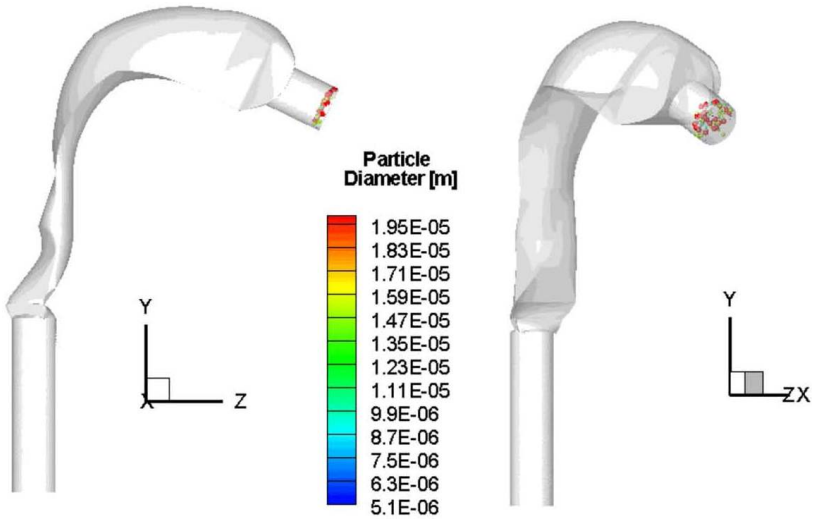

FIGURE 11.1.2. Sketch of the simulated idealized mouth and throat with particles at the mouth inlet.

(2) boundary surface curvatures between the cross sections reported in Fig. 11.1.1 were not given. Therefore the oral cavity differse original model in representing the sides of the human mouth.

(3) Experimental and numerical results of previous works are not directly comparable since they refer to different geometries

However, numerical results show a good agreement with the patterns reported in litterature, in both the numerical [**85, 83**] and experimental [**70, 67**] field.

11.2. Motivations and Historical Background

The respiratory system is used as a route for medical treatments for a variety of respiratory diseases by way of inhaled aerosols. Many different devices are at present used for respiratory drug delivery. In order for inhalation to be effective, the inhaled aerosol should reach the targeted area, i.e. the lungs, as in the sketch shown in Fig.11.2.1. In this regard, the extrathoracic region can greatly affect respiratory drug delivery, since it acts as a filter proximal to the lungs. For this reason, understanding of flow dynamics and deposition of inhaled aerosols in the extrathoracic region is important in designing effective inhalation devices. However, such an understanding is complicated by morphological variation among different individuals as well as time/flow rate dependency of respiratory system geometry. Initial work with the idealized model used here was performed by De Hann and Finlay [**68, 85**] who examined the effect of several inhalation devices on total deposition monodispersed aerosols. Works performed on measurements by Hennan [**67**] and Grgic [**70**] who performed also modeling in [**69**] as Matida[**27**] aimed to better understand the phenomena involved and the critical numerical parameter representative of the aerosol deposition process. Experimental results on the 30 l/min airflow are shown in Table **??**.

11.3. RANS Simulation

RANS simulation performed at 30 l/min showed unsteady behaviour, see Fig.11.4. The unsteady fluid dynamics was investigated by the LES simulation, presented in Section 11.4. The P^3 software used in this work was not developed to upload the y^+node values from the CFD: $y^+$was instead calculated in the code only at the boundary cells. Such a limitation prevented the author to correctly apply the fluctuation formulas presented in Section 1.5, to take into account the

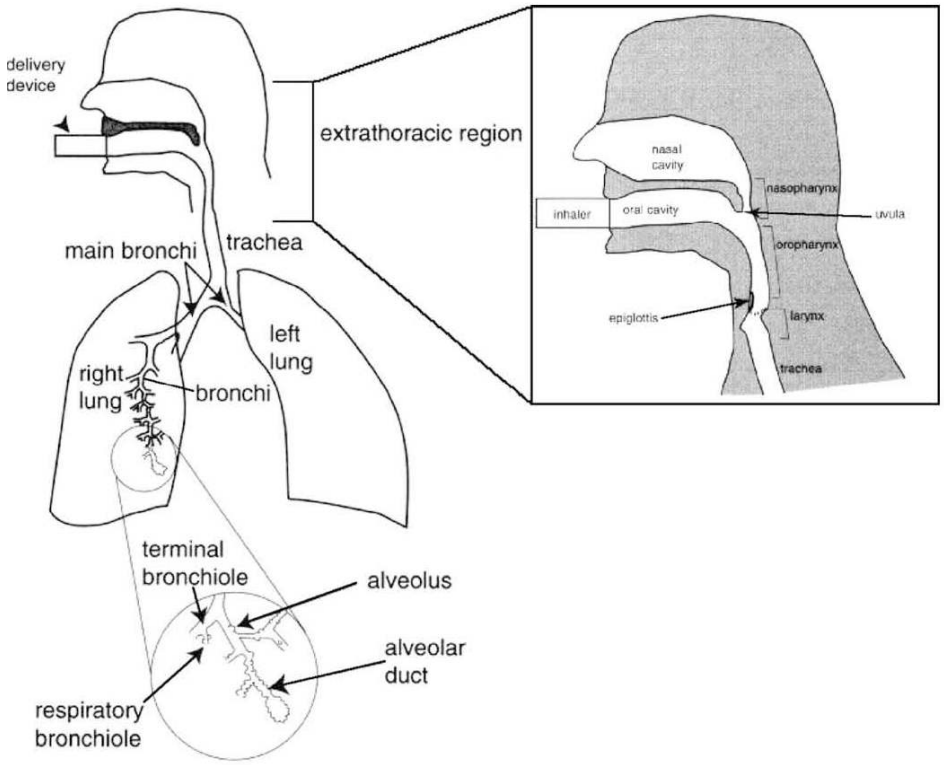

FIGURE 11.2.1. Detail of the part modelled in this work. Source [**84**].

boundary effect for $y^+ < 80$. Although, the RANS simulation provided $y^+ < 10$, the aerosol tracking investigation showed promising results consistent with the other experimental data reported in literature.

11.3.1. Steady Particle Tracking.

Statistics obtained by steady particle tracking on RANS are illustrated in Fig.11.3.2. Results are substantially in agreement with those published by Matida et al.[**27**]. The main disagreement is in the particle deposit location: in [**27**] particles deposit along the oral cavity and the oropharinx while in the numerical simulation presented here, particles deposit only along the orophaynx. This fact may be addressed to the different mesh resolution, slightly different geometry (especially the larinx and epiglottis intersection) and the fluctuation correction

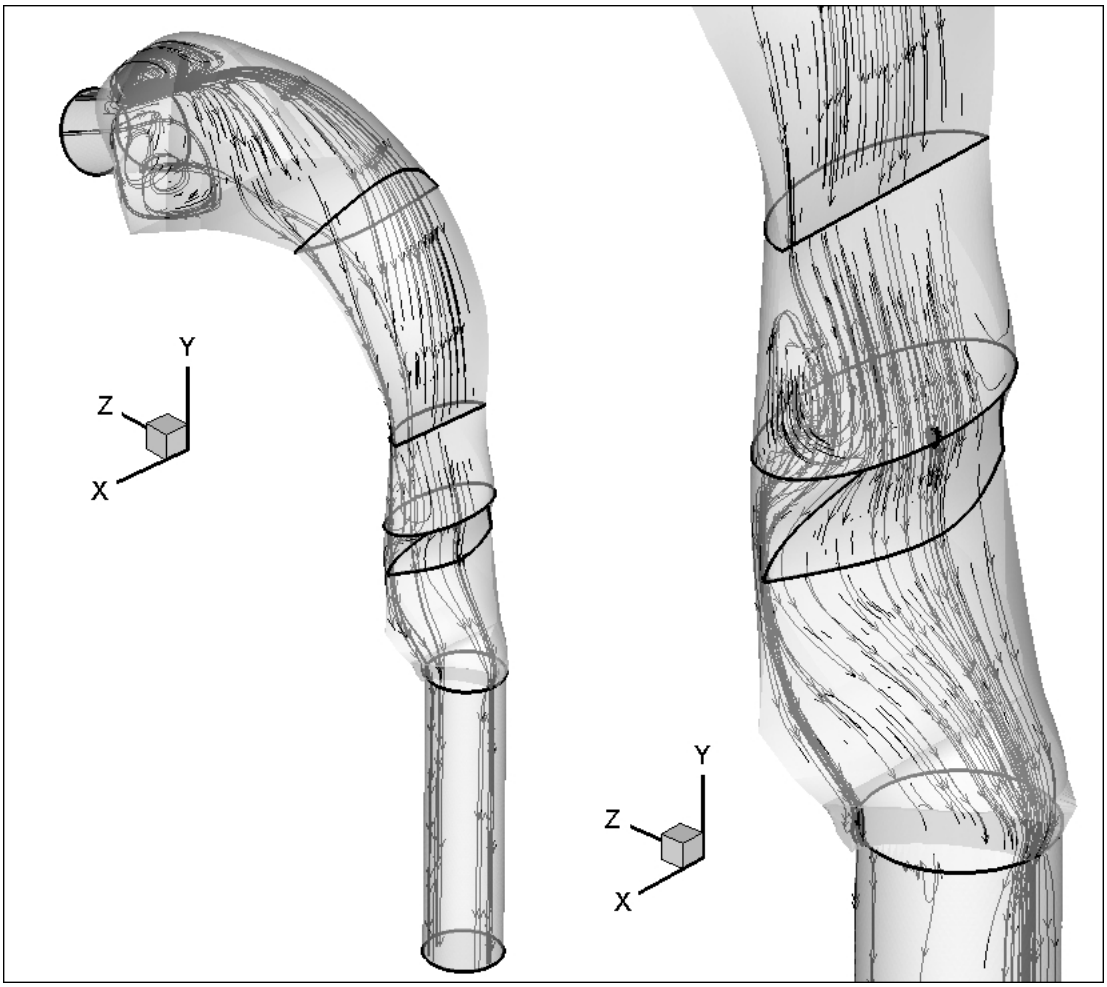

FIGURE 11.3.1. Streamlines detail of the idealized model in the RANS simulation.

applied for $y^+ < 80$. As already mentioned above, such a correction in the P^3 code was only applied at the boundary cells. However, particle deposition appear more distributed in the unsteady particle tracking both in the RANS and LES CFD calculations.

11.3.2. Unsteady Particle Tracking.

The unsteady particle tracking was performed using $5 \cdot 10^{-5}$ s as particle integration time step. This time step was about one order of magnitude lower than the average time step required by a 10 μm

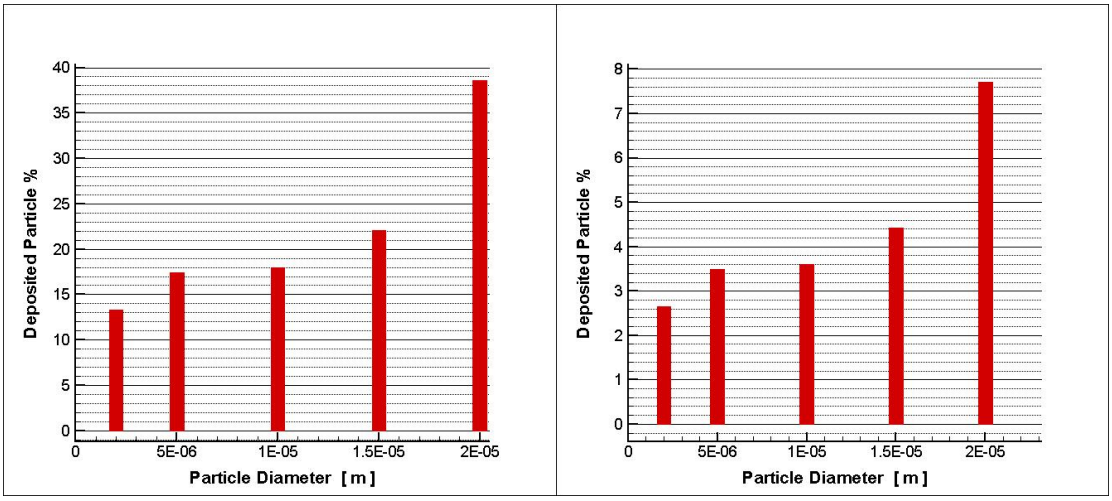

(a) deposited percentage per each class size (b) deposited percentage on the total injected

FIGURE 11.3.2. Aerosol Statistics

to cross a non-boundary host cell[1]. This fact implied that a particle needed from 5 up to 10 time steps to cross its own host cell. That is, particles appeared more diffused than in the steady particle tracking, see Fig. 11.3.4. The total time investigated was 1.8 s. Deposition occurs along the oral cavity, the oropharinx and at the intersection with the epiglottis. Such a result is indeed more consistent with the results presented in [**27**].

11.4. LES Simulations

The LES simulation was performed with a CFD integration time step $5 \cdot 10^{-4}$ s while the particle integration time step was $2.5 \cdot 10^{-5}$ s. The total time investigated was 1.78 s. The unsteady fluid dynamics captured is shown in four snapshots in Fig. 11.4.1. Concerning the particle tracking, Fig. 11.4.3 and 11.4.4 show from different prospective particle diffusion. Particle deposition is spread on both sides of the oral cavity and along the oropharinx, see Fig. 11.4.5. This result is closer to the experiments reported in [**69**] and the numerical results in [**27**]. As

[1]The mesh resolution at the boundaries was increased. Therefore, the volume and hence the mean cell dimention to be crossed by a particle was consistently reduced.

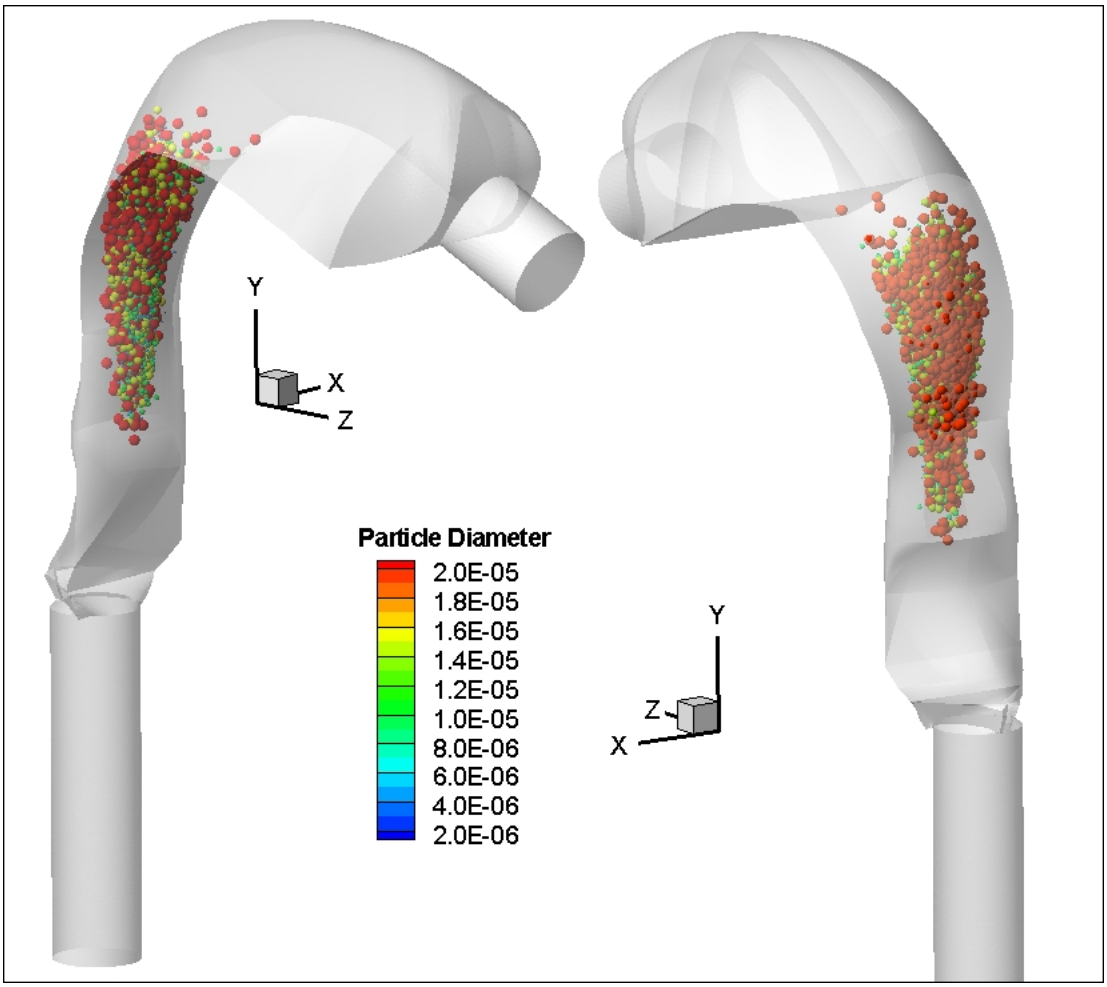

FIGURE 11.3.3. Aerosol RANS Deposit Location

reported in Section 1.5, LES performed at low time step may reduce the numerical error introduced by neglecting turbulence modeling at the sub-grid scale level. This fact caused the particle tracking performed on LES to be closer to the experiments in particle deposit location. Particle deposit statistics are reported in Fig. 11.4.6: 20 μm particles deposit mostly in the oral cavity and along the oropharinx while 2 μm particles deposit along the trachea. Since the simulation was neither taken to the end (no particle injected any longer) nor performed for a time period sufficient to achieve a steady deposition rate result, see Section 7.4 in Fig. 7.4.4, the reported statistics are meant to be

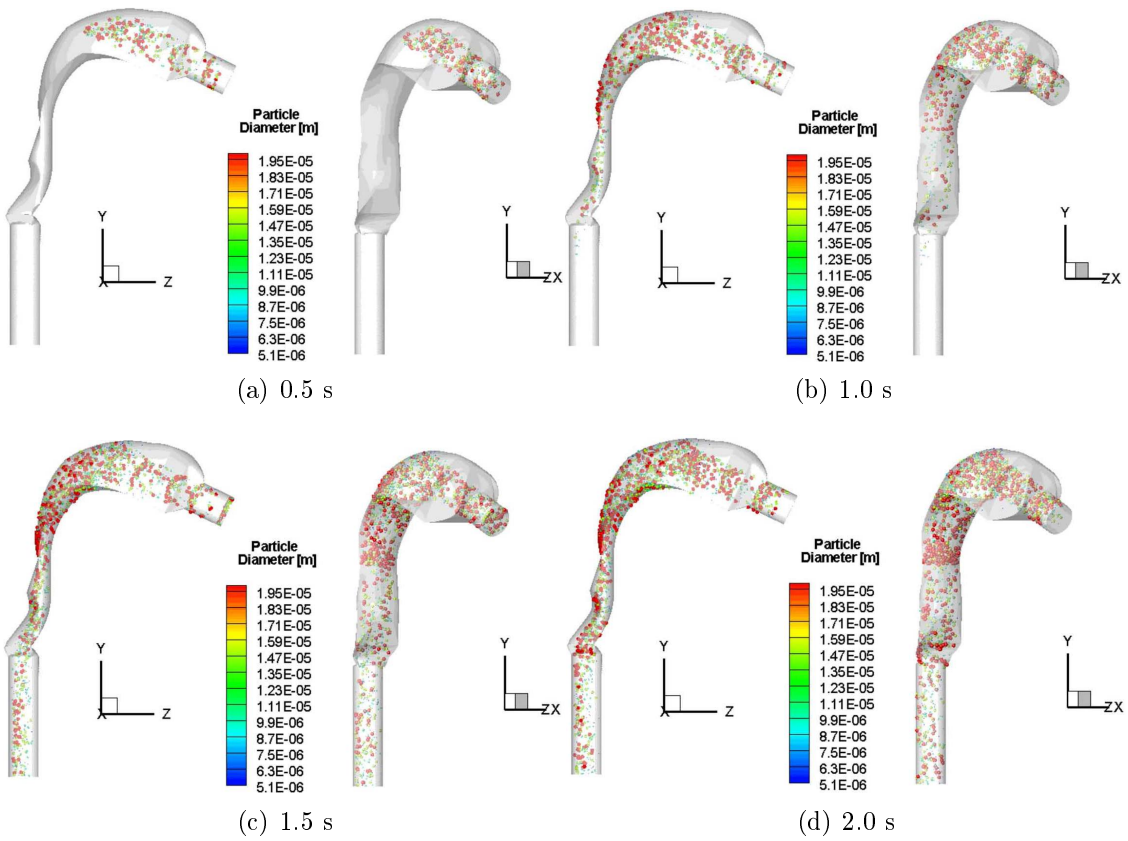

(a) 0.5 s (b) 1.0 s

(c) 1.5 s (d) 2.0 s

FIGURE 11.3.4. Aerosol Deposition RANS, unsteady particle tracking. Four snapshots.

considered only to show the tendency of particle deposition behaviour. Numerical results on LES streamlines visualization in Fig. 11.4.1 fairly compare to the experimental instantaneous flow snapshots, shown in Fig. 11.4.2, reported by Johnstone et al. [**84**] for the 30 l/min airflow: the vortex release and periodic formation at the mouth inlet is fairly well captured whereas the vorteces at the side of the mouth are not. The main reason may lie in the bottom and the side oral cavity curvatures, which, as mentioned at the begining of this chapter, differ from the original geometry. In Fig. and 11.4.1 the two vorteces at the top and bottom of the oral cavity are clearly shown. Indeed, the shape of the larinx and the epiglottis may influence the fluid dynamics and the vortex formation within the oral cavity.

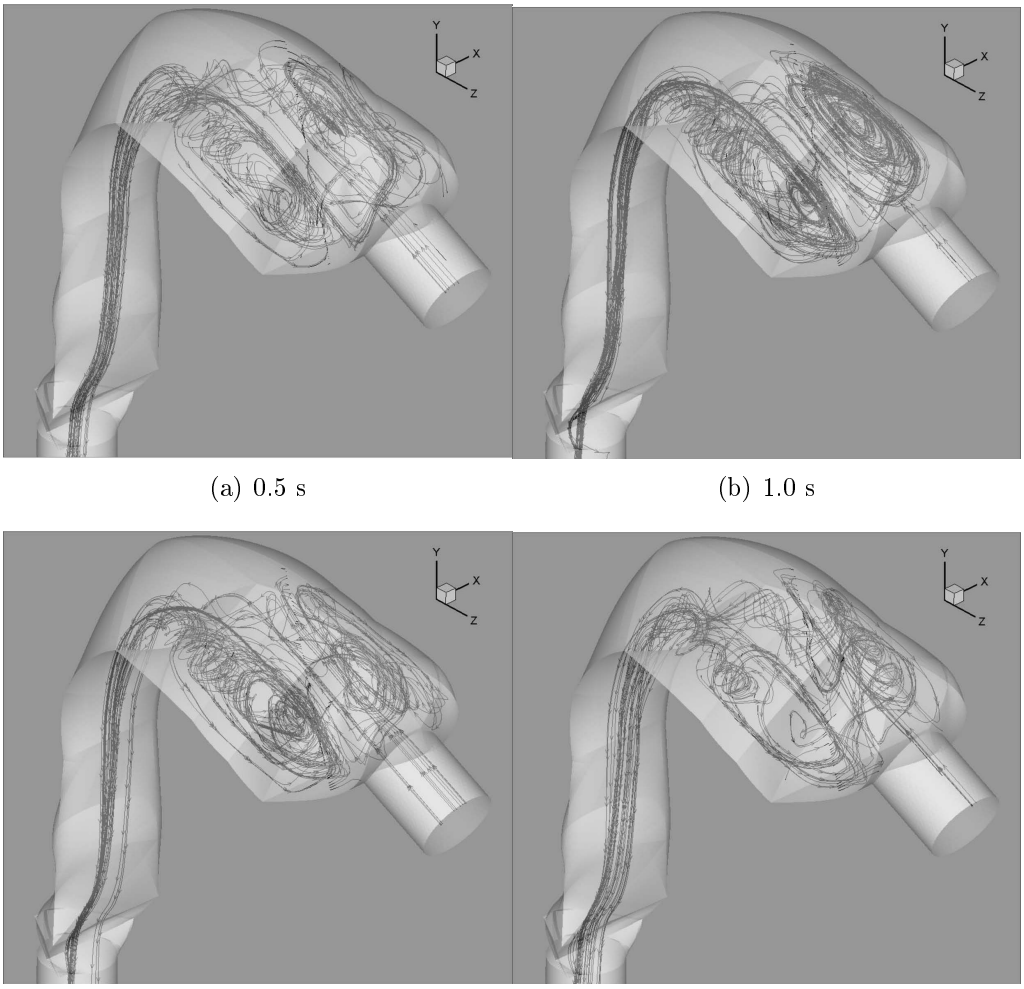

(a) 0.5 s (b) 1.0 s

(c) 1.25 s (d) 1.8 s

FIGURE 11.4.1. Aerosol LES streamline snapshots

Animation of the CFD LES simulation is available at [Weblink Aerosol LES Streamlines], while the unsteady particle tracking performed on the LES flowfields are available at [Weblink Aerosol LES 1st Movie] and [Weblink Aerosol LES 2nd Movie].

11.5. Conclusions

In this Chapter LES flowfields were coupled with unsteady particle tracking to simulate aerosol dispersion inhaled during medical treatments. Results are in good agreement with experiments and numerical

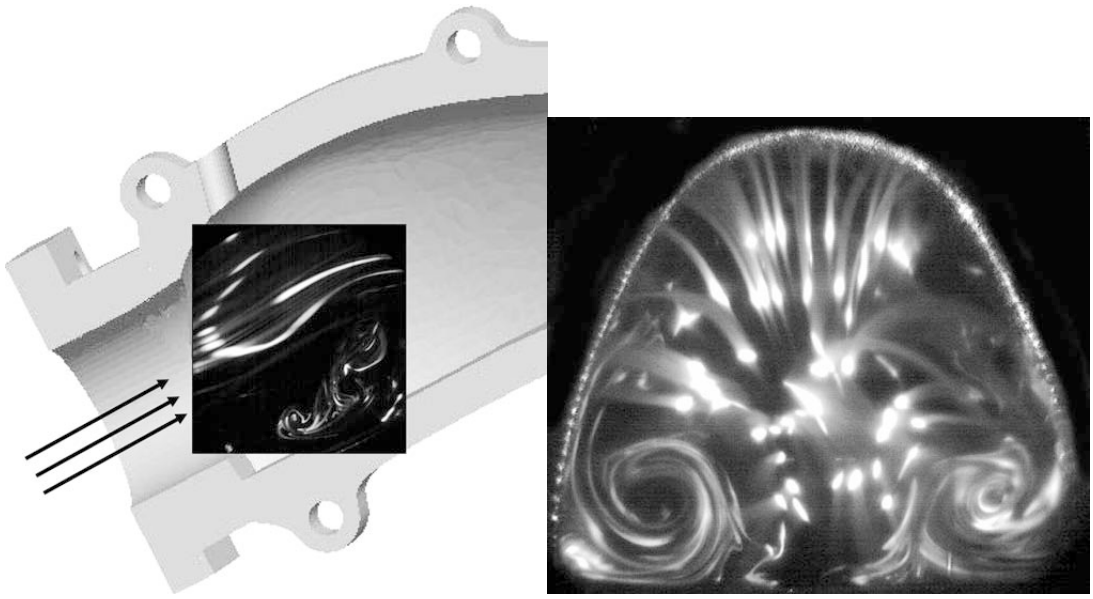

(a) mouth inlet (b) cross section at the end of oral cavity

FIGURE 11.4.2. Instantaneous Flow visualization, 30l/min. Pictures taken from Johnstone et al. [**84**]

results in literature. The final goal was twofold: i) to test the versatile P^3capability of tracking particles on LES flowfields, ii) to compare results obtained on RANS and LES simulations performing steady and unsteady particle tracking. Results show that particle dispersion is affected by turbulence fluctuactions due to boundaries ($y^+ < 80$). The error introduced by applying such a turbulence correction only in boundary cells is reduced by performing unsteady particle tracking on RANS or, better, on LES. The simulation performed on LES provided the dispersion closest to the literature results due to the fact that in LES no turbulence model is applied as in RANS. Furthermore, the error introduced by neglecting sub-grid scale turbulence modeling on particles may be reduced by reducing the LES integration time step which implies to reduce the particle integration time step which must be always lower than the one used in the CFD calculation. See Table 1 for a short summary of the simulation presented.

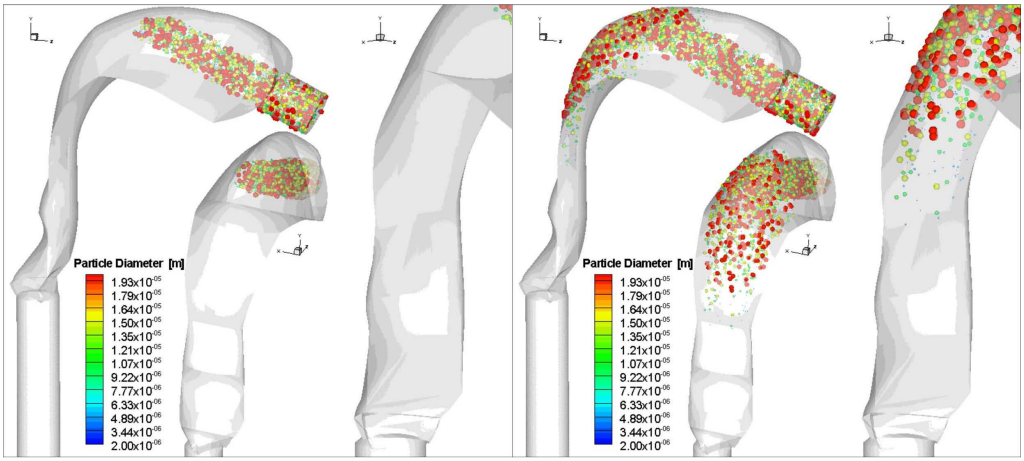

(a) 0.5 s (b) 0.95 s

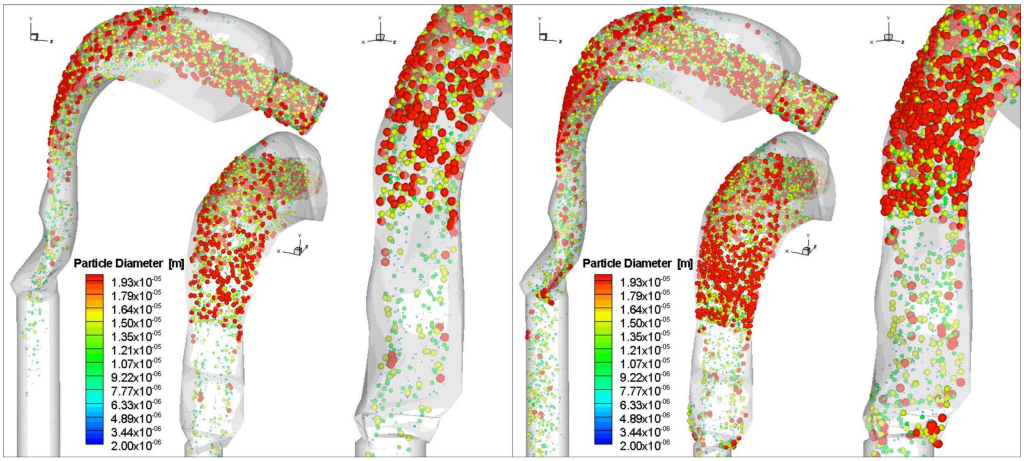

(c) 1.45 s (d) 1.8 s

FIGURE 11.4.3. Aerosol Particle, LES simulation and unsteady particle tracking, first view. Animation at [Weblink Aerosol LES 1st Movie].

CFD	*Particle Tracking*	*No.Particles*
RANS	*Steady*	6250
RANS	*Unsteady*	7000
LES	*Unsteady*	10000

TABLE 1. Aerosol Simulations Summary Table

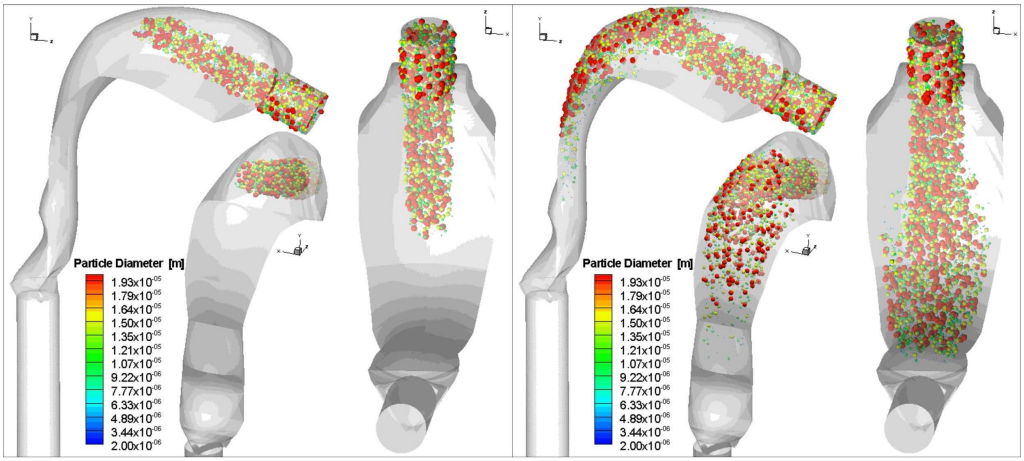

(a) 0.5 s (b) 1.05 s

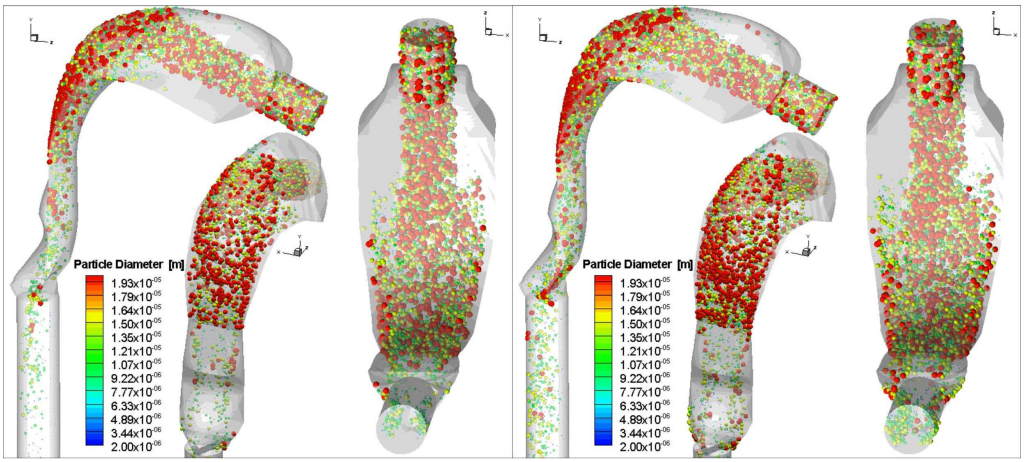

(c) 1.65 s (d) 1.8 s

FIGURE 11.4.4. Aerosol Particle, LES simulation and unsteady particle tracking, second view. Animation at [Weblink Aerosol LES 2nd Movie]

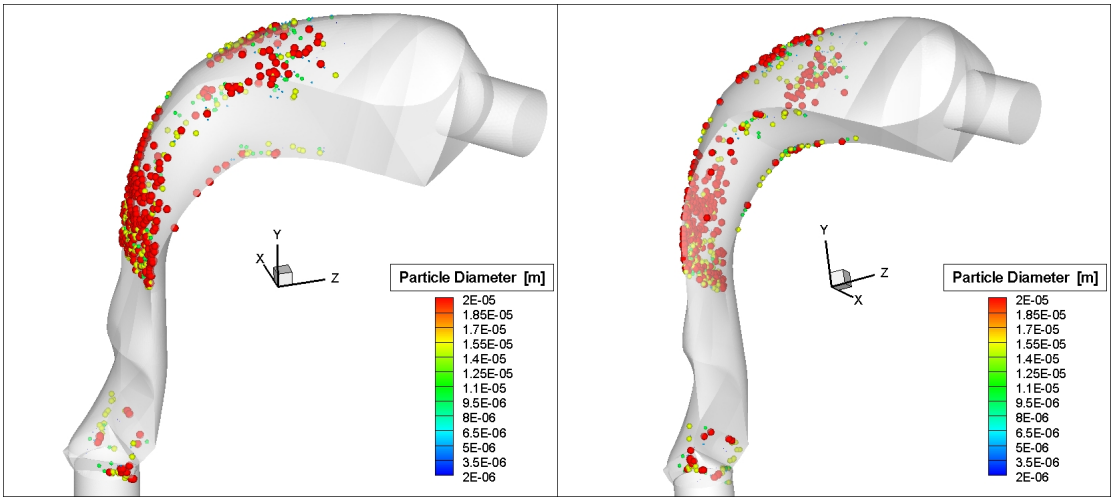

(a) (b)

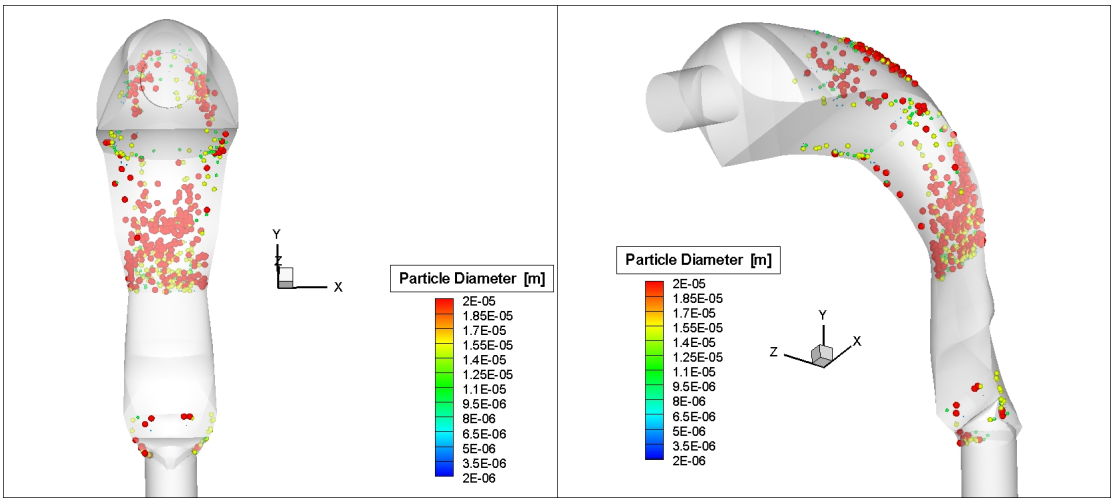

(c) (d)

FIGURE 11.4.5. LES, unsteady Particle Tracking. Deposited Particles

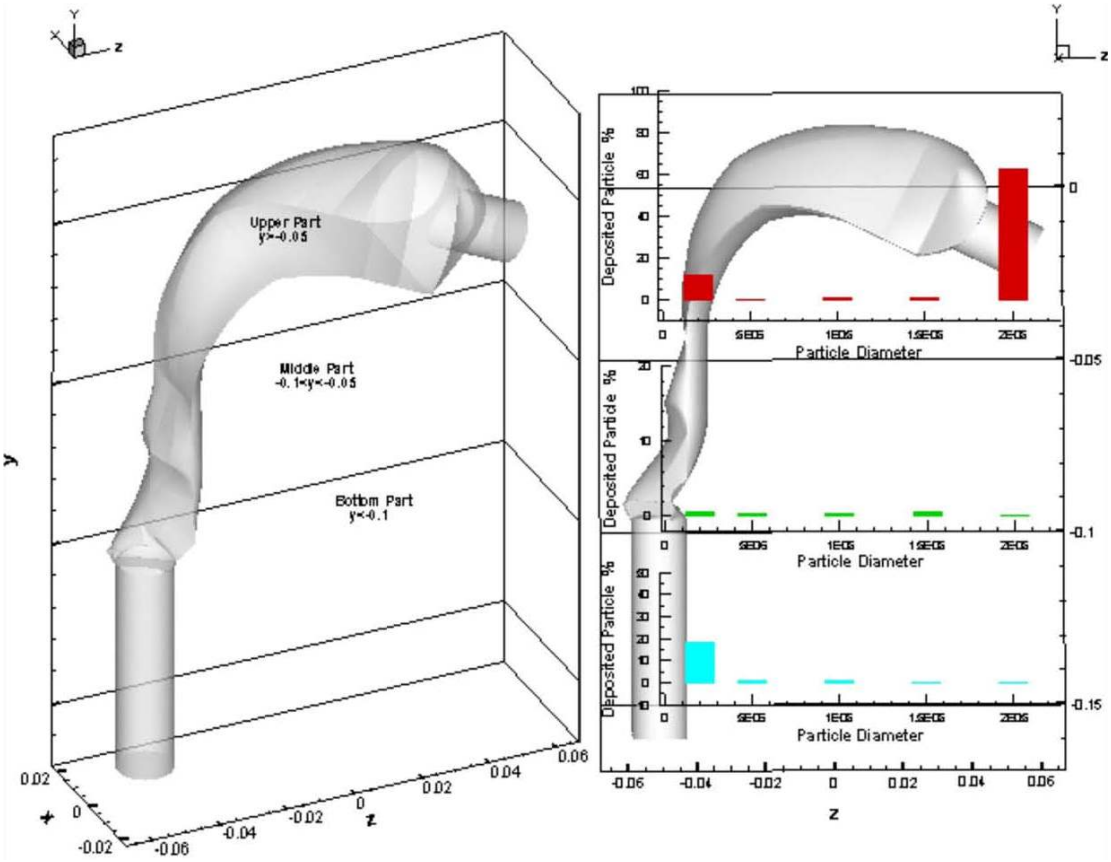

FIGURE 11.4.6. Aerosol LES Deposit Statistics

CHAPTER 12

Hemodynamics: Arteria Carotis Communis

"Life is pleasant. Death is peaceful.

It's the transition that's troublesome..."

- Isaac Asimov

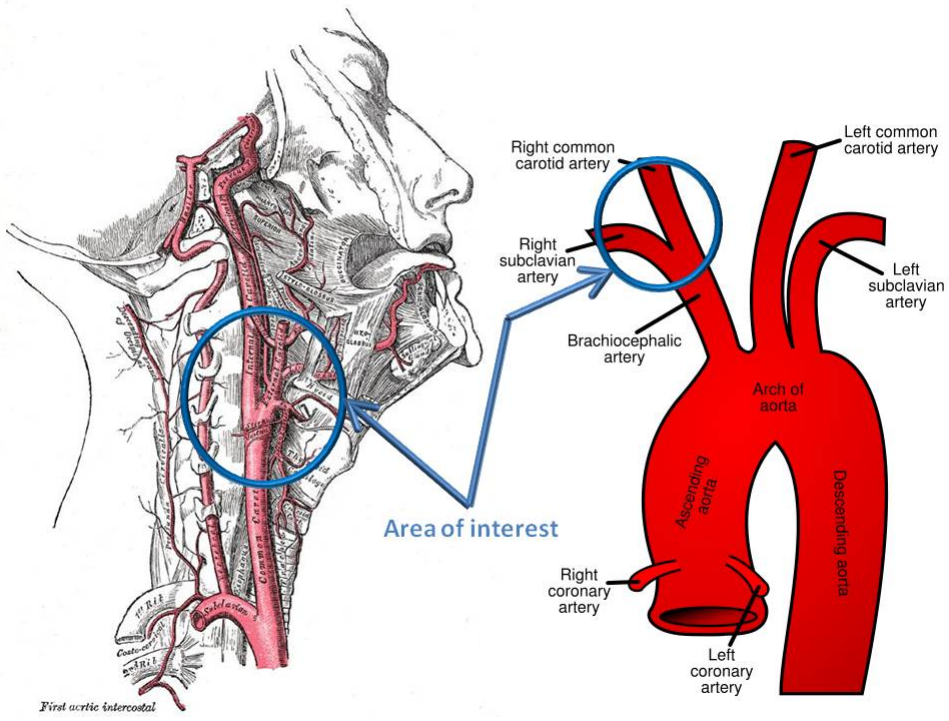

(a)

FIGURE 12.1.1. Arteria carotis communi. Sketch of the area of interest.

12.1. Introduction & Historical Background

In human anatomy, the common carotid artery is an artery that supplies the head and neck with oxygenated blood; it divides in the neck to form the external and internal carotid arteries, as shown in Fig. 12.1.1.

Because of the anatomy of the carotid, it is known to be one of the main locations where obstruction may occur. In particular at the bifurcation between the internal and external carotid, where the blood stream may become turbulent and swirl motion may occur. This fact in conjunction with high blood pressure and other health diseases are commonly considered the main cause of the genesis of atherosclerosis, heart or brain strokes. Blood is a non-Newtonian fluid and its viscoelastic behavior is quite a complex issue to investigate and used to be negected and modelled with Newtonina fluids.

Blood viscosity changes with the speed at which it flows. At high speed, blood is almost as fluid as water, whereas at low speed (as when blood flow in the major arteries almost comes to a halt at the end of diastole, the heart's relaxation phase), viscosity may increase three to five times. This dramatically increases the force required to pump the blood and changes the interaction between the blood and the arterial wall. Therefore, higher blood viscosity increases the 'drag' of the blood, and amplifies the tendency for eddies and therefore lower shear stress in the areas known to be prone to early atherosclerosis. Further, the resistance to blood flow and therefore the required pumping pressure (blood pressure) is directly dependant on the blood viscosity. Higher blood viscosity requires higher blood pressure to ensure the same circulating blood volume. Therefore, both the burden on the heart and the forces acting upon the vessel wall are directly influenced by changes in blood viscosity [**91**].

Several works focused on experiments and numerical simulations [**86, 87, 88, 89, 90**] of hemodynamics. Among others, Gijesen et al. [**89**] studied the influence of the non-Newtonian behavior compared to a Newtonian fluid that mimics blood properties. In order to achieve such

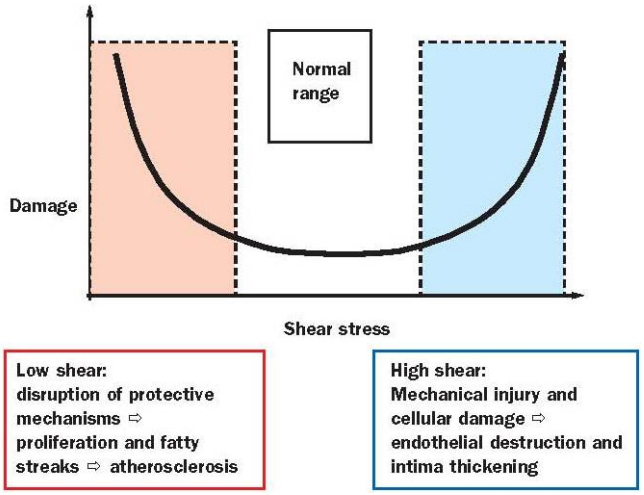

(a) Artery damages vs Blood Shear Stress

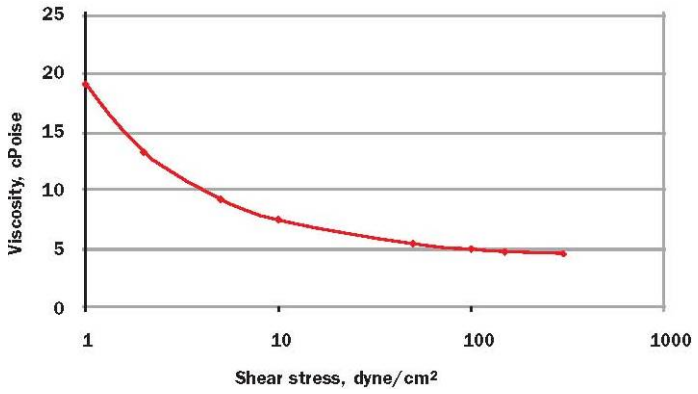

(b) Typica

FIGURE 12.1.2. Blood shear stress and viscosity. Source [**91**]

goal, the blood viscosity was assumed to be equal to the blood shear rate limit ($\mu = 3.5{\times}10^{-3}\ Pa{\cdot}s$). The shear thinning in the blood stream seemed to play an important role in the blood fluid dynamics. As a general result, the velocity profile along the artery of a non-Newtonian flow was flatter compared to a simil-Newtonian blood stream. It is not clear whether this fact may consistently affect numerical results on artery lesions predictions. However, it seems possible to mimic a non-Newtonian flow with a Newtonian one, although the viscoelastic modelling of blood is not completely solved.

The work presented in this chapeter attempted to mimic blood viscoelastic behavior (fluid rheology) with particles injected in a Newtonian flow: the rheology, or history, is recorded and advected in the blood stream by particles. Since the flow stream is Newtonian with a modified viscosity and density (no memory) it suits the requirements of the particle tracking in post-processing.

To test such a memory decoupling model, a simple RANS simulation was performed on a ideal carotid artery bifurcation. The attempt was to simulate fat particles motion and deposition. The main aim was to simulate the fatty deposit thickening process on arterial tissues. The fact that what is transported in the blood stream is absorbed due to non mechanical processes requires further and strong assumptions to be made.

(1) mechanical deposition/impact mimics the long process of absorption due to concentration osmosis and other related phenomena
(2) parcels of fat, as solid body released by the liver[1]
(3) fat may adhere to tissues
(4) Young moduli were assumed as the ones for steel (arteria tissue), soft light rubber (high viscosity blood particles) and glass (fat, released post-traumas)
(5) constant pressure condition mimics an average pressure difference in a long life time period
(6) flow viscosity $\mu = 1.5 \times 10^{-3}\ Pa \cdot s$ and density $\rho = 1100\ kg/m^3$ **[91]**
(7) the rigid model of the artery is a rather simplified geometry which lacks of local widening and narrowing patterns typical of a real human artery

The geometrical assumptions did affect the fluid dynamics and velocity profiles along the carotid did not show any turbulent or swirl "C" shape typical behavior **[87, 89, 90]**. As mentioned above, the final goal was

[1]Human liver may release fat that agglomerates in particles as consequence of an accident (physical trauma)

not to reproduce a correct fluid dynamic case but to numerically test the possibility to "address" the fluid memory to particles and to model the non-mechanical tissue thickening with a viscoelastic mechanical model for particles.

12.2. Numerical Results

Since the geometry reproduced was not suitable to represent a typical blood fluid dynamics, the shear stress along the geometry was incorrect. Therefore, the viscosity dependency on the local shear stress, see Fig. 12.1.2b, of the simil-blood particle was not implemented and the particle viscosities were assumed constant.

The computational strategy to simulate arteria thickening is to apply the Step-RANS approach, see Section 9.2, combined with the deposit growth (arteria tissues tickening). Unfortunately, the thickness of the deposit (arteria obstruction) can only increase in human people...

Fig.12.2.1 presents the geometry used in this work. The Step-RANS approach is necessary to recalculate the shear stress along the geometry and to track particles with updated properties. The deposit growth algoritm, see Section 2.2, was applied only once. Results of the tissue thickening are shown in Fig. 12.2.2a-b. To see particle distribution at the bifurcation, it seemed necessary to apply the unsteady particle tracking. Fig. 12.2.1 shows two snapshots of the animation, [Weblink Arteria Carotis Communis]

12.3. Conclusion & Remarks

The simplified geometry used in the simulations was not accurate enough to correctly describe a the fluid dynamics at the carotid bifurcation. Therefore the shear stress values along the carotid could have led to unrealistic particle behavior. The work presented here attempted to demonstrate the modeling of blood (rheological) viscoelastic behavior with particles advected in a Newtonian fluid (non-rheological). Arteria tissue thickneing was modelled applying the deposit growth algorithm presented in Section 2.2. However, results show that it is possible to study arteria thickening with simil-blood particles. Indeed the shear

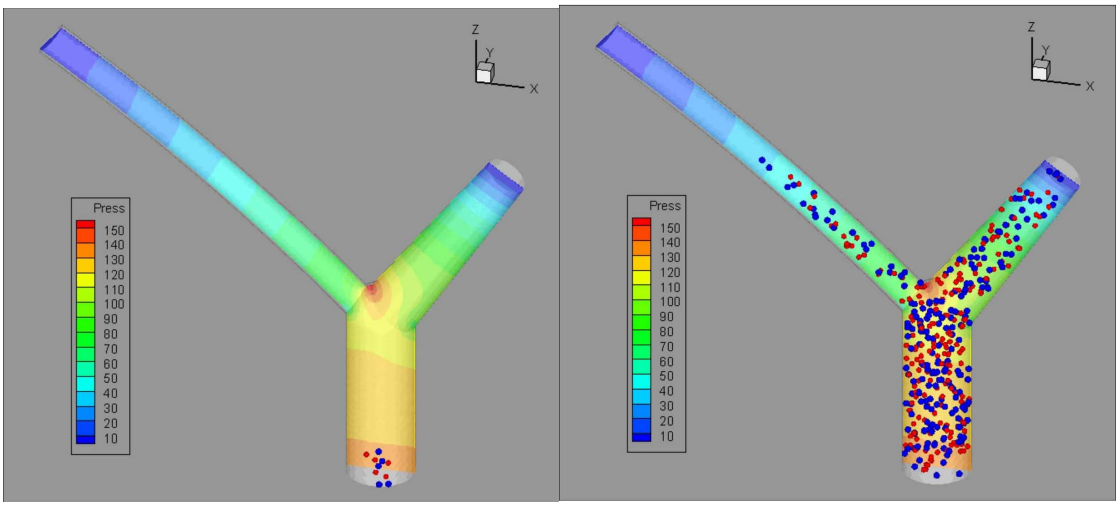

(a) (b)

FIGURE 12.2.1. Arteria Carotis Communis snapshots. Animation available at [Weblink Arteria Carotis Communis]

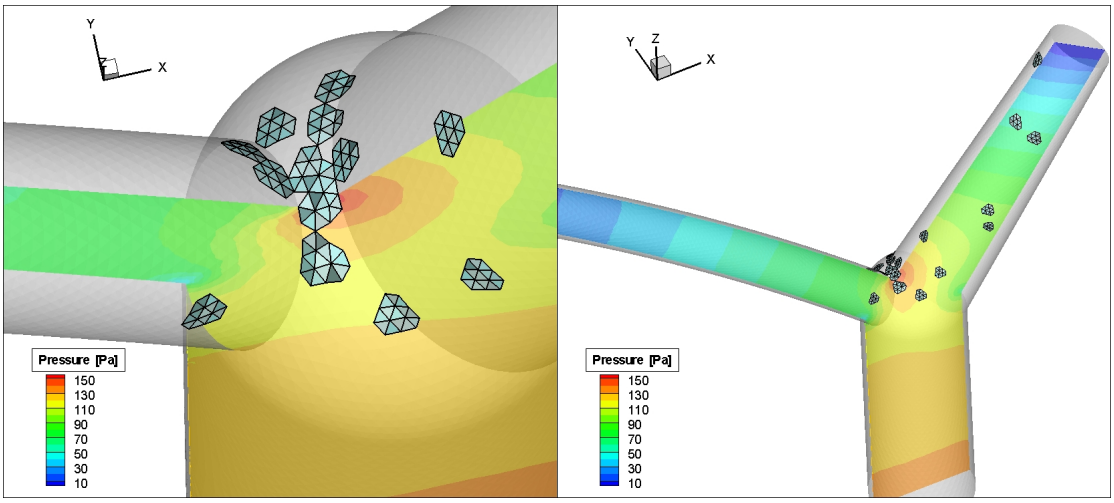

(a) (b)

FIGURE 12.2.2. Arteria Carotis Communis Deposit

stress field should be sufficiently accurate and the dependency of the viscosity of the simil-blood particles explicited as function of the fluid

shear stress. The shear stress field can be recalculated importing the deposited geometry into the CFD code again (see Step-RANS approach, Section 9.2). The Step RANS approach seems suitable to represent changes in a long term period (month or years) which cannot be simulated performing a CFD time dependent simulation.

Part 5

Conclusions, Bibliography & Appendices

Conclusions

"...If I asked you 'What is life?', you would probably reply, in so many words, that it is all just a coincidence. So, the question remains. What sort of coincidence?"

- 'The Lemon Table', Julian Barnes.

The final goal of the present thesis was to provide a numerical estimate of particle deposition, deposit composition, deposit thermal resistance and temperature behavior in burners of coal and biomass with high silicate content burners, applying mechanical and rheological models for visco-elastic solids. Typically, in pulverized coal and biomass burners the deposit prediction plays a key role in estimating performance loss in heat exchanging process. These losses result in decreasing production and raising operational costs. A novel computational strategy to predict particle trajectories, and a visco-elastic approach to eventually evaluate their deposition by post-processing CFD data has been presented. This strategy is based on two particle tracking techniques which can be combined with steady and unsteady CFD data, either in the complete or reduced computational domain. A visco-elastic approach models particle deposition by calculating the tangential and normal to boundary energy restitution coefficients. Experimental results using glass particles obtained at the ECN LCS facility have been used to validate the visco-elastic deposition model. The code developed uses polyhedral (hybrid) unstructured meshes (P1 elements only). The novel two-step cell detection algorithm, coupled with the trilinear-isoparametrical interpolation, provides acceptable CPU time as well as

computational accuracy even in the case of cell distortion due to deposition. Particles are assumed as visco-elastic solids, and their time and temperature compliance are modeled using a Standard Linear Solid spring dash-pot model (SLS). The particle stickiness behavior model follows the mathematical energy restitution coefficient approach proposed by Stronge and Thornton and based on the JKR theory. Restitution and friction coefficients have been modeled as functions of the particle composition and temperature by calculating of the equivalent Young modulus and the surface energy. Viscosity, creep compliance and the work of adhesion are the key parameters to model the stickiness behavior of the colliding bodies. The visco-elastic approach has proved to be adequate to properly describe elasto-plastic particle impact. The Maxwell and Standard Linear Solid model (SLS), used in this work to mimic soft particle (JKR theory) impact, numerically predict the Young modulus of the particle and the wall (either clean or dirty) according to the viscosity and particle dwelling time. This modelling can be applied both when temperature may soften the particle, and in those cases where temperature is substantially so low as to not consistently influence (either harden or soften) particle elastic properties. In the latter cases, the model simply describes particle impact from a mechanical point of view, also investigated by Hertz and Davies primarily, and by Johnson, Derjaguin, Maugis and Stronge lately. The joint use of all the above computational strategies, allows to extend to a broader range of opportunities the intrinsic computational limits of the decoupled flow-particle interaction. Some other applications were investigated by combining computational strategies. Particle motion in industrial ice scrapers and particle separators, sand deposition in water pipelines, aerosol deposition and fat deposition on tissues in hemodynamics were investigated. Although several limitations were found and pointed out in this dissertation, in general the presented results showed good agreement with both experiments (when available) and expectations, when no experimental data were available.

Curriculum Vitae

The author Marco Losurdo was born on January 11, 1976 in Rome, Italy. He defended his M.Sc. diploma thesis "Numerical CFD Simulations of a Trapped Vortex Combustor" in Aerospace Engineering at the University of Rome "La Sapienza" in 2002. He perfomed further work on numerical CFD combustion simularions at The Cardiff University of Wales (UK) from 2002 to 2003, financed by the European Program Euroflame. The PhD work reported in this dissertation was accomplished between 2004-2008 as PhD student at Delft University of Technology. From 2008, he is employed at the Technical University of Munich (Germany) in the field of numerical simulations of slagging and fouling occurring in industrial burners and gasifiers.

Selected Publications

2008-2009

- Losurdo M., Spliethoff H., Kiel J., A novel computational strategy for Lagrangian particle tracking and particle deposition, submitted to Computers & Fluids, accepted with revisions.

2007

- Losurdo M., Roekaerts D., Bertrand C. (2007). A novel CFD strategy for numerical investigation of particle deposition in industrial applications. NPS7 conference proceedings.
- LosurdoM., Kiel J., Spliethoff H. (2007). Particle deposition numerical studies in co-firing biomass burners. A novel Lagrangian particle tracking code dedicated to CFD data post processing. IFRF conference proceedings, Pisa, Italy.
- Bruno, C., & Losurdo, M. (2007). The Trapped Vortex Combustor: An Advanced Combustion Technology for Aerospace and Gas Turbine Applications. In Advanced Combustion and Aerothermal Technologies (pp. 365–384).
- Losurdo, M., Bertrand, C., & Spliethoff, H. (2007). A Lagrangian Particle Cfd Post-Processor Dedicated To Particle Adhesion/Deposition. In ECI Symposium Series – Heat Exchanger Fouling and Cleaning – Challenges and Opportunities. Tomar, Portugal: ECI Symposium Series.

2006

- Losurdo, M., Bruno, C., & Patrignani, L. (2006). Numerical Simulations of Trapped Vortex Combustors. Feasibility Study of TVC integration in traditional GT combustion chambers. In 42nd AIAA/ASME/SAE/ASEE Joint Propulsion Conference and Exhibit. Sacramento, California.

2005

- Losurdo, M., Korbee, R., Venneker, B., Kiel, J., & Spliethoff, H. (2005). Ash and Fouling Deposition in Pulverized Co-Firing BiomassBurners: CFD Ash Deposition Modelling. In ECCO-MAS Thematic Conference on Computational Combustion.
- Korbee, R., Losurdo, M., Lensselink, J., Cieplik, M. K., & Verhoeff, F. (2005). Monitoring And Modelling Of Gas-Side Boiler Fouling. In ECI – Heat Exchanger Fouling and Cleaning – Challenges and Opportunities. Kloster Irsee, Germany.

Bibliography

[1] Sippola M-R., Nazaroff W.W., Particle Deposition from Turbulent Flow: Review of Published Research and Its Applicability to Ventilation Ducts in Commercial Buildings, Lawrence Berkeley National Report, LBNL - 51432, June 2002.

[2] Baxter L.L., De Sollar R.W., A mechanistic description of ash deposition during pulverized coal combustion: predictions compared with observations, 1993, Fuel Vol 72, Issue 10, pp. 1411-1418.

[3] Stronge W.J., Impact Mechanics, 2000, Cambridge University Press.

[4] Quesnel D.J., Rimai D.S., Sharpe L.H., Particle adhesion: application and advances, 2001, New York Taylor and Francis.

[5] Baxter L.L., Mitchell R.E., Release of Iron During the Combustion of Illinois No. 6 Coal, 1992, Combust. Flame, Vol. 88, pp. 1-14.

[6] Srinivasachar S., Helble J.J., Boni A.A., Mineral behavior during coal combustion 1. Pyrite transformations, 1990, Progr. Energy Combust. Sci., 16, pp. 281-292.

[7] Srinivasachar S., Helble J.J., Boni A.A., Shah N., Huffman G.P. and Huggins F.E., Mineral behavior during coal combustion 2. Illite transformations, Progr. Energy Combust. Sci. Vol. 16, 1990, pp. 293-302.

[8] Kaer S. K., Numerical investigation of ash deposition in straw-fired boilers, Ph.D. Thesis, Aalborg University, Denmark, 2001.

[9] Lee F. and Lockwood F., Modelling ash deposition in pulverized coal-fired applications, Progr. Energy & Comb. Sci., 25, 1999, pp. 117-132.

[10] Bocksell T.L., Loth E., Stochastic modeling of particle diffusion in a turbulent boundary layer, International Journal of Multiphase Flow, Vol. 32, pp. 1234–1253, 2006.

[11] Senior, C. and Srinivasachar S., Viscosity of ash particles in combustion systems for prediction of particle sticking., Energy and Fuels, 9, 1995, pp. 277–283.

[12] Costen P.G., Lockwood F.C. and Siddique M.M., Mathematical Modelling of Ash Deposition in Pulverized Fuel-Fired Combustor, Proc. Comb. Inst., Vol 28, 2000, pp. 2243-2250.

[13] Lakes R.S., Viscoelastic Solids, 1999, CRC Press.

[14] Greenwood J.A. and Williamson J.B., 1966, Proc. R. Soc. Lond. A 295 300.

[15] Johnson K.L., Kendall K. and Roberts A.D., 1971, Proc. R. Soc. Lond. A 324 301.

[16] Derjaguin B.V., Muller V.M., Toporov Y.P., 1975, Proc. R. Soc. Lond. A 324 301.

[17] Tabor D.,Surface Forces and Surface Interactions, J. Colloid Interface Sci., Vol.58 pp2-13, 1977.

[18] Johnson, K. L. and Greenwood, J. A., An adhesion map for the contact of elastic spheres. J. Coll. Interface Sci., 1997, 192, 326–333.

[19] Maugis D., Adhesion of spheres: The JKR-DMT transition using a dugdale model, J. Colloid and Interface Sc. Tech., Vol. 150, Issue 1, pp 243-269 , 1992.

[20] Maugis D., On the Contact and Adhesion of Rough Surfaces, J. Adhesion Sci. Technol., Vol. 10, No. 2, pp. 161-175, 1996.

[21] Morrow C.A., Adhesive Rough Surface Contact, Ph.D. Thesis, Pittsburgh University, 2003.

[22] Strandström K., Muller C., Hupa M., Development of an ash particle deposition model considering build-up and removal mechanisms, Fuel Processing Technology Vol. 88, pp. 1053-1060, 2007.

[23] Malkin A.Y., Rheology Fundamentals, 1994, Canada ChemTec Publishing.

[24] Vargas S., Frandsen F.J., Dam-Johansen K., Rheological properties of high-temperature melts of coal ashes and other silicates. Progress in Energy and Combustion Science, Vol. 27, pp. 237-429, 2001.

[25] Walsh P.M., Sayre A.N., Loehden D.O., Monroe L.S., Beer J.M., Sarofim A.F., Deposition of bituminous coal ash on an isolated heat exchanger tube: Effects of coal properties on deposit growth, Progr. Energy Combust. Sci., 16 (4), 1990, pp. 327-345.

[26] Snyder W.H. and Lumley L., Some measurements of particle velocity autocorrelation functions in turbulent flow, J.Fluid Mech., Vol. 48, part 1, pp. 41-71, 1971.

[27] Matida E.A., Finlay W.H., Lange C.F. and Grgic B., Improved numerical simulation of aerosol deposition in an idealized mouth-throat, Journal of Aerosol ScienceVolume 35, Issue 1, January 2004, pp 1-19.

[28] Lohner R., Ambrosiano J. A vectorized particle tracer for unstructured grids, Journal of Computational Physics, Vol. 91, pp. 22-31, 1990.

[29] Lohner R., Robust, Vectorized Search Algorithm for Interpolation on Unstructured Grids, Journal of Computational Physics, Vol. 118, pp. 380-387, 1995.

[30] Haselbacher A., Najjar F.M., Ferry J.P., An Efficient and Robust Particle-Localization Algorithm for Unstructured Grids, Journal of Computational Physics, Vol. 225, pp. 2198-2213, 2007.

[31] Chen X.-Q. Pereira J.C.F., A new Particle-Locating Method accounting for Source Distribution and Particle-Field Interpolation for Hybrid Modelling of Strongly Coupled Two-Phase Flows in Arbitrary Coordinates, Numerical Heat Transfer, Part B: Fundamentals, Vol. 35, No. 1, pp. 41-63, 1999.

[32] Zhou Q. Leschziner M.A., An Improved Particle-Locating Algorithm for Eulerian-Lagrangian Computations of Two-Phase Flows in General Coordinates, International Journal of Multiphase Flow, Vol. 25, pp. 813-825, 1999.

[33] Oliveira P.J., Gosman A.D and Issa R.I., A Method for Particle-Location and Fiel Interpolation on Complex Three-Dimensional Computational Meshes, Adv. Eng. Software, Vol. 28, pp. 607-614, 1997.

[34] Martin G.D., Loth E., Lankford D., Particle host cell determination in unstructured grids, Comput Fluids (2008) doi:10.1016/j.compfluid.2008.01.005

[35] Quarteroni, A. and Valli, A., 1999. Domain decomposition methods for partial differential equations, Oxford Science Publications, Oxford.

[36] Dreeben, T.D., Pope, S.B., Probability density function and Reynoldsstress modeling of near-wall turbulent flows. Phys. Fluids 9 (1), 154–163, 1997.

[37] Dehbi A., A CFD model for particle dispersion in turbulent boundary layer flows, Article in Press Nuclear Eng. Design, 2007.

[38] Greenfield C., Quarini G., A Lagrangian simulation of particle deposition in a turbulent boundary layer in the presence of thermophoresis. Applied Mathematical Modelling, Vol. 22, pp. 759-771, 1998.

[39] Kallio G.A., Reeks M.W., A numerical simulation of particle deposition in turbulent boundary layers, Int. J.Multiphase Flow, Vol. 15, No. 3, 433-446, 1989.

[40] Wang Y. and James P.W., On the effect of anysotropy on the turbulent dispersion and deposition of small particles. International Journal of Multiphase Flow, Vol. 25, pp 551-558, 1999.

[41] Loth E., Numerical approaches for motion of dispersed particles, droplets and bubbles, Progress in Energy and Combustion Science, 2000, Vol. 26, pp. 161–223.

[42] Abd-Elhady M.S., Rindt C.C.M., Van Steenhoven A.A., Optimization of Flow Direction to Minimize Particulate Fouling of Heat Exchangers, 2007, Heat Exchanger Fouling and Cleaning - Challenges and Opportunities, H. Müller-Steinhagen, M.R. Malayeri and A.P. Watkinson, Canada Eds, ECI Symposium Series, Volume RP5.

[43] Talbot L., Thermophoresis of particles in a heated boundary layer, Journal of Fluid Mech., Vol. 101, part 4, pp. 737-758, 1980.

[44] Morsi S.A. and Alexander A.J., An investigation of particle trajectories in two-phase flow systems, J. Fluid Mech. 55 (1972), p. 193

[45] Gosman, A. D. and Ioannides, S. I., 1983, Aspects of computer simulation of liquid-fuelled combustors, AIAA J of Energy, Vol. 7, No. 6, pp 482-490.

[46] Schuen, J. S., Chen, L. D., & Faeth, G. M. (1983). Evaluation of a stochastic model of particle dispersion in a turbulent round jet. American Institute of Chemical Engineers (AIChE) Journal, 29(1), 167–170.

[47] FLUENT, FLUENT 6.2 Users Guide (2005) Lebanon, USA.

[48] Berrouk A.S., Laurence D., Stochastic modelling of aerosol deposition for LES of 90^o bend turbulent flow, Int. J. Heat and Fluid Flow (2008), doi:10.1016/j.ijheatfluidflow.2008.02.010

[49] Huang L.Y., Norman J. S., Pourkashanian M. and Williams A., Prediction of ash deposition on superheater tubes from pulverized coal combustion, 1996, Fuel, Vol. 75, Issue 3, pp. 271-279.

[50] Israel R. , Rosner D.E., Use of a generalized stokes number to determine the aerodynamic capture efficiency of non-stokesian particles for a compressible gas flow. 1983, Aerosol Sci. & Tech. 2, pp. 45–51.

[51] Mittal K.L., Contact angle, wettability and adhesion, 2002, Vol.2, Utrecht VSP.

[52] Gerberich W.W. and Cordill M.J., Physics of Adhesion, Reports on Progress in Physics, Vol. 69, pp 2157-2203, 2006.

[53] Takahashi H. and Hiki Y., Kobayashi H. Study on the Shear Viscosity of Several Inorganic Glasses, Journal of Applied Physics, Vol. 84, No. 1, pp. 213-218, 1998.

[54] Thornton C., Yin K.K., Impact of elastic spheres with and without adhesion, Powder Technology, 1991, Vol 65, pp. 153-166.

[55] Thornton C., Ning Z., A theoretical model for the stick/bounce behaviour of adhesive elastic-plastic spheres, Powder Technology, 1998, vol 99, pp. 154-162.

[56] Chau K.W., Contact Dynamics of a Step-loaded Viscoelastic Solid, 2006, J. Phys. D: Appl. Phys. 39, pp. 712-720.

[57] Lim C.T. and Stronge W.J., Normal Elastic-Plastic Impact in Plane Strain, Mathl. Comput. Modelling, Vol. 28, No. 4-8, pp. 323-340, 1998.

[58] Urbain G., Bottinga Y., Richet P., Viscosity of liquid silica, silicates and alumino-silicates, Geochimica et Cosmochimica Acta Vol. 46 pp. 1061-1072.

[59] Batyrev I., A. Alavi, and M. Finnis, Equilibrium and adhesion of Nb/sapphire: The effect of oxygen partial pressure, Phys. Rev. B 62, pp. 4698-4706, 2000.

[60] Hoomans B.P.B., Granular Dynamics of Gas-solid Two-Phase Flow, 2000, PhD Thesis, Twente University, Enschede, The Netherlands.

[61] Milojevic D., Lagrangian Stochastic-Deterministic (LSD) Prediction of Particle Dispersion in Turbulence, 1990, Particle & Particle Systems Characterization, Vol. 7, Issue 4, pp. 181-190.

[62] Tomeczek J., Palugniok H., Ochman J., Modelling of deposit formation on heating tubes in pulverized coal boilers, 2004, Fuel Vol 83, pp. 213-221.

[63] Korbee R., Boersma A.R., Cieplik M.K., Heere P.G.Th., Slort D.J., Kiel J.H.A., Fuel characterisation and test methods for biomass co-firing, 2003, Report ECN-C-03-057, p.41.

[64] Korbee R., Losurdo M., Lensselink J., Cieplik M.K. and Verhoeff F., Monitoring and modelling of gas-side boiler fouling, 6th Int. Conference on Heat Exchanger Fouling and Cleaning Challenges and Opportunities, Proceedings Vol. RP2, ECI Symposium Series, Kloster-Irsee, Germany June 5-10, 2005.

[65] Johnson K. L., Mechanics of Adhesion, Tribology International, Vol. 31, No. 8, pp. 413-418, 1998.

[66] Johnson, K. L., Contact Mechanics. C.U.P., 1985.

[67] Heenan, A.F., Finlay W.H., Matida E.A. & Pollard A., Eperimental measurements and computational modelling of the flow field in an idealized extrathoracic airway. Experiments in Fluids, 35, 70-85, 2003.

[68] De Haan, W. H. & Finlay, W. H., In vitro monodisperse aerosol deposition in a mouth and throat with six different inhalation devices, Journal of aerosol Medicine, 14(3), 361-367, 2001.

[69] Grgic B., Finlay, W. H., Heenan A.F., Regional aerosol deposition and flow measurements in an idealized mouth and throat., Aerosol Science, 35, 21-32, 2004.

[70] Grgic B., Finlay, W. H., Burnell P.K.P., Heenan A.F., In vitro intersubject and intrasubject deposition measurements in realistic mouth–throat geometries., Aerosol Science, 35, 1025-1040, 2004.

[71] Pyykönen J. and Jokiniemi J. Development of a prediction scheme for pulverized coal-fired boiler slagging. In The Engineering Foundation Conference on 'Impact of Mineral Impurities in Solid Fuel Combustion', November 2-7, Kona, Hawaii, 1997.

[72] Mueller C., Selenius M., Theis M., Skrifvars B., Backman R., Hupa M., Tran H., Deposition behavior of molten alkali-rich fly ashes-development of a submodel for CFD applications. Proceedings of the Combustion Institute, 30 (2005), 2991-2998.

[73] Genceli, F.E., Gaertner, R. and Witkamp, G.J.(2005) Eutectic freeze crystallization of a 2nd generation cooled disk column crystallizer for MgSO4-H2O system. Journal of Crystal Growth , 275(1-2), pp. 1369-72.

[74] Van der Ham, F., Seckler, M. M., Witkamp, G. J. Eutectic Freeze Crystallization in a New Apparatus: The Cooled Disk Column Crystallizer, Chem. Eng. Proc. 43 (2003), 161

[75] Himawan, C., Kramer H. J. M., Witkamp, G. J. Study on the recovery of purified MgSO4M7H2O crystals from industrial solution by eutectic freezing, Separation and Purification Technology 50 (2) (2006), 240–248

[76] Vaessen, R.J.C., Himawan, C. and Witkamp, G.J. (2002), Scale formation of ice from electrolyte solutions on a scraped surface heat exchanger plate. Journal of Crystal Growth, 237-239 (Pt.3), pp. 2172-77.

[77] M. Losurdo, C. Bertrand and H.Spliethoff, A Lagrangian Particle CFD Post-Processor dedicated to particle adhesion/deposition, Heat Exchanger Fouling and Cleaning - Challenges and Opportunities", H. Müller-Steinhagen, M. Reza Malayeri, A. Paul Watkinson, Canada Eds, ECI Symposium Series, Volume RP5 (2007).

[78] P.A. Cundall, O.D.L. Strack, A discrete numerical model for granular assemblies, Geotechnique 29 (1979) 47–65.

[79] Arlov D., Revstedt J., Fuchs L., Numerical simulation of a gas–liquid Rushton stirred reactor - LES and LPT, Comput. Fluids (2007), doi:10.1016/j.compfluid.2007.03.017

[80] Ranade V., Van den Akker H., A computational snapshot of gas-liquid flow in baffled stirred reactors. Chem Eng Sci 1994; 49 (24B): 5175-92

[81] Ranade V. and Deshpande V., Gas-liquid flow in stirred reactors: trailing vortices and gas accumulation behind impeller blades. Chem Eng Sci 1999; 54: 2305-15.

[82] Bakker R., Van den Akker H., A Lagrangian Description of Micromixing in a stirred tank reactor using 1D-micromixing models in a CFD flow field. Chem Eng Sci 1996; 51(11): 2643-8

[83] Jayarajua S.T., Brounsa M., Verbanckb S., Lacora C., Fluid flow and particle deposition analysis in a realistic extrathoracic airway model using unstructured grids. Aerosol Science 38 (2007) 494 – 508.

[84] Johnstone A., Uddin M., Pollard A., Heenan W., Finlay W. H., The flow inside an idealized form of the human extrathoracic airway. Experiments in Fluids 37 (2004) 673 – 689.

[85] De Haan W. H., & Finlay,W. H. (2004). Predicting extrathoracic deposition from dry powder inhalers. Journal of Aerosol Science, 35, 309–331.

[86] Rindt C.C.M., Van de Vosse F. N., Van Steenhoven A.A.,Janssen J.D., Reneman R.S., A numerical and experimental analysis of flow field in two-dimensional model of the human carotid artery bifurcation. Journal of Biomechanics (1987), 20(5), 499–509.

[87] Rindt C.C.M. & Van Steenhoven A.A., Reneman R.S., An experimental analysis of the flow field in a three-dimensional model of the human carotid artery bifurcation. Journal of Biomechanics (1988), 21(11), 985–991.

[88] Rindt C.C.M., Van Steenhoven A.A.,Janssen J.D., Reneman R.S., Segal A. A numerical analysis of steady flow in three-dimensional model of carotid artery bifurcation. Journal of Biomechanics (1990), 23(5), 461–473.

[89] Gijsen F.J.H., Van de Vosse F. N., Janssen J.D., The influence of the non-Newtonina properties of blood on the flow in large arteries: steady flow in a carotid bifurcation model. Journal of Biomechanics (1999), 32, 601–608.

[90] Botnar R., Rappitsch G., Scheidegger M., Liepsch D., Perktold K., Boesiger P., Hemodynamics in the carotid artery bifurcation: a comparison between numerical simulations and in vitro MRI measurements. Journal of Biomechanics (2000), 33, 137–144.

[91] Malek A.M., Alper S.L., Izumo S., Hemodynamic shear stress and its role in atherosclerosis, JAMA (1999), 282(21), 2035-2042.

APPENDIX A

The JKR and DMT Theory

In the JKR theory bases its assumptions on an energy balance between the energy dissipated by the mechanic energy U_M (impact or compression load), the elastic stored energy U_E and the energy (loss) due to the adhesion U_S.

$$U_T = U_E + U_M + U_S \tag{A.0.1}$$

$$U_M = -P\delta \tag{A.0.2}$$

$$\delta = a^2/R^* \tag{A.0.3}$$

$$a^3 = R^* P/E^* \tag{A.0.4}$$

$$U_S = -\pi a^2 \Gamma \tag{A.0.5}$$

where Γ is the surface energy of both surfaces[**15**], a is the radius of contact and δ the space displacement due to the applied load P.

$$U_E = U_1 - U_2 = \frac{1}{E^{*\frac{2}{3}} R^{*\frac{1}{3}}} \left[\frac{1}{15} P_1^{\frac{5}{3}} + \frac{1}{3} P^2 P^{-\frac{1}{3}} \right] \tag{A.0.6}$$

$$U_1 = \int_0^{P_1} \frac{2}{3} \frac{P^{\frac{2}{3}}}{E^{*\frac{2}{3}} R^{*\frac{1}{3}}} dP = \frac{2}{5} \frac{P_1^{\frac{5}{3}}}{E^{*\frac{2}{3}} R^{*\frac{1}{3}}} \tag{A.0.7}$$

$$U_2 = \int_P^{P_1} \frac{2}{3}\frac{P}{E^* a} dP = \frac{1}{3E^{*\frac{2}{3}} R^{*\frac{1}{3}}} \left[\frac{P_1^2 - P^2}{P_1^{\frac{1}{3}}} \right] \tag{A.0.8}$$

where P is the effective applied load whereas P_1 is the *"apparent"* Hertz load, which essentially is the force virtually required to acquire the same radius of contact a_1 in case of adhesion (see Fig.A.0.1a). The equilibrium condition may be expressed by

$$\frac{dU_T}{da} = 0 \Rightarrow \frac{dU_T}{dP_1} = 0 \tag{A.0.9}$$

Such a condition takes to the solution:

$$P_1 = P + 3\Gamma\pi R + \sqrt{\left\{6\Gamma\pi R^* P + (3\Gamma\pi R^*)^2\right\}} \tag{A.0.10}$$

It can be noticed that in case of adhesion $P_1 > P$ while if $\Gamma = 0$, the formula returns $P_1 = P$. Substituing eq.A.0.10 into eq.A.0.4:

$$a^3 = \frac{R^*}{E^*}\left(P + 3\Gamma\pi R + \sqrt{\left\{6\Gamma\pi R^* P + (3\Gamma\pi R^*)^2\right\}}\right) \tag{A.0.11}$$

At a zero and separation load P[1]:

$$P = 0 \quad \Rightarrow \quad a^3 = \frac{R^*\left(6\Gamma\pi R^*\right)}{E^*} \tag{A.0.12}$$

$$\textit{separation} \quad \textit{condition} \quad \Rightarrow \quad P = -\frac{3}{2}\Gamma\pi R^* \tag{A.0.13}$$

However, in 1974 Derjaguin proposed the DMT theory based on molecular forces acting within a ring-shape area of noncontact adhesion which do not alter the Hertz load profile in the contact area. Using a "thermodynamic approach", the DMT theory stated that the attractive force is $2\pi w R^*$at the contact point. Tabor in 1977 pointed out that the main difference between the two theories was the fact that

[1]in eq.A.0.11 to have real and positive solutions, $6\Gamma\pi R^* P + (3\Gamma\pi R^*)^2 \geq 0$

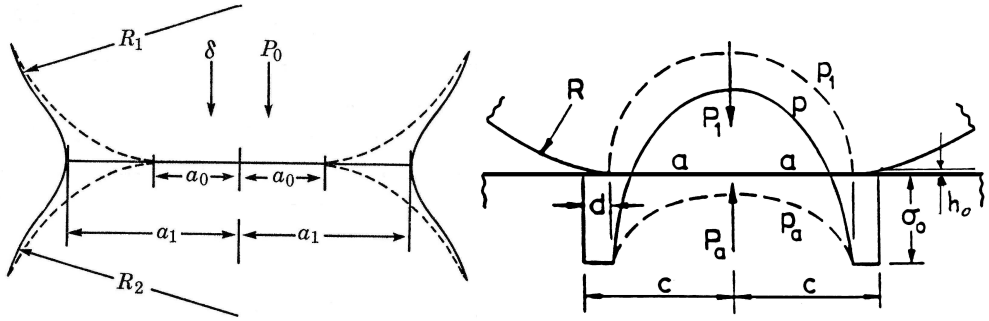

(a) (b)

FIGURE A.0.1. Load and displacement distribution in the JKR theory (a) and in the Maugis-Dugdale model (b). Pictures taken from Johnson[**15, 65**].

DMT neglects the deformation due to attractive forces close to the edge of the contact, while JKR at zero load the neck height h_0 (see Fig.A.0.1b) between the two bodies is of the same order of magnitude of the separation distance z_0.

APPENDIX B

Closure Algorithm for the Visco-Elastic Restitution Coefficients Modelling

The algorithm of the model is based on following steps.
Particle Visco-elastic Restitution coefficient modelling.

(1) temperature
(2) viscosity
(3) Young Modulus
(4) Restitution coefficients
(5) elastic, elastic-plastic, fully plastic collision (either particle-particle or particle-surface)

B.1. Temperature

The particle temperature is calculated at the center of the particle and assumed to be homogeneous within the particle (point mass assumption according to the Fourier conduction law: $\overrightarrow{\phi} = -k\overrightarrow{\nabla}T$, where $\overrightarrow{\phi}$ is the heat flux, k the thermoconductivity and $\overrightarrow{\nabla}T$ is the temperature gradient. The particle thermoconductivity is an inlet parameter and it is kept constant during the calculation.

B.2. Viscosity

Particle Viscosity has to be calculated by means of an interpolation function. The author of this dissertation chose the Urbain interpolation type proposed by Senior and Srinivasachar[**11**], which is following reported.

B.2.1. Temperature Dependence of Viscosity. Urbain showed and hence proposed to explicit the viscosity of a ash particle in pulverized coal combustion cases as reported in eq.B.2.1.

$$\ln \frac{\eta}{T} = A + \frac{10^3 B}{T} \tag{B.2.1}$$

where the viscosity is in poise and the temperature in Kelvin.

Senior and Srinivasachar extended the range of validity of this formulation proposing a new set of coefficients A and B to fit viscosity experimental results from high to very low silicate and alumina components solids. The main ash components which significantly may alter the properties of the ash and certainly ash deposit behavior, may simply fall in three groups:

(1) glass formers which form the basic anionic polymer unit: Si^{4+}, Ti^{4+}, P^{5+}

(2) modifiers which disrupt the polymer chains by bonding with oxygen and terminate the chains: Ca^{2+}, Mg^{2+}, Fe^{2+}, K^{+}, Na^{+}.

(3) amophoretics which may act either as formers or as modifiers: Al^{3+}, Fe^{3+}, B^{3+}.

To describe the behavior of glassy networks, the parameter $\frac{NBO}{T}$ was used. It represents the ration between nonbridging oxygens to the tetrahedral oxygens, as described in eq.B.2.2.

$$\frac{NBO}{T} = \frac{CaO + MgO + FeO + Na_2O + K_2O - Al_2O_3 - FeO_3}{\frac{(SiO_2 + TiO_2)}{2} + Al_2O_3 + Fe_2O_3} \tag{B.2.2}$$

Experimentally it was shown that increasing the amount of alumina for negative $\frac{NBO}{T}$ ratios, reduces the viscosity of the solid particle.

To both the coefficients A and B a polynomial formulation is given.

$$\begin{cases} A = \alpha_0 + \alpha_1 B + \alpha_2 \frac{NBO}{T} \\ B = B_0 + B_1 N + B_2 N^2 + B_3 N^3 \end{cases} \tag{B.2.3}$$

where N is the mole fraction of SiO_2 and coefficients α_i and B_i are given.